STATE AND PARAMETER ESTIMATION FOR VEHICLE DYNAMICS CONTROL USING GPS

A DISSERTATION
SUBMITTED TO THE DEPARTMENT OF MECHANICAL ENGINEERING
AND THE COMMITTEE ON GRADUATE STUDIES
OF STANFORD UNIVERSITY
IN PARTIAL FULFILLMENT OF THE REQUIREMENTS
FOR THE DEGREE OF
DOCTOR OF PHILOSOPHY

Jihan Ryu
December 2004

I certify that I have read this dissertation and that, in my opinion, it is fully adequate in scope and quality as a dissertation for the degree of Doctor of Philosophy.

J. Christian Gerdes
(Principal Adviser)

I certify that I have read this dissertation and that, in my opinion, it is fully adequate in scope and quality as a dissertation for the degree of Doctor of Philosophy.

Stephen M. Rock

I certify that I have read this dissertation and that, in my opinion, it is fully adequate in scope and quality as a dissertation for the degree of Doctor of Philosophy.

Günter Niemeyer

Approved for the University Committee on Graduate Studies.

This thesis is dedicated to my family.

Abstract

Many types of vehicle control systems can conceivably be developed to help drivers maintain stability, avoid roll-over, and customize handling characteristics. A lack of state and parameter information, however, presents a major obstacle. This dissertation presents state and parameter estimation methods using the Global Positioning System (GPS) for vehicle dynamics control. It begins by explaining basic vehicle dynamic models which are commonly used for vehicle dynamics control. The dissertation then demonstrates a method of estimating several key vehicle states – sideslip angle, longitudinal velocity, roll and grade – by combining automotive grade inertial sensors with a GPS receiver. Kinematic estimators that are independent of uncertain vehicle parameters integrate the inertial sensors with GPS to provide high update estimates of the vehicle states and the sensor biases. With a two-antenna GPS system, the effects of pitch and roll on the measurements can be quantified and are demonstrated to be quite significant in sideslip angle estimation. Using the same GPS system, a new method that compensates for roll and pitch effects is developed to improve the accuracy of the vehicle state and sensor bias estimates. In addition, calibration procedures for the sensitivity and cross-coupling of inertial sensors are provided to reduce measurement error further.

To verify that the estimation scheme provides appropriate estimates of the vehicle states, this dissertation shows that the state estimates from real experiments compare well with the results from calibrated models. The performance of the estimation scheme is also verified by statistical analysis. Results from the statistical analysis match predictions from the kinematic estimators. Since the proposed estimation scheme is based on a cascade estimator structure, the convergence of the cascade

estimator structure is also proven. As an application, the estimated vehicle states are used to virtually modify a vehicle's handling characteristics through a full state feedback controller. Results from this application show that the estimated states are accurate and clean enough to be used in vehicle dynamics control systems without additional filtering.

The dissertation then examines parameter estimation for vehicle dynamic models. Several important vehicle parameters such as tire cornering stiffness, understeer gradient, and roll stiffness, can be estimated using the estimated vehicle states. Experimental results show that the parameter estimates from proposed methods converge to the known values. Finally, the dissertation presents a new method for identifying road bank and suspension roll separately using a disturbance observer and a vehicle dynamic model. Based on the estimated vehicle parameters, a dynamic model, which includes suspension roll as a state and road bank as a disturbance, is first introduced. A disturbance observer is then implemented from the vehicle model using estimated vehicle states. Experimental results verify that the estimation scheme gives separate estimates of the suspension roll and road bank angles. The results of this work can improve the performance of stability control systems and enable a number of future systems.

Acknowledgements

First, I would like to thank my advisor, Chris Gerdes, for providing an excellent environment for research and study. I appreciate his guidance, technical insight, and dedication. I learned many things from him. I would also like to thank Chris for providing such cool test vehicles. I don't think many graduate students drive a BMW, Corvette, and Mercedes for their work.

I would like to thank my reading committee, Steve Rock and Günter Niemeyer, for taking their time to read my thesis. I really appreciate their helpful comments. I would also like to thank Per Enge and Tom Kenny for being on my oral examination committee.

I want to thank all of my colleagues in the Dynamic Design Lab for the support, advice, and friendship. Chris, Eric, Greg, Hong, Josh, Judy, Matt, Paul, Sam, Shad made the lab a wonderful place. My life and research at Stanford would have never been the same without them. I also want to thank my KSAS and KME friends, who made my life at Stanford not only less boring but also exciting and meaningful. They are great friends.

I want to especially thank my family for their continuous support and encouragement. Special thanks to my mom. I could not have been here without her. I also want to thank my little daughter, Erin, for being in my life. Finally, I want to thank my wife, Myoung Jee, for believing in me.

Contents

List of Tables

List of Figures

Chapter 1

Introduction

Automobiles are indispensable in our modern society, and vehicle safety is consequently very important in our everyday life. In the past few decades, vehicle dynamics control systems have been developed to improve control and safety of vehicles. Vehicle dynamics control systems seek to prevent unintended vehicle behavior through active control and help drivers maintain control of their vehicles. Among them, Anti-lock Brake Systems (ABS) to prevent wheel lock-up have become common equipment in production passenger vehicles, and traction control systems are also becoming popular to prevent the drive wheels from losing grip when accelerating [50]. In addition to ABS and traction control, many automotive companies have been developing Electronic Stability Control (ESC) systems to prevent the vehicle from spins, skids, and rollovers [47, 50]. The main function of electronic stability control is to provide enhanced stability and control not only when accelerating and braking but also when cornering and avoiding obstacles.

During cornering, a stability control system compares a driver's intended vehicle motion with the vehicle's actual behavior. When the stability control system detects a discrepancy between them, it automatically applies brakes to individual wheels to bring the movement of the vehicle back in line with the driver's intention. The driver's intention is calculated from the driver's commanded steering wheel angle and speed of the vehicle, which can easily be measured using the steering wheel angle sensor and wheel speed sensors. In order to determine the vehicle's actual behavior,

current stability control systems use measurements from a yaw rate gyro and lateral accelerometer. The yaw rate gyro gives the rotation rate of the vehicle, and the measured lateral acceleration with the yaw rate gives an indication of vehicle lateral motion. However, this is only a rough indication since a sliding or skidding vehicle may not be spinning and thus may have a normal yaw rate. In such cases, the sideslip angle of the vehicle must be known to determine the vehicle's lateral motion in addition to its rotational motion. The vehicle sideslip angle captures the lateral velocity because it is the angle between the longitudinal axis of the vehicle body and the direction of the vehicle velocity. Current vehicles, however, are not equipped with an ability to measure the sideslip angle directly, and this limits the algorithms that can be incorporated in production systems. The inability to sense vehicle sideslip angle is the primary challenge in the development of stability control systems [49].

Instead of measuring sideslip angle directly, stability control systems on current production vehicles estimate sideslip angle for their control purposes. One common method for estimating sideslip angle is to combine measurements from the yaw rate gyro and lateral accelerometer [17, 38]. Because the time derivative of sideslip angle can be expressed in terms of yaw rate and lateral acceleration, sideslip angle can be estimated by integration of these measurements [16, 47]. Unfortunately, measurements from these sensors contain bias as well as electrical noise, and can drift with temperature changes. In addition, the lateral accelerometer cannot distinguish between the acceleration from lateral motion of the vehicle and the acceleration due to gravity during vehicle roll motion. As a result, the integration can accumulate error from sensor noise and vehicle roll. These errors limit the effectiveness of current stability control systems, and improvements in estimating sideslip angle will enable the vehicle control systems of the future.

Since the vehicle sideslip angle is the difference between the vehicle yaw angle and the direction of the velocity, the sideslip angle can be calculated if both the attitude and velocity of the vehicle are known. Inertial Navigation System (INS) could provide these values by integrating gyro measurements to get the attitude and integrating accelerometer measurements with gravity compensation to get the velocity [5, 11, 13, 20]. Historically, INS has been commonly used in aircraft and

missile applications. Since the first INS system was used in the German V1 and V2 missiles in World War II, many aircraft and missile applications have used INS to keep track of position, velocity, and attitude for navigation purposes [32]. A typical inertial navigation system uses a combination of accelerometers and gyros, and solves a large set (usually 6 DOF) of differential equations to convert these measurements into estimates of position, velocity and attitude [11]. However, integration of inertial measurements is limited by the drift caused by sensor bias and sensitivity as small errors in measurement are integrated into progressively larger errors in attitude and velocity. In general, sensor quality (grade) is judged according to this drift rate. To estimate the vehicle yaw angle over long periods of time with enough accuracy for sideslip angle determination using INS alone would require a tactical or navigation grade system with a 1 deg/hr drift rate or better. Such accurate systems are usually implemented using a wheel (called the rotor) spinning at high speed on a multi-gimbal structure. The speed of the rotor is precisely controlled by an electric motor, and the mounting structure should be manufactured with extremely high precision. With a cost of $10,000 or more [11, 21], such an INS system is much too expensive for automotive applications.

Instead, lower-cost MEMS (Micro-Electro-Mechanical System) gyros can be used. A typical MEMS gyro uses an electrostatically driven, vibrating silicon mass. In response to an angular rate, the mass is deflected by the Coriolis force. This deflection is sensed capacitively, and the amplitude is proportional to the angular rate. Even though it has a cost advantage, this measurement method is sensitive to temperature changes and drifts with them [15]. As a result, using a MEMS sensor alone is not sufficient to estimate the vehicle yaw and sideslip angle over long periods of time. However, integration with attitude and velocity measurements from the Global Positioning System (GPS) can effectively negate these drift effects and enable the use of these sensors.

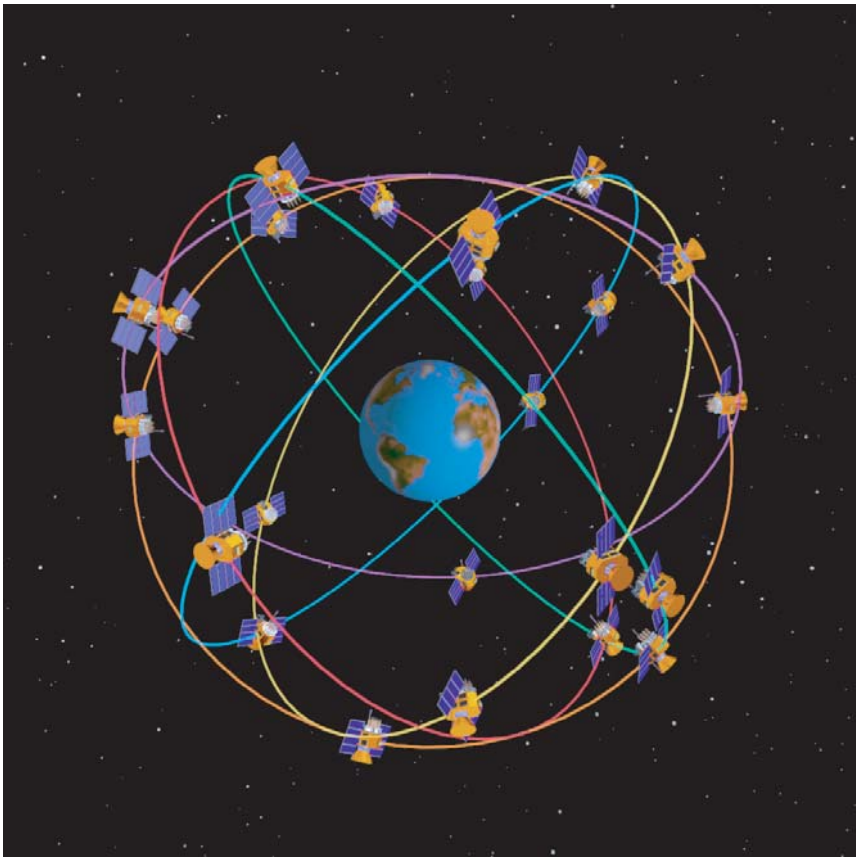

Figure 1.1: GPS Constellation (Illustration: The Aerospace Corporation)

1.1 Global Positioning System

The Global Positioning System (GPS) is a satellite-based navigation system consisting of a constellation of 24 satellites. The U.S. military developed and implemented this satellite network as a military navigation system, but in the 1980s, the government made the system available for civilian use. GPS satellites circle the earth twice a day at an altitude of about 20,000 km in a very precise orbit, continuously monitored by ground stations located worldwide. The satellites transmit information on radio signals to earth, and GPS receivers interpret this information. Then, the GPS receiver calculates the travel time of signals by comparing the time a signal was transmitted by a satellite with the time it was received. The receiver multiplies this time by the speed of radio waves to determine how far the signal traveled. With this distance of

travel, the receiver uses trilateration to calculate the receiver's exact position. As a result, a standard GPS receiver can provide position information with about 10 meter accuracy [25, 36].

Even though standard GPS position information has about 10 meter accuracy, GPS velocity information can be much more accurate by measuring the Doppler shifts of GPS carrier waves as shown in Fig. 1.2. The satellites transmit radio carrier

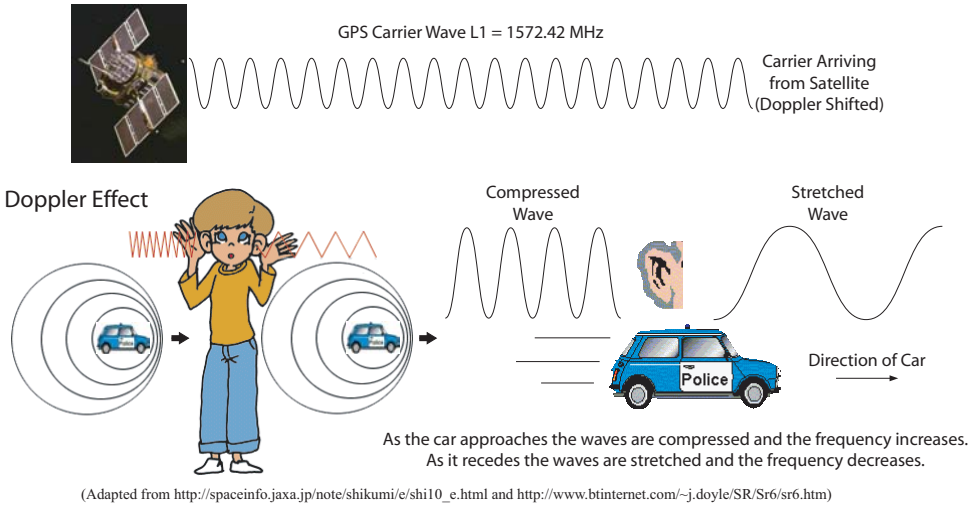

Figure 1.2: GPS Carrier Wave and Doppler Effect

waves at the L1 frequency (1575.42 MHz) for civil users. However, the frequency of the signal received by a GPS receiver is changed because of relative velocity between the satellites and receiver. This change is called the Doppler effect, and the difference between the frequency of the received signal and the original frequency at the source is called the Doppler shift. The accurate velocity of the receiver can be calculated by measuring the Doppler shifts in the incoming carrier waves. A GPS receiver can provide velocity information with accuracy of 3 cm/s (1σ, horizontal velocity) and 6 cm/s (vertical velocity) even without differential corrections [6].

In addition to velocity, attitude can be determined very accurately with multiple GPS antennas. Figure 1.3 shows the schematic of attitude determination. When the baseline length, b, is known, the attitude, θ, can be determined by measuring the range difference, Δr. The range difference, Δr, can be accurately measured by the

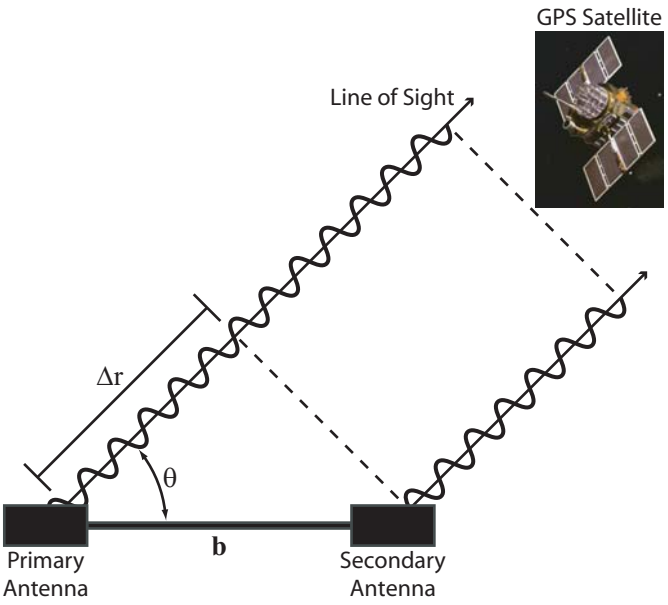

Figure 1.3: GPS Attitude Determination

phase difference of the carrier waves received at two antennas. Since a GPS receiver can measure L1 carrier phase with great precision (0.005 *cycle* or 1 *mm*) [36], GPS attitude is available with accuracy of 0.25 *deg* (1σ with 2 *m* baseline length) using the phase difference from carrier phase measurements [34]. One difficult problem involved in using the carrier phase measurements to determine attitude is the resolution of the integer ambiguity inherent in the carrier phase measurements. When the separation of two antennas exceeds $\lambda/2$ ($\lambda = 19$ *cm*, L1 carrier wavelength), relative phase is not sufficient to measure the range difference, Δr, and the integer number of cycles must also be determined. This integer ambiguity must be resolved before the measurements can be used for attitude determination. Multiple-antenna GPS systems have been deployed for automated farming and marine navigation [34, 39]

1.2 GPS/INS Integration for Vehicle Dynamics

The integration of INS sensors with GPS has been given much attention, especially in aircraft applications, due to the complementary nature of the individual systems.

GPS measurements are stable but subject to a fairly low update rate (1-10 Hz) and signal blockage while inertial sensor measurements are continuously available but suffer from long term drift.

GPS/INS integration is commonly implemented using Kalman filters. Schmidt discussed Kalman filters and computations for a gimballed INS and a strap-down INS [43]. Bar-Itzhack et al. presented a control theoretical approach to GPS/INS integration using Kalman filters for navigation [4]. Randle et al. used Kalman filters to integrate GPS with low cost INS sensors for both flight and land vehicle navigation [40]. Grewal et al. discussed the detailed working principles of the INS, GPS and Kalman filtering in their book [25]. Recently, Gautier designed the GPS/INS generalized evaluation tool (GIGET) using Kalman filters for navigation systems and tested it on an unmanned air vehicle [19].

Most of the previous GPS/INS integration work has focused on the navigation and dead reckoning of vehicles [51]. Da et al. and Gebre-Eaziabher et al. used INS sensor measurements to update position estimates between GPS measurement updates for aircraft navigation [13, 20]. Similarly, Berman et al. and Masson et al. utilized INS sensors to dead reckon during short GPS outages for aviation applications [5, 33]. Cannon et al. integrated low cost INS sensors with GPS to provide navigation capability to bridge GPS outages for tens of seconds, and the robustness of the system was studied for both airborne and ground tests [9]. Abbott et al. and Schonberg et al. investigated GPS/INS integration for land vehicle navigation and dead reckoning systems [1, 44].

Spurred by the increase in GPS systems in cars, Bevly et al. developed a method of estimating vehicle sideslip by integrating inertial sensors from a stability control system with velocity information from a single antenna GPS receiver using a planar vehicle model and Kalman filters [6, 7]. As discussed earlier, one advantage of using GPS velocity (or attitude) information for sideslip angle estimation is its accuracy. GPS attitude and velocity are considerably more accurate than position. While the standard GPS can provide absolute position within about a 10 meter radius, GPS attitude and velocity are available with errors on the order of 0.25 deg (1σ, attitude with 2 m baseline length), 3 cm/s (1σ, horizontal velocity), and 6 cm/s (vertical

velocity) even without differential corrections [6, 34].

However, out-of-plane vehicle motions due to roll and pitch could not be taken into account with the planar model, leaving open questions of system accuracy and the potential benefits of additional sensing and vehicle modeling. Even though additional sensing – such as a two-antenna GPS receiver – can help determine out-of-plane vehicle motions, more information is necessary to determine the interaction between the vehicle and ground. Sensors are usually installed on the vehicle body and therefore cannot fully explain the vehicle's motions without additional information from the sensors on the wheels or suspension of the vehicle. Especially in land vehicle applications, the interaction between a vehicle and the ground is very important to determine the vehicle's behavior. Figure 1.4 shows one example which illustrates that the sensors installed on the vehicle body are not enough to explain the interaction between the vehicle and ground. In Fig. 1.4, the two vehicles have the same vehicle roll with

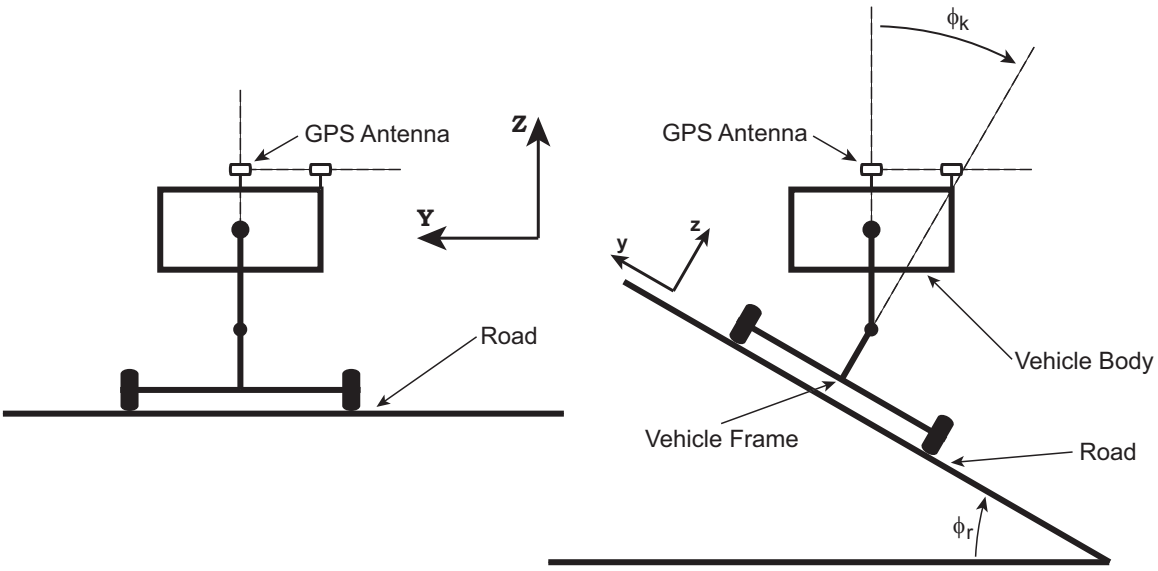

Figure 1.4: Vehicle with/without Roll and Road Bank

respect to the inertial frame, and the GPS thus gives the same roll measurements in both cases. However, the two vehicles are in very different dynamic situations. The vehicle on the flat surface will have similar responses to left and right steering, but the response of the vehicle on the banked surface will be highly dependent on the

steering direction. Additional vehicle models should be considered to separate these two cases.

1.3 Vehicle State and Parameter Estimation Using GPS

This thesis investigates the use of several GPS and inertial sensor configurations and levels of modeling fidelity in the estimation of vehicle states including sideslip angle. Unlike previous work, vehicle yaw information is obtained from a two-antenna GPS system that not only eliminates issues of drift in attitude estimation but also provides a measurement of the roll angle. Using a two-antenna GPS system, this thesis investigates the influence of road grade, bank angle, and suspension roll on GPS-based vehicle sideslip and longitudinal velocity estimates derived from a planar model. Since roll and grade have a pronounced effect [42, 46, 48], a new method of estimating several key vehicle states (sideslip angle, longitudinal velocity, yaw, and roll) and sensor biases is proposed using the two-antenna GPS system in combination with inertial sensors. The combined system fuses a road grade estimate derived from GPS velocity [3] and the roll information from the two-antenna system with an appropriate roll center model of the vehicle since the two antennas are placed laterally. Comparisons with a calibrated vehicle model show excellent correlation and the relative constancy of the sensor bias estimates demonstrates that no significant dynamics are ignored. From a practical standpoint, this thesis also describes a number of refinements to calibrate sensitivity variation and cross-coupling of inertial sensors. With multiple-antenna GPS systems currently deployed for automated farming [39] and under development at automotive price points, a sensing system such as this could be the key enabling technology for future vehicle dynamics control systems.

From a theoretical standpoint, the convergence of the proposed estimation method is proved in this thesis, and statistical analysis demonstrates that the performance of the final system with calibration performs according to the predictions of propagated

Kalman filter covariances. As an application, it is also shown that the resulting estimate is successfully integrated as a state feedback measurement for a steer-by-wire vehicle to virtually modify the vehicle's handling characteristics. With the improved sideslip angle estimate presented in this work, such a system can be easily implemented.

The accurate estimates of the vehicle states are available at a level previously unavailable and these estimates yield a new opportunity to estimate key vehicle parameters, such as vehicle mass, tire cornering stiffness, understeer gradient, roll stiffness, and roll damping coefficient. Once vehicle parameters are precisely estimated, parameterized vehicle dynamics models with properly estimated parameters can be used for a wide variety of applications including highway automation, vehicle stability control, and rollover prevention systems [10, 17, 38, 47, 53]. Aiming to provide parameter estimates precisely enough to be used for most vehicle dynamics and control problems, this thesis investigates vehicle parameter estimation schemes and demonstrates experimental results of the estimation schemes.

Furthermore, estimated vehicle parameters together with estimated sensor biases open the door to estimate vehicle states correctly even when GPS is not available. Parameterized vehicle models with properly estimated parameters can produce correct vehicle state estimates using INS sensors calibrated by the sensor bias estimates. This concept is illustrated in Fig. 1.5. When GPS is available, represented in the left side of the figure, vehicle parameters and INS sensor biases are estimated as well as vehicle states. When GPS is not available, represented in the right side, the estimated vehicle parameters and sensor biases are used as inputs to the estimation process to estimate vehicle states without help of GPS measurements.

In addition, based on the estimated parameters and states, this thesis presents a new method for separating road bank and suspension roll angle using a disturbance observer and a vehicle dynamic model. While a lumped value of road bank and suspension roll can be measured using a two-antenna GPS system and the lumped value can be used to compensate the acceleration measurements [41], the separation of these two angles could be especially beneficial to vehicle rollover warning and avoidance systems [10, 12, 24]. Since a small lumped value does not necessarily mean

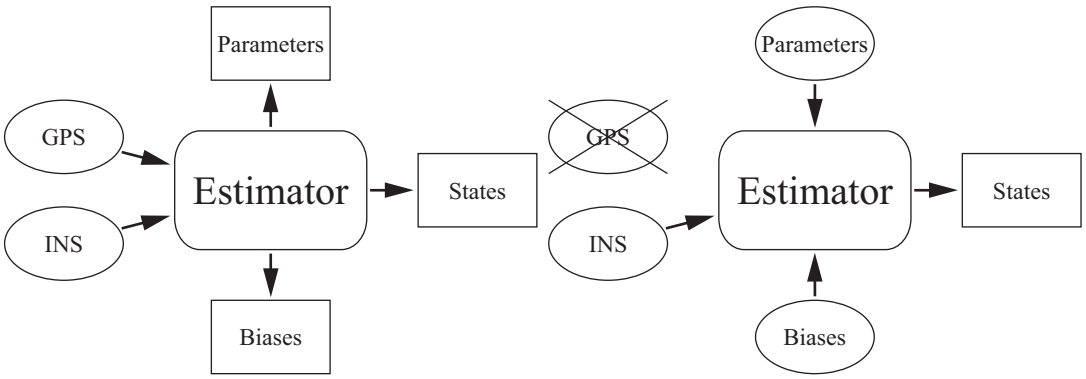

Figure 1.5: Estimation with/without GPS Availability

a small road bank angle, a vehicle may experience a significant road bank angle even though the sum of the two angles is small.

Although the suspension roll and road bank angles have similar influences on the roll and roll rate measurements, they play very different roles in the vehicle dynamics. While the road bank angle can be treated as a disturbance or unknown input to the vehicle, the suspension roll angle is a state resulting from the road bank angle and other inputs, governed by vehicle dynamics. This implies that a parameterized vehicle dynamic model could conceivably be used to separate the suspension roll and road bank angles. In this thesis, a dynamic model, which includes suspension roll as a state and road bank as a disturbance, is introduced. The disturbance observer is then implemented using the measurements of the sideslip angle, yaw rate, roll rate, and total roll angle (the sum of road bank and suspension roll angles) from the GPS/INS system. Using this structure, experimental results demonstrate that road bank angle and suspension roll can be effectively separated.

1.4 Thesis Contributions

The contributions of this thesis are as follows:

- Developed cascade state estimators for vehicle dynamics control, which systematically take care of sensor biases and unwanted effects from roll and pitch, using a two-antenna GPS receiver.

- Proved the convergence of the cascade estimators and verified the performance of the estimators by statistical analysis.
- Demonstrated the applicability of the estimators. Applied the estimated vehicle states as feedback signals to a linear controller, which virtually modifies a vehicle's handling characteristics.
- Developed parameter estimation methods for vehicle dynamic models using the estimated vehicle states, and contrasted the performance of these methods in several scenarios.
- Developed a vehicle dynamic model with proper treatment of the full 3D kinematic property of road bank, and estimated road bank separately from suspension roll.

1.5 Thesis Outline

Chapter 2 initiates the discussion of vehicle lateral dynamics by explaining fundamental concepts and introducing linear tire and vehicle models, which have been commonly adopted for vehicle dynamics control. The introduced models provide a basic idea of what states and parameters of a vehicle are important for vehicle dynamics control.

Chapter 3 then presents a method of estimating the vehicle states by combining automotive grade inertial sensors with a two-antenna GPS receiver. Cascade Kinematic Kalman filters that are independent of physical vehicle parameters are used to get high update rate estimates of the vehicle states by integrating the inertial sensors with the GPS receiver. The effects of pitch and roll on the measurements are compensated to improve the accuracy of the vehicle state and sensor bias estimates. In addition, the sensitivity and cross-coupling of inertial sensors are systematically calibrated to reduce measurement error further.

To show that the proposed estimation method is stable and gives appropriate state estimates for vehicle control purposes, Chapter 4 starts by proving the convergence

of the cascade filter structure. The performance of the estimation method is then verified by statistical analysis. Results from the statistical analysis match predictions from the Kalman filters well. Finally, the estimated vehicle states are used to modify a vehicle's handling characteristics through a full state feedback controller, which implies that the estimation method is applicable to a real-world vehicle controller.

The thesis then moves on to vehicle parameter estimation. Chapter 5 experimentally shows that key vehicle parameters, such as tire cornering stiffness, understeer gradient, yaw moment of inertia, and roll stiffness, can be estimated using the estimated vehicle states.

Based on the estimated states and parameters, Chapter 6 presents a new method for identifying road bank and suspension roll separately using a disturbance observer and a vehicle dynamic model. A dynamic model, which includes suspension roll as a state and road bank as a disturbance, is first developed, and a disturbance observer is then implemented from the vehicle model. Experimental results show that the suspension roll and road bank angles are estimated separately by the proposed estimation scheme. Chapter 7 concludes the thesis by summarizing the main results and suggesting possible directions for future work.

Chapter 2

Vehicle Dynamics

This chapter explains fundamental concepts of vehicle lateral dynamics by introducing linear tire and bicycle models, which have been commonly adopted for vehicle dynamics control. The introduced models help to get a basic idea of what states and parameters of a vehicle are important to implement vehicle dynamics control systems. This chapter also explains how the understeer gradient of a vehicle is defined. The understeer gradient is one of the most important vehicle properties which determine the handling characteristic of a vehicle and proves useful in discussing parameter estimation results.

2.1 Linear Tire Model

One of the most significant functions of a tire is to generate lateral forces to control the vehicle's direction. The tires of a vehicle produce lateral forces as they deform with slip angles as shown in Fig. 2.1. The slip angle, α, represents the angle between the tire's direction of travel and its longitudinal axis.

As the tire rolls, the tire contact patch over the ground deforms according to the direction of travel. This deformation and the elasticity of the tire produce the lateral tire force. Figure 2.2 shows experimental measurements of the lateral force supplied by a tire as a function of the slip angle [23]. In the linear region of the tire curve

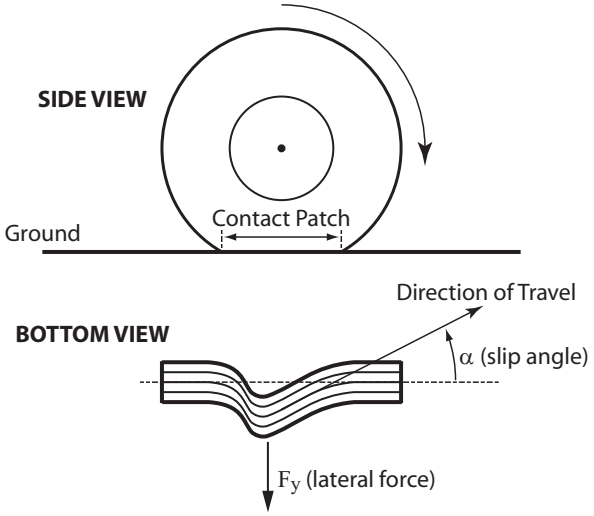

Figure 2.1: Rolling Tire Deformation and Lateral Force

(small slip angle), the lateral force of the tire can be modeled as:

$$F_y = -C_\alpha \alpha \tag{2.1}$$

where cornering stiffness, C_α, represents the slope of initial portion of the tire curve.

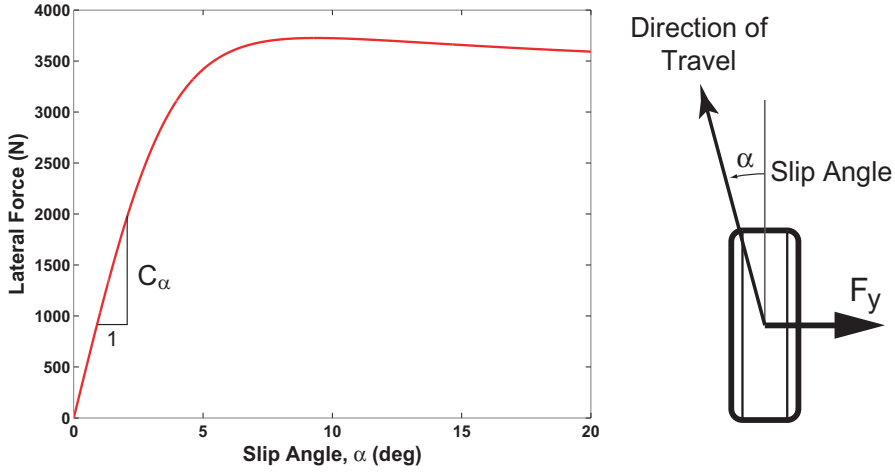

Figure 2.2: Tire Lateral Force and Slip Angle

2.2 Planar Bicycle Model

The lateral dynamics of a vehicle in the horizontal plane are represented here by the single track, or bicycle model with states of lateral velocity, u_y, and yaw rate, r. The bicycle model is a standard representation in the area of ground vehicle dynamics and has been used extensively in previous work [7, 16, 38, 46, 48, 54]. While detailed derivation and explanation can be found in many textbooks [14, 35], the underlying assumptions are that the slip angles on the inside and outside wheels are approximately the same and the effect of the suspension roll is small. These assumptions hold well for most typical driving situations and, in particular, for the test maneuvers used for validation in this thesis.

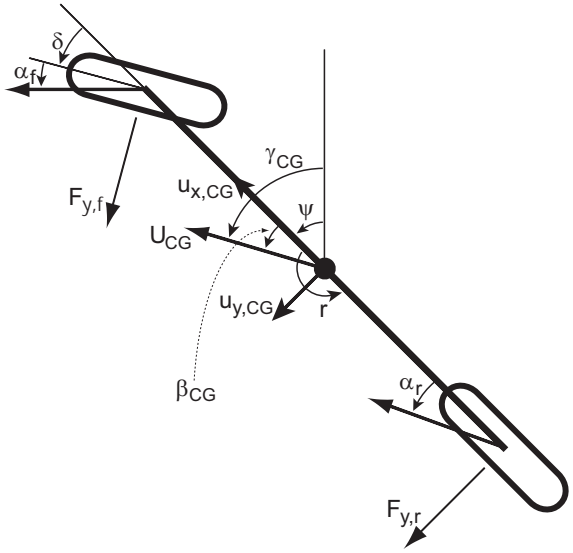

Figure 2.3: Bicycle Model

In Fig. 2.3, δ is the steering angle, u_x and u_y are the longitudinal and lateral components of the vehicle velocity, $F_{y,f}$ and $F_{y,r}$ are the lateral tire forces, and α_f and α_r are the tire slip angles. Derivation of the equations of motion for the bicycle model then follows from the following force and moment balances:

$$\begin{aligned} ma_y &= F_{y,f}\cos\delta + F_{y,r} \\ I_z\dot{r} &= aF_{y,f}\cos\delta - bF_{y,r} \end{aligned} \tag{2.2}$$

where I_z is the moment of inertia of the vehicle about its yaw axis, m is the vehicle mass, a and b are distance of the front and rear axles from the CG.

Using the linear tire model in Eq. (2.1), the front and rear tire forces, $F_{y,f}$ and $F_{y,r}$, become:

$$F_{y,f} = -C_{\alpha f}\alpha_f, \quad F_{y,r} = -C_{\alpha r}\alpha_r \tag{2.3}$$

where $C_{\alpha f}$ and $C_{\alpha r}$ are the total front and rear cornering stiffness. The assumption that both the slip angle and the cornering stiffness are approximately the same for the inner and outer tires on each axle is inherent in this equation.

Linearized with the small angles, the tire slip angles, α_f and α_r, can be written in terms of $u_{x,CG}$, $u_{y,CG}$, r, and δ:

$$\begin{aligned} \alpha_f &\approx \frac{u_{y,CG} + ar}{u_{x,CG}} - \delta \\ \alpha_r &\approx \frac{u_{y,CG} - br}{u_{x,CG}} \end{aligned} \tag{2.4}$$

The state equation for the bicycle model can be then written as:

$$\begin{bmatrix} \dot{u}_{y,CG} \\ \dot{r} \end{bmatrix} = \begin{bmatrix} \frac{-C_{\alpha f}-C_{\alpha r}}{mu_{x,CG}} & -u_{x,CG} + \frac{C_{\alpha r}b - C_{\alpha f}a}{mu_{x,CG}} \\ \frac{C_{\alpha r}b - C_{\alpha f}a}{I_z u_{x,CG}} & \frac{-C_{\alpha f}a^2 - C_{\alpha r}b^2}{I_z u_{x,CG}} \end{bmatrix} \begin{bmatrix} u_{y,CG} \\ r \end{bmatrix} + \begin{bmatrix} \frac{C_{\alpha f}}{m} \\ \frac{C_{\alpha f}a}{I_z} \end{bmatrix} \delta \tag{2.5}$$

Note that given the longitudinal and lateral velocities, u_x and u_y, at any point on the vehicle body, the sideslip angle can be defined by:

$$\beta = \tan^{-1}\left(\frac{u_y}{u_x}\right) \approx \frac{u_y}{u_x} \tag{2.6}$$

The sideslip angle at the center of gravity (CG) is shown by β_{CG} in Fig. 2.3. The sideslip angle at any point on the body can also be defined as the difference between the vehicle yaw angle (ψ) and the direction of the velocity (γ) at that point.

$$\beta = \gamma - \psi \tag{2.7}$$

Since a two-antenna GPS receiver provides both velocity and yaw angle measurements, the vehicle yaw angle and direction of the velocity can be directly measured. In the flat world of the bicycle model, therefore, the sideslip angle can be calculated by simply using Eq. (2.7). The errors introduced by this simplification are discussed in subsequent sections.

2.3 Understeer Gradient

The understeer gradient describes vehicle handling characteristics. Using the steady-state bicycle model, the understeer gradient can be determined from the weight distribution and the cornering stiffness. For a steady-state turning vehicle with a constant speed of V, lateral acceleration of the vehicle, a_{lat}, and the vehicle speed, V, can be written as:

$$a_{lat} = \frac{V^2}{R}, \quad V = Rr \tag{2.8}$$

where R is the radius of the turn. The steer angle, δ can be then derived from Eqs. (2.4), (2.6), and (2.8):

$$\begin{aligned}
\beta_{CG} &= \tan^{-1}\left(\frac{u_{y,CG}}{u_{x,CG}}\right) \approx \frac{u_{y,CG}}{u_{x,CG}} \approx \frac{u_{y,CG}}{V} \\
\alpha_f &\approx \beta_{CG} + \frac{ar}{V} - \delta = \beta_{CG} + \frac{a}{R} - \delta \\
\alpha_r &\approx \beta_{CG} - \frac{br}{V} = \beta_{CG} - \frac{b}{R} \\
\therefore \delta &\approx \frac{a+b}{R} - \alpha_f + \alpha_r = \frac{L}{R} - \alpha_f + \alpha_r
\end{aligned} \tag{2.9}$$

where L is the wheelbase.

The steady-state force and moment balances are from Eq. (2.2) with small angles.

$$\begin{aligned}
F_{y,f} + F_{y,r} &= m\frac{V^2}{R} \\
aF_{y,f} &= bF_{y,r}
\end{aligned} \tag{2.10}$$

The tire slip angles, α_f and α_r, can be calculated from the following equations using

the linear tire model in Eq. (2.3).

$$\begin{aligned} F_{y,f} &= \frac{b}{L}\frac{mV^2}{R} = \frac{W_r}{g}\frac{V^2}{R} = -C_{\alpha f}\alpha_f \\ F_{y,r} &= \frac{a}{L}\frac{mV^2}{R} = \frac{W_f}{g}\frac{V^2}{R} = -C_{\alpha r}\alpha_r \\ \because W_f &= \frac{b}{L}mg, \quad W_r = \frac{a}{L}mg \end{aligned} \tag{2.11}$$

where W_f and W_r are the vehicle loads on the front and rear axles respectively. Using Eq. (2.9), the steer angle is therefore given by:

$$\begin{aligned} \delta &= \frac{L}{R} - \alpha_f + \alpha_r = \frac{L}{R} + \left(\frac{W_f}{C_{\alpha f}} - \frac{W_r}{C_{\alpha r}}\right)\frac{V^2}{Rg} \\ &= \frac{L}{R} + K_{US}\frac{a_{lat}}{g} \end{aligned} \tag{2.12}$$

where

$$K_{US} = \frac{W_f}{C_{\alpha f}} - \frac{W_r}{C_{\alpha r}} = \text{understeering gradient in rad/g}$$

Equation 2.12 is very important to determine the handling characteristic of a vehicle. This equation determines how the steer angle should be changed according to the radius of turn and the lateral acceleration of the vehicle. If K_{US} is zero, the vehicle is called neutral steering and no change in steer angle on a constant radius turn is necessary even as the speed of the vehicle varies. If K_{US} is greater than zero, the vehicle is understeering and the steer angle should increase on a constant radius turn as the speed of the vehicle increases. Similarly, if K_{US} is less than zero, the vehicle is oversteering and the steer angle turn should decrease on a constant radius as the speed of the vehicle increases. The understeer gradient also affects the dynamic response of the vehicle. An understeering vehicle has system poles in the left half plane regardless of the vehicle speed, but the poles move further from the real axis and the response becomes oscillatory as the vehicle speed increases. On the other hand, poles of an oversteering vehicle move to the right half plane as the

speed increases. As a result, an understeering vehicle is always stable, but the vehicle response becomes oscillatory at higher speed, while an oversteering vehicle becomes unstable at higher speed.

Chapter 3

Vehicle State Estimation Using GPS

3.1 Introduction

While new steering and braking actuator designs provide new opportunities to shape vehicle dynamics through active control, the primary challenge in the development of vehicle control systems remains the lack of necessary feedback. In particular, the difficult problem of estimating the sideslip angle or lateral velocity of the vehicle currently limits the algorithms that can be incorporated in production systems [49]. Although vehicle stability and steering control systems require sideslip angle for their control purposes [17, 31, 38] and future steer-by-wire systems will require it for full-state feedback [54], current vehicles are not equipped with an ability to measure the sideslip angle directly. As a result, the sideslip angle must instead be estimated for vehicle control applications. Two common techniques for estimating the sideslip angle are integrating an automotive grade accelerometer and rate gyro directly and using a physical vehicle model as an observer [16, 17, 27]. Some methods use a combination or switch between these two methods appropriately based on vehicle states [17, 38]. While they have enabled vehicle dynamics control in series production, these solutions nevertheless have fundamental problems. Direct integration methods can accumulate error from sensor noise and unwanted measurements from road grade and bank angle

(superelevation) while methods based on a physical vehicle model can be sensitive to changes in the vehicle parameters and inaccurate on low friction surfaces [48]. The vehicle control systems of the future, therefore, will only be enabled by improvements in sensing.

This chapter presents a method of estimating sideslip angle and other vehicle states using a two-antenna GPS receiver which avoids these estimation errors. Since a two-antenna GPS receiver provides direct measurements of vehicle velocity and attitude (yaw and roll) in addition to position information, key vehicle states including sideslip angle can be estimated using GPS velocity and attitude measurements. The GPS measurements are combined with automotive grade inertial sensors to get high update rate estimates of the vehicle.

3.1.1 Chapter Outline

This chapter first starts with a brief description of general Kalman filter structure, which is used to integrate inertial sensors with GPS for state estimation throughout the whole chapter. This chapter then investigates a state estimation method using a planar vehicle model, which does not consider road grade and vehicle roll. These estimation results show that the effects of grade and roll create significant error in sideslip angle estimation. To avoid estimation error caused by road grade and vehicle roll, a roll center model of the vehicle with road grade is introduced. A road grade estimate is derived from GPS velocity. The estimate combined with roll information from the two-antenna system is used to improve the accuracy of the vehicle state and sensor bias estimates. As a final refinement step, this chapter provides calibration procedures for the sensitivity and cross-coupling of inertial sensors to reduce estimation error further.

3.2 GPS/INS Integration Using Kalman Filters

3.2.1 General Kalman Filter Structure

Because the update rate of most GPS receivers is not high enough for control purposes [7], INS sensors are commonly integrated with GPS measurements in a Kalman filter structure to provide higher update rate estimates of the vehicle states. While the filter could be based around the physical model in Eq. (2.5), there are some drawbacks to such an approach. Since this model is valid only in the linear region and the parameters involve significant uncertainty, particularly with respect to tire stiffnesses, a Kalman filter built on this model may possess significant estimation error. With the two antenna GPS system, however, it is possible to use two kinematic models, independent of any physical parameter uncertainties and changes, in the state estimator.

The traditional Kalman filter is comprised of a measurement update and a time update [22, 45]. Because of the lower update rate of the GPS measurement, the measurement update is performed only when GPS is available in order to estimate the sensor bias and minimize the state estimation error. The measurement update is generally described by:

$$\begin{aligned} x_t(+) &= x_t(-) + K_t\left(y_t - Cx_t(-)\right) \\ K_t &= P_t(-)C^T\left(CP_t(-)C^T + R\right) \quad \text{or} \quad K_t = P_t(+)C^TR^{-1} \\ P_t(+) &= \left(I - K_tC\right)P_t(-) \quad \text{or} \quad P_t(+)^{-1} = P_t(-)^{-1} + C^TR^{-1}C \end{aligned} \tag{3.1}$$

where

$x_t(-)$ = prior estimate of system state at time t

$x_t(+)$ = updated estimate of system state at time t

$P_t(-)$ = prior error covariance matrix at time t

$P_t(+)$ = updated error covariance matrix at time t

K_t = Kalman Gain at time t

y_t = new measurement at time t

C = observation matrix

R = measurement noise covariance matrix

Here x and y represent vehicle states of interest and available measurements, respectively, for a general filter. Simple integration of the inertial sensors is performed during the time update because GPS measurements are not available. Using the discrete model of a sampled-data system, the time update can be written as:

$$\begin{aligned} x_{t+1}(-) &= A_d x_t(+) + B_d u_t \\ P_{t+1}(-) &= A_d P_t(+) A_d^T + Q \end{aligned} \tag{3.2}$$

where

$$A_d = e^{A\Delta T} = \sum_{k=0}^{\infty} \frac{A^k \Delta T^k}{k!}$$

$$B_d = \int_0^{\Delta T} e^{A\eta}\, \mathrm{d}\eta\, B = \sum_{k=0}^{\infty} \frac{A^k \Delta T^{k+1}}{(k+1)!} B$$

u_t = input to system at time t

Q = process noise covariance matrix

This Kalman filter structure is used for all of the individual filters throughout the whole chapter.

3.2.2 State Estimation with Simple Planar Vehicle Model

In previous work with GPS for sideslip estimation [7], the vehicle yaw angle was estimated by integrating a yaw gyro. This is not an ideal approach, however, since the estimate must be periodically reset while driving straight in order to prevent integration of gyro bias error from producing large, fictitious sideslip values. The addition of a two-antenna GPS receiver solves this problem by providing an absolute attitude reference and the opportunity to neatly decouple the estimation problem into two

simple Kalman filters. One is used to estimate the vehicle yaw angle without errors arising from gyro integration. The other is used to estimate absolute longitudinal and lateral velocities of the vehicle without using wheel speed sensors, thus avoiding error caused by wheelslip.

For the yaw Kalman filter, the kinematic relationship between the yaw rate measurements and the yaw angle can be written as:

$$r_m = \dot{\psi} + r_{bias} + noise \tag{3.3}$$

where

$\psi =$ yaw angle of vehicle

$r_m,\ r_{bias} =$ yaw rate gyro measurement and bias

The yaw angle can be measured using a two-antenna GPS receiver.

$$\psi_m^{GPS} = \psi + noise \tag{3.4}$$

where

$\psi_m^{GPS} =$ yaw angle measurement from GPS

A linear dynamic system can be constructed from Eqs. (3.3) and (3.4) using the inertial sensor as the input and GPS as the measurement.

$$\begin{bmatrix} \dot{\psi} \\ \dot{r}_{bias} \end{bmatrix} = \begin{bmatrix} 0 & -1 \\ 0 & 0 \end{bmatrix} \begin{bmatrix} \psi \\ r_{bias} \end{bmatrix} + \begin{bmatrix} 1 \\ 0 \end{bmatrix} r_m + noise \tag{3.5}$$

When GPS attitude measurements are available,

$$\psi_m^{GPS} = \begin{bmatrix} 1 & 0 \end{bmatrix} \begin{bmatrix} \psi \\ r_{bias} \end{bmatrix} + noise \tag{3.6}$$

The Kalman filter in Eqs. (3.1) and (3.2) is then applied to the system to obtain the vehicle yaw angle and the gyro bias. Using Eq. (3.2), a discrete representation of sampled Eq. (3.5) can be written exactly as:

$$\begin{aligned} x_{t+1}(-) &= A_d x_t(+) + B_d u_t \\ A_d &= e^{A\Delta T} = \sum_{k=0}^{\infty} \frac{A^k \Delta T^k}{k!} = \begin{bmatrix} 1 & -\Delta T \\ 0 & 1 \end{bmatrix} \\ B_d &= \int_0^{\Delta T} e^{A\eta}\, \mathrm{d}\eta\, B = \sum_{k=0}^{\infty} \frac{A^k \Delta T^{k+1}}{(k+1)!} B = \begin{bmatrix} \Delta T \\ 0 \end{bmatrix} \end{aligned} \tag{3.7}$$

The state vector, x, in this Kalman filter is $[\ \psi \quad r_{bias}\ ]^T$, the input, u, is the measured yaw rate r_m from the yaw rate gyro. The measurement y in the Kalman filter is the yaw angle from GPS, ψ_m^{GPS}, with observation matrix C, which is $[\ 1 \quad 0\ ]$ only when GPS measurements are available. The observation matrix, C, is $[\ 0 \quad 0\ ]$ when GPS measurements are not available since the system simply integrates the gyro in this case.

For the velocity Kalman filter, the kinematic relationship between acceleration measurements and velocity components at the point where the sensor is located can be written as:

$$\begin{aligned} a_{x,m} &= \dot{u}_{x,sensor} - \dot{\psi} u_{y,sensor} + a_{x,bias} + noise \\ a_{y,m} &= \dot{u}_{y,sensor} + \dot{\psi} u_{x,sensor} + a_{y,bias} + noise \end{aligned} \tag{3.8}$$

where

$u_{x,sensor}$ = longitudinal velocity at sensor location

$a_{x,m},\ a_{x,bias}$ = longitudinal accelerometer measurement and bias

$u_{y,sensor}$ = lateral velocity at sensor location

$a_{y,m},\ a_{y,bias}$ = lateral accelerometer measurement and bias

The longitudinal and lateral velocity can be estimated using GPS velocity together

with the yaw Kalman filter. First, the sideslip angle, β^{GPS}, needs to be calculated using the velocity vector, U^{GPS}, from the GPS measurement and the vehicle yaw angle, ψ, from the yaw Kalman filter by Eq. (2.7). Then, the longitudinal velocity measurement, $u_{x,m}^{GPS}$, and lateral velocity measurement, $u_{y,m}^{GPS}$, are simply:

$$\begin{aligned} u_{x,m}^{GPS} &= \left\| U^{GPS} \right\| \cos(\beta^{GPS}) \\ u_{y,m}^{GPS} &= \left\| U^{GPS} \right\| \sin(\beta^{GPS}) \end{aligned} \tag{3.9}$$

Assuming that the primary GPS antenna giving velocity measurements is placed directly above the INS sensor location, the measured velocity components from GPS can be written as:

$$\begin{aligned} u_{x,m}^{GPS} &= u_{x,sensor} + noise \\ u_{y,m}^{GPS} &= u_{y,sensor} + noise \end{aligned} \tag{3.10}$$

where

$$\begin{aligned} u_{x,m}^{GPS} &= \text{longitudinal velocity measurement from GPS} \\ u_{y,m}^{GPS} &= \text{lateral velocity measurement from GPS} \end{aligned}$$

Note that Eq. (3.10) holds only when the primary GPS antenna is located above the sensor location. If it is not, an additional velocity term from the yaw rate must be taken into account.

A Kalman filter is then applied to the following linear dynamic system from Eqs. (3.8) and (3.10) to obtain the vehicle velocities and the sensor biases.

$$\begin{bmatrix} \dot{u}_{x,sensor} \\ \dot{a}_{x,bias} \\ \dot{u}_{y,sensor} \\ \dot{a}_{y,bias} \end{bmatrix} = \begin{bmatrix} 0 & -1 & r & 0 \\ 0 & 0 & 0 & 0 \\ -r & 0 & 0 & -1 \\ 0 & 0 & 0 & 0 \end{bmatrix} \begin{bmatrix} u_{x,sensor} \\ a_{x,bias} \\ u_{y,sensor} \\ a_{y,bias} \end{bmatrix} + \begin{bmatrix} 1 & 0 \\ 0 & 0 \\ 0 & 1 \\ 0 & 0 \end{bmatrix} \begin{bmatrix} a_{x,m} \\ a_{y,m} \end{bmatrix} + noise \tag{3.11}$$

where

$$r = \dot{\psi} = r_m - r_{bias} = \text{compensated yaw rate}$$

When GPS velocity measurements are available,

$$\begin{bmatrix} u_{x,m}^{GPS} \\ u_{y,m}^{GPS} \end{bmatrix} = \begin{bmatrix} 1 & 0 & 0 & 0 \\ 0 & 0 & 1 & 0 \end{bmatrix} \begin{bmatrix} u_{x,sensor} \\ a_{x,bias} \\ u_{y,sensor} \\ a_{y,bias} \end{bmatrix} + noise \tag{3.12}$$

The state vector, x, is $[\ u_{x,sensor} \quad a_{x,bias} \quad u_{y,sensor} \quad a_{y,bias}\ ]^T$ and the measurement, y, is $[\ u_{x,m}^{GPS} \quad u_{y,m}^{GPS}\ ]^T$ in the Kalman filter of Eqs. (3.1) and (3.2). The discrete state space form of Eq. (3.11) can be represented exactly as:

$$\begin{aligned} A_d &= e^{A\Delta T} = \sum_{k=0}^{\infty} \frac{A^k \Delta T^k}{k!} \\ &= \begin{bmatrix} \cos(r\Delta T) & \frac{-\sin(r\Delta T)}{r} & \sin(r\Delta T) & \frac{\cos(r\Delta T)-1}{r} \\ 0 & 1 & 0 & 0 \\ -\sin(r\Delta T) & \frac{1-\cos(r\Delta T)}{r} & \cos(r\Delta T) & \frac{\sin(r\Delta T)}{r} \\ 0 & 0 & 0 & 1 \end{bmatrix} \\ B_d &= \int_0^{\Delta T} e^{A\eta}\, \mathrm{d}\eta\, B = \sum_{k=0}^{\infty} \frac{A^k \Delta T^{k+1}}{(k+1)!} B = \begin{bmatrix} \frac{\sin(r\Delta T)}{r} & \frac{1-\cos(r\Delta T)}{r} \\ 0 & 0 \\ \frac{\cos(r\Delta T)-1}{r} & \frac{\sin(r\Delta T)}{r} \\ 0 & 0 \end{bmatrix} \end{aligned} \tag{3.13}$$

3.3 Experimental Result with Planar Model

While the estimator in the previous section is quite simple, it relies heavily on the assumption that motion occurs only in the plane. To determine the validity of this assumption, a series of experiments was performed on a Mercedes E-class wagon shown in Fig. 3.1 The test vehicle is equipped with a 3-axis automotive-grade accelerome-

Figure 3.1: Test Vehicle with Two-Antenna GPS Set-up

ter/rate gyro triad sampled at 100 Hz. Sensor noise levels (1σ) are 0.05 m/s^2 for the accelerometers and 0.2 deg/s for the rate gyros. The vehicle is also equipped with Novatel GPS antenna/receiver pairs, providing 10 Hz velocity measurements and 5 Hz attitude measurements with a noise level (1σ) of less than 3 cm/s and 0.25 deg respectively. (Figure 3.1 shows three GPS antennas, but the third one is a redundant one. The system can be implemented using only two antennas.)

Because the GPS receiver introduces a half sample period inherent latency and a finite amount of time is needed for computation and data transfer, the time tags in the GPS measurement messages and the synchronizing pulse from the receiver are used to align the GPS information with the inertial sensor measurements. This synchronizing process is very important when the inertial sensors are combined with the GPS measurements, because any time offset between two measurements may result in significant overall estimation errors [7].

Figure 3.2 shows yaw angle estimates compared to raw GPS measurements from

the two-antenna GPS system. Experimental tests consisting of several laps around an uneven parking lot are performed. Note that integration of inertial sensors fills in the gaps between GPS measurements. Even though the update rate of the GPS measurements is not high enough for vehicle control purposes, the combination of GPS measurements with inertial measurements provides estimates with sufficient bandwidth for vehicle control applications [7].

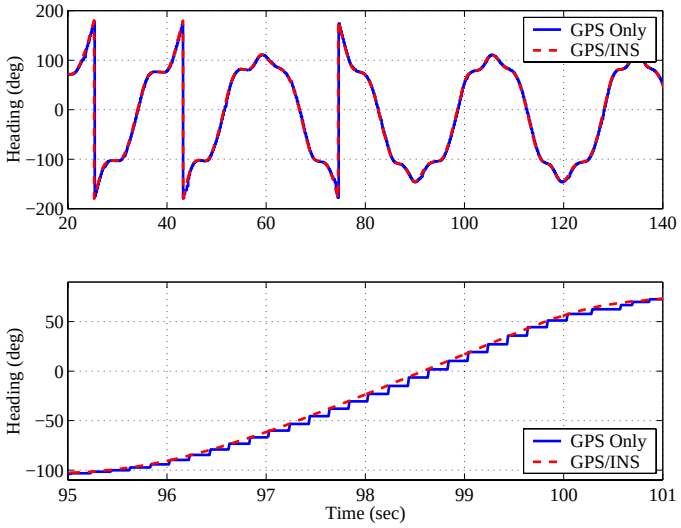

Figure 3.2: Yaw Angle Estimates

Figure 3.3 compares yaw rate and sideslip angle estimates from the GPS/INS integration with the simulation results from a carefully calibrated bicycle model. Since the velocity Kalman filter provides the velocity at the sensor location, the velocity estimates are translated to the center of gravity with the yaw rate in order to compare sideslip angle with the bicycle model. The similarity between the estimated and model yaw rates demonstrates that the bicycle model used in the comparison is indeed calibrated for the vehicle. In contrast, there are differences between estimated and modeled sideslip angles. Even though the estimated sideslip is still much better than that obtained from simply integrating the accelerometer [7] – the slip angle estimate is quite clean and does not drift – the accuracy is less than would be desired for control purposes. Not surprisingly, these differences are consistent with the uneven

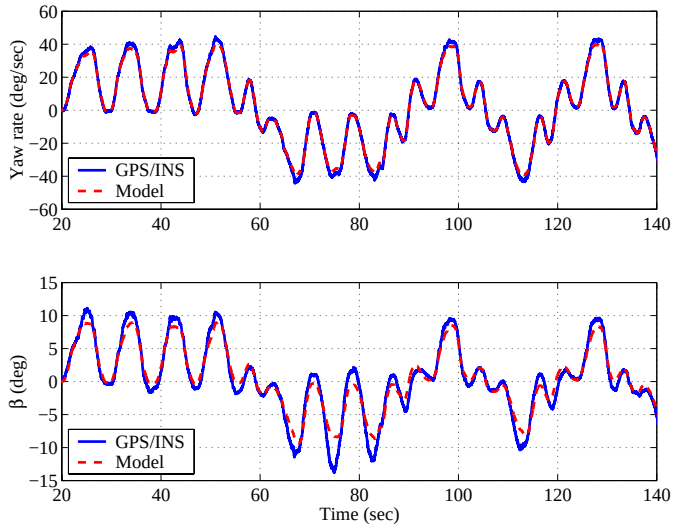

Figure 3.3: Yaw Rate and Sideslip Angle Estimates

grade and bank angle of the test path – factors neglected in the assumption of planar motion. The correlation between these differences and unevenness of the surface can be seen easily by comparing the accelerometer biases with the surface grade and suspension roll.

Although some caveats are noted later in the chapter, the surface grade can in general be estimated by examining the ratio of the vertical velocity obtained from GPS to the horizontal GPS velocity [3].

$$\theta_r \approx \tan^{-1}\left(\frac{U_V}{U_H}\right) \tag{3.14}$$

where

θ_r = road grade estimate

$U_V,\ U_H$ = vertical and horizontal velocity from GPS

Figure 3.4 shows the strong correlation between the longitudinal accelerometer bias and the grade along the test path calculated according to the velocity ratio. As

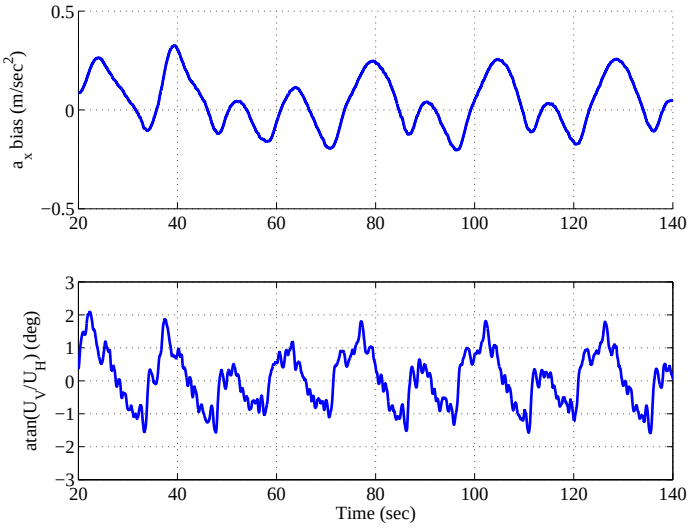

Figure 3.4: Longitudinal Accelerometer Bias and Grade Estimates

would be expected, the longitudinal accelerometer bias term reflects the component of gravitational acceleration entering as a result of the grade.

Since the two antennas of the GPS receiver are placed laterally, the combination of road bank angle (sometimes called side-slope or superelevation) and suspension roll can be directly measured. As shown in Fig. 3.5, the lateral accelerometer bias and the roll angle show the same correlation as the longitudinal values. The rationale is exactly the same since roll causes a component of the gravitational acceleration to enter the lateral acceleration measurement.

3.4 Improved Model: Roll Center Model with Road Grade

For a more accurate estimation of the slip angle it is necessary to compensate for the effects of vehicle pitch and roll. While this could be accomplished in a number of ways – such as incorporating a 3 or 4 antenna GPS system for 3D attitude measurement – basic estimates of roll and grade are available with the existing sensor suite. Assuming

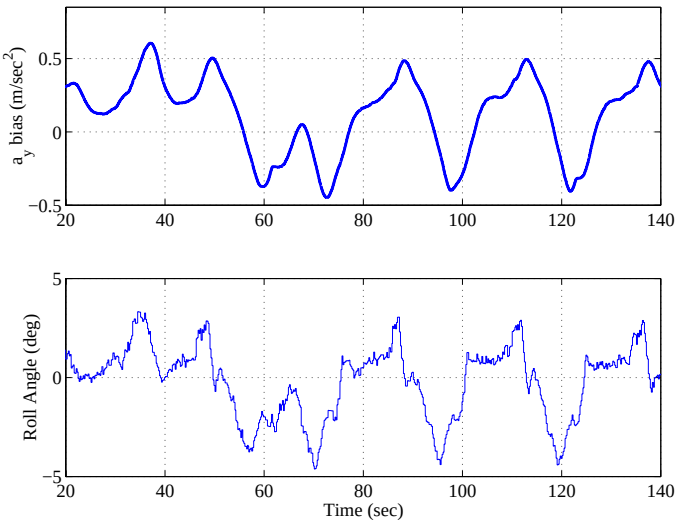

Figure 3.5: Lateral Accelerometer Bias Estimates and Roll Angle Measurements

that vehicle pitch is caused mostly by road grade, and that grade can be estimated by examining the velocity ratio using Eq. (3.14), gravity components in acceleration measurements due to pitch and roll can be compensated using only a two-antenna GPS receiver. Thus the measurements used to demonstrate the correlation between sensor biases and road geometry in the previous section can be harnessed to remove these effects.

A roll center vehicle model with a road grade and a bank angle is shown in Fig. 3.6. This model assumes that the vehicle body rotates about a fixed point (the roll center) on a frame that remains in the plane of the road. The expected gravity component in the acceleration measurement can be explicitly specified and compensated in Eq. (3.8) because the grade of the surface can be estimated from the GPS velocity measurement and the total roll angle (the sum of the suspension roll angle and the bank angle or superelevation of the surface) can be measured utilizing the two-antenna GPS receiver.

The kinematic relationship between acceleration measurements and velocity components at the sensor location for this model can be written as:

$$a_{x,m} = \dot{u}_{x,sensor} - \dot{\psi} u_{y,sensor} + a_{x,bias} + g \sin\theta_r + noise$$

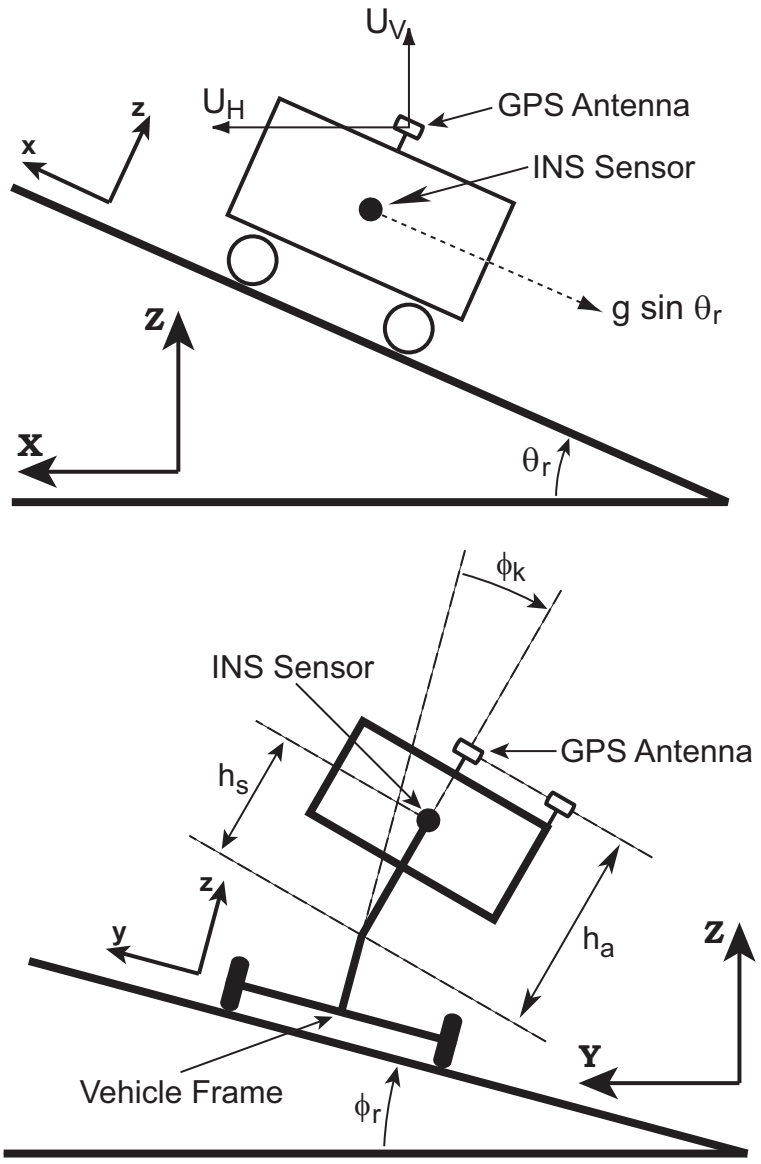

Figure 3.6: Roll Center Model with Grade and Bank Angle

$$a_{y,m} = \dot{u}_{y,sensor} + \dot{\psi} u_{x,sensor} + a_{y,bias} + g \sin\phi + noise \tag{3.15}$$

where

θ_r = road grade estimate

$\phi = \phi_r + \phi_k$ = sum of road bank and suspension roll

These additional terms can easily be included in the Kalman filter from Eqs. (3.11), (3.12), and (3.14). Equation (3.11) is written assuming road grade and bank angle changes are small and extra terms due to rotating frames such as the Coriolis forces are negligible.

Another important advantage in using the roll center model is that the roll motion of vehicle can be taken into account when determining vehicle velocity. Note that Eq. (3.15) is written for the point at which the sensor is located and the two GPS antennas are placed on the top of the vehicle roof. Therefore, there is an additional velocity component due to vehicle yaw and roll in the GPS velocity measurement. This can be included by translating the velocity at the antenna to the point at which the sensor is located using Eq. (3.16) under the assumption of small road grades and bank angles.

$$\begin{aligned} u_{x,m}^{GPS} &= u_{x,sensor} + r(h_a - h_s)\sin\phi_k + noise \\ &\approx u_{x,sensor} + noise \\ u_{y,m}^{GPS} &= u_{y,sensor} - p(h_a - h_s)\cos\phi_k + noise \\ &\approx u_{y,sensor} - p(h_a - h_s) + noise \end{aligned} \tag{3.16}$$

where

r = yaw rate

p = roll rate

h_a = distance from roll center to GPS antenna

h_s = distance from roll center to INS sensor

Since the suspension roll angle is small, the additional velocity component is negligible relative to the vehicle longitudinal velocity. However, the additional velocity component due to the roll rate should be considered in the lateral direction since the lateral velocity is comparably small. This roll rate compensation plays an important role when the vehicle is experiencing a heavy roll motion. If the primary GPS antenna is not placed directly above the inertial sensor, the yaw rate of the vehicle should also be taken into account in the lateral velocity measurement.

In addition, the sum of the road bank angle and the suspension roll can be estimated by constructing a roll Kalman filter in the same manner as in the yaw Kalman filter. Since the GPS antennas and roll gyro are attached to the vehicle body, only the sum of the road bank angle and the suspension roll angle can be measured without additional modeling. For the roll Kalman filter, the kinematic relationship between roll rate measurements and roll angle can be written as:

$$p_m = \dot{\phi} + p_{m,err} + noise \tag{3.17}$$

where

$$p_m,\ p_{m,err} = \text{roll rate gyro measurement and error}$$

Here, $p_{m,err}$ represents the roll rate measurement error from the gyro bias and extra roll rate term from road and vehicle kinematics. This extra roll term is explained and exactly defined in Eqs. (6.13) and (6.15). The roll angle can be measured using a two-antenna GPS receiver:

$$\phi_m^{GPS} = \phi + noise \tag{3.18}$$

where

$$\phi_m^{GPS} = \text{roll angle measurement from GPS}$$

The roll Kalman filter is then implemented using Eqs. (3.17) and (3.18) in the same manner as in the yaw Kalman filter. The state vector, x, is $[\ \phi \quad p_{bias}\ ]^T$ and the measurement, y, is the roll angle from GPS, ϕ_m^{GPS}.

3.5 Experimental Results with Roll Model

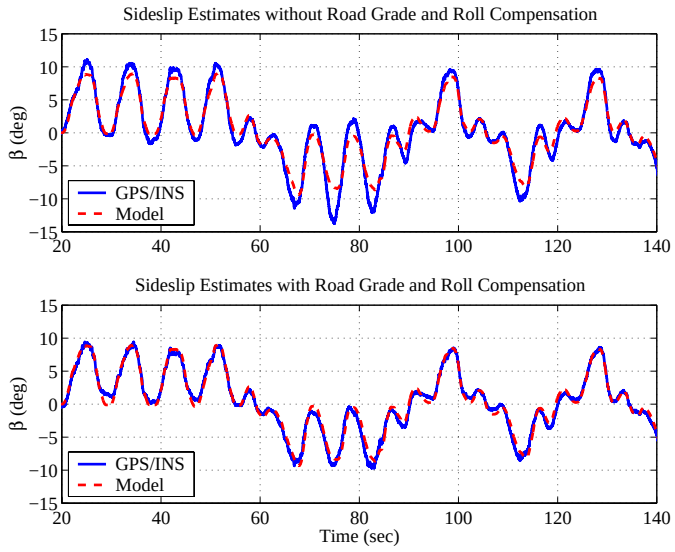

Figure 3.7: Comparison of Sideslip Angle Estimates

Figure 3.7 shows the experimental results of sideslip angle estimation with and without the compensation. Since the velocity Kalman filter provides the velocity at the sensor location, whereas the bicycle model generates the sideslip angle at the center of gravity, the velocity estimates from the filter are translated with yaw and roll rates to the corresponding point on the vehicle frame for the comparison with the bicycle model. Note that the discrepancies between the model and estimate are significantly reduced after the compensation. The same improvement can be seen in the case of longitudinal velocity estimation shown in Fig. 3.8. Differences between the longitudinal velocity estimate and wheel speed after the compensation are, in fact, due to longitudinal slip of the tire.

The combination of road bank angle and suspension roll angle is also estimated using the roll Kalman filter. Figure 3.9 shows roll estimates together with raw GPS roll measurements. Integration of INS sensors fills in the gaps between GPS measurements giving a smooth roll signal.

With accurate measurements of roll angle and roll rate, it is possible to estimate

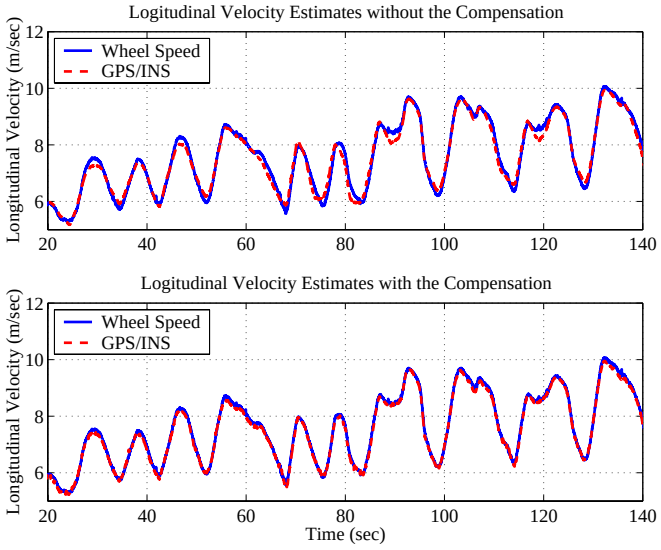

Figure 3.8: Longitudinal Velocity Estimates

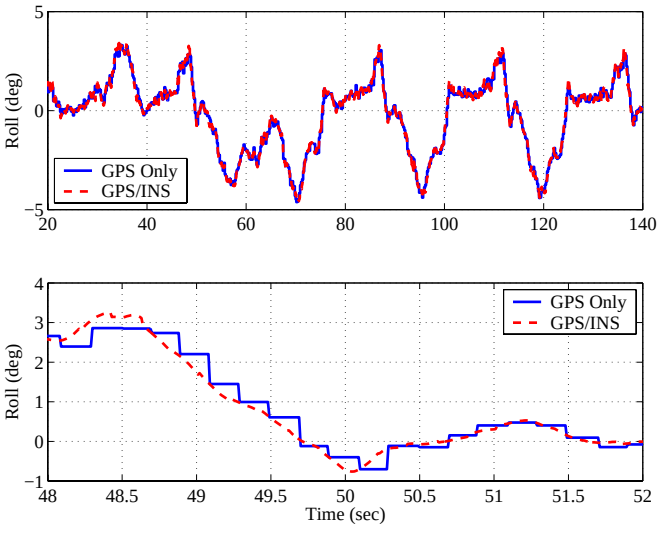

Figure 3.9: Roll Angle Estimates

parameters related to the roll dynamics such as roll stiffness and damping ratio [42]. A dynamic roll model can be used for a wide variety of applications including rollover prevention [10] or active suspension control. In addition, a parameterized vehicle roll dynamic model could conceivably be used to separate roll and bank angle.

3.6 Further Refinements

3.6.1 Gyro Sensitivity Effects and Estimation

After the compensation for grade and roll described in the previous sections, both sideslip angle and yaw rate estimates match the model predicted values very well, suggesting that the proposed scheme can correct for changes in grade and roll. However, the estimated sensor biases show significant variations over a short period of time, which is not consistent with the bias estimates representing true sensor biases. These variations can be seen in the following typical experimental results. As Fig. 3.10 illustrates, considerable low frequency variation exists in the estimated accelerometer bias after compensating for road grade and roll.

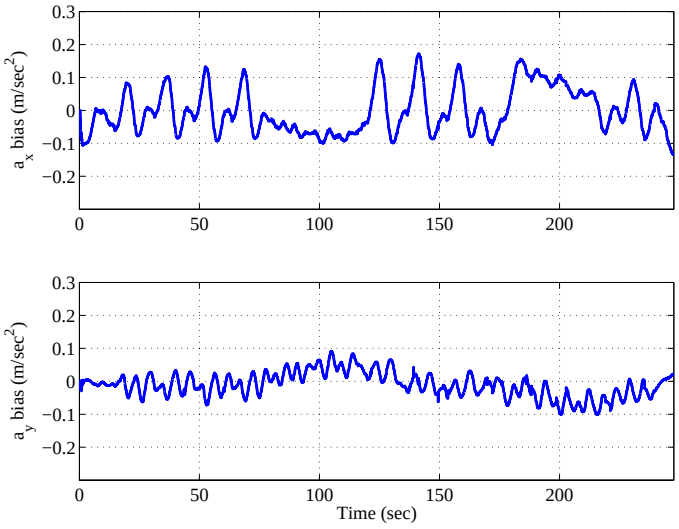

Figure 3.10: Estimated Accelerometer Biases

Similar variations can be also seen in the estimated yaw gyro bias in Fig. 3.11. While the bias variation is significant, it is interesting to note that the bias is strongly

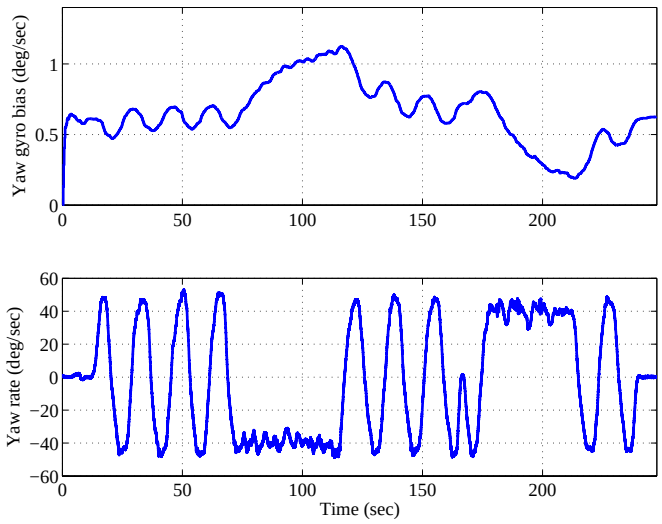

Figure 3.11: Estimated Yaw Gyro Bias and Yaw Rate

correlated with the yaw rate. In other words, the yaw gyro bias increases or decreases depending on the sign of the yaw rate. The yaw gyro bias increases when the yaw rate is negative and decreases when the yaw rate is positive. This can easily be seen in Fig. 3.11 at around 100 and 200 seconds.

The dependency of the bias on the sign of the yaw rate implies that there is an error in the sensitivity (scale factor) of the yaw rate gyro. In order to resolve this problem, a new sensor kinematic relationship that includes both sensitivity and bias is used:

$$r_m = s_r\dot{\psi} + r_{bias} + w_{r,m} \tag{3.19}$$

where

s_r = yaw rate gyro sensitivity

$w_{r,m}$ = yaw rate measurement (gyro) noise

Taking Eq. (3.19) into account, the system model becomes:

$$\frac{\mathrm{d}}{\mathrm{d}t}\begin{bmatrix} \psi \\ 1/s_r \\ r_{bias}/s_r \end{bmatrix} = \begin{bmatrix} 0 & r_m & -1 \\ 0 & 0 & 0 \\ 0 & 0 & 0 \end{bmatrix}\begin{bmatrix} \psi \\ 1/s_r \\ r_{bias}/s_r \end{bmatrix} + \begin{bmatrix} w_{r,m} \\ w_{sr} \\ w_{r,bias} \end{bmatrix} \tag{3.20}$$

where

$$s_r = \text{yaw rate gyro sensitivity}$$
$$w_{sr},\ w_{r,bias} = \text{process noise}$$

The yaw Kalman filter can then be constructed using Eq. (3.20) in place of Eq. (3.5). With this structure, the sensitivity and bias of the yaw rate gyro are estimated together; the results are shown in Fig. 3.12. The estimated bias with

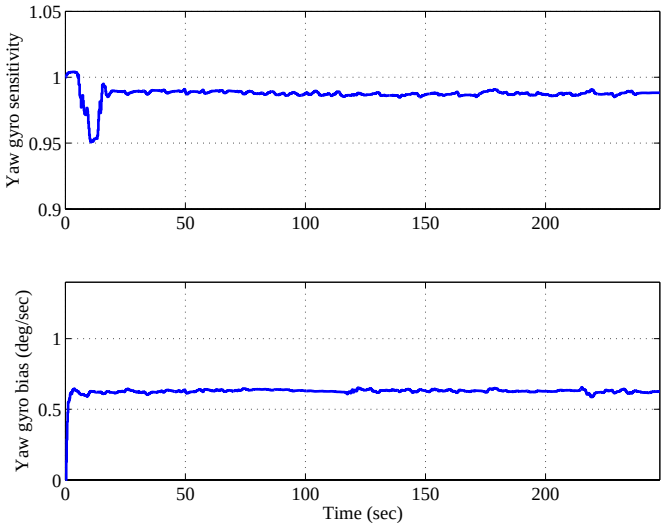

Figure 3.12: Estimated Yaw Gyro Sensitivity and Bias

the sensitivity estimation shows much less variation and appears to have acceptable performance for use in chassis control systems. Although the sensitivity is only observable when the vehicle is maneuvering, its value changes very slowly in the sensors used in this work. Thus some heuristics can be used to estimate the sensitivity on

the first few turns a vehicle makes (and perhaps occasionally update this value over the course of a trip) before returning to the original filter structure.

3.6.2 Removing Cross-Coupling in Accelerometers

Since the yaw angle and yaw rate are coupled with the longitudinal and lateral velocities, the accelerometer biases are altered when the filter calibrates the correct yaw gyro sensitivity. The estimated longitudinal and lateral accelerometer biases with the new yaw filter are shown in Fig. 3.13.

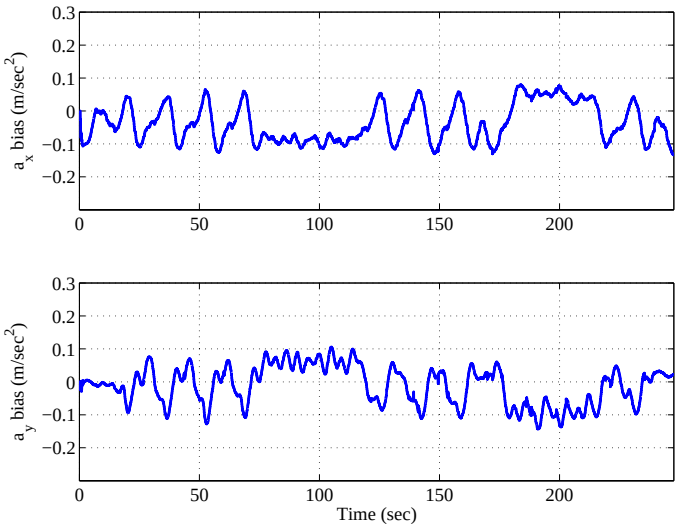

Figure 3.13: Estimated Accelerometer Biases with New Yaw Angle Estimation

Comparing with the previous results in Fig. 3.10, little improvement can be seen in these biases. In fact, the a_y bias looks even worse. However, these bias variations can also be explained by correlation with other signals. Figure 3.14 compares the longitudinal biases with the measured lateral acceleration, showing the similarity between the two signals. Since the longitudinal accelerometer is not exactly aligned with the vehicle's longitudinal axis, the longitudinal accelerometer picks up not only longitudinal acceleration but also lateral acceleration. Therefore, a cross-coupled lateral acceleration component shows up as in the longitudinal accelerometer bias.

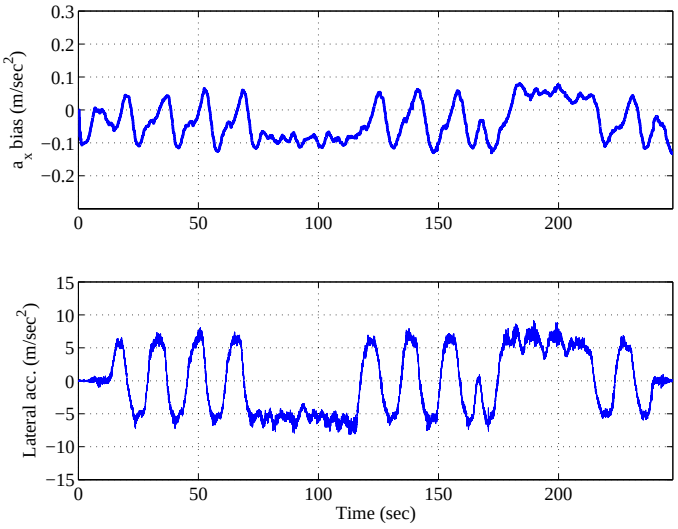

Figure 3.14: Longitudinal Accelerometer Bias and Lateral Acceleration

This component can be explicitly specified and compensated in the previous kinematic relationship for the longitudinal accelerometer.

$$a_{x,m} = \dot{u}_{x,sensor} - \dot{\psi} u_{y,sensor} + a_{x,bias} + g \sin\theta_r + c_{x,y} a_{y,ef} + w_{ax,m} \tag{3.21}$$

where

$$\begin{aligned} c_{x,y} &= \text{cross-coupling coefficient from } a_y \text{ to } a_x \\ a_{y,ef} &= \dot{u}_{y,sensor} + \dot{\psi} u_{x,sensor} + g \sin\phi \\ &= \text{effective acceleration along lateral axis} \\ w_{ax,m} &= a_x \text{ measurement (accelerometer) noise} \end{aligned}$$

Figure 3.15 shows the comparison between lateral accelerometer bias and lateral acceleration. As in the case of the gyro, the lateral accelerometer bias variation has a dependency on the lateral acceleration, which implies there is an error in the sensitivity of the lateral accelerometer. As with the gyro sensitivity estimation, a new

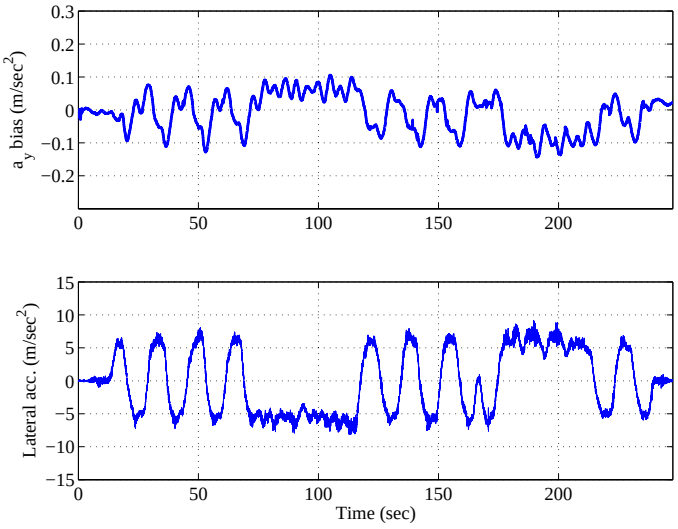

Figure 3.15: Lateral Accelerometer Bias and Lateral Acceleration

sensor kinematic relationship that includes both sensitivity and bias can be defined:

$$a_{y,m} = s_{ay}\left(\dot{u}_{y,sensor} + \dot{\psi}u_{x,sensor} + g\sin\phi\right) + a_{y,bias} + w_{ay,m} \tag{3.22}$$

where

$$s_{ay} = \text{lateral accelerometer sensitivity}$$
$$w_{ay,m} = a_y \text{ measurement (accelerometer) noise}$$

In order to estimate the cross-coupling coefficient, $c_{x,y}$, Eq. (3.21) can be integrated and rearranged by defining a term, $\Delta u_x(t)$.

$$\begin{aligned}\Delta u_x(t) &= u_{x,acc}(t) - u_{x,sensor}(t) + \int_0^t \left(\dot{\psi}u_{y,sensor} - g\sin\theta_r\right)\,\mathrm{d}t^* \\ &= a_{x,bias}t + c_{x,y}\int_0^t a_{y,ef}\,\mathrm{d}t^* + \Delta u_{x,0} + noise \end{aligned} \tag{3.23}$$

where

$$\begin{aligned} u_{x,acc}(t) &= \int_0^t a_{x,m}\,\mathrm{d}t^* \\ &= \text{longitudinal velocity from integrating } a_x \text{ measurements} \end{aligned}$$

Evaluating Eq. (3.23) at every sample time and rewriting in a linear estimation format gives:

$$\begin{bmatrix} \Delta u_x(t_0) \\ \vdots \\ \Delta u_x(t_f) \end{bmatrix} = \begin{bmatrix} t_0 & \int_{t_0}^{t_0} a_{y,ef}\,\mathrm{d}t^* & 1 \\ \vdots & \vdots & \vdots \\ t_f & \int_{t_0}^{t_f} a_{y,ef}\,\mathrm{d}t^* & 1 \end{bmatrix} \begin{bmatrix} a_{x,bias} \\ c_{x,y} \\ \Delta u_{x,0} \end{bmatrix} + noise \tag{3.24}$$

which is equivalently,

$$z_x = H\hat{x_x} + noise \tag{3.25}$$

where

$$z_x = \begin{bmatrix} \Delta u_x(t_0) \\ \vdots \\ \Delta u_x(t_f) \end{bmatrix}, \quad H = \begin{bmatrix} t_0 & \int_{t_0}^{t_0} a_{y,ef}\,\mathrm{d}t^* & 1 \\ \vdots & \vdots & \vdots \\ t_f & \int_{t_0}^{t_f} a_{y,ef}\,\mathrm{d}t^* & 1 \end{bmatrix}, \quad \hat{x_x} = \begin{bmatrix} a_{x,bias} \\ c_{x,y} \\ \Delta u_{x,0} \end{bmatrix}$$

Assuming that noise is zero-mean and uncorrelated, a least squares estimator can then be applied to estimate the a_x bias, cross-coupling coefficient, and initial velocity.

$$\hat{x_x} = \left(H^T H\right)^{-1} H^T z_x \tag{3.26}$$

In practice, these assumptions will not strictly hold. However, this simple approach works very well in obtaining reasonable estimates. The estimation is presented as a batch process here since the cross-coupling is essentially static and continuous updating is not required.

Similarly, Eq. (3.22) can be integrated and rearranged to estimate the lateral accelerometer sensitivity, s_{ay} by defining a term, $\Delta u_x(t)$.

$$\Delta u_y(t) = u_{y,acc}(t)$$

$$
\begin{aligned}
&= a_{y,bias}t + s_{ay}\left(u_{y,sensor}(t) + \int_0^t \left(\dot{\psi}u_{x,sensor} + g\sin\phi\right)\,\mathrm{d}t^*\right) \\
&\quad +\Delta u_{y,0} + noise \\
&= a_{y,bias}t + s_{ay}\int_0^t a_{y,ef}\,\mathrm{d}t^* + \Delta u_{y,0} + noise
\end{aligned} \tag{3.27}
$$

where

$$
\begin{aligned}
u_{y,acc}(t) &= \int_0^t a_{y,m}\,\mathrm{d}t^* \\
&= \text{lateral velocity from integrating } a_y \text{ measurements}
\end{aligned}
$$

Evaluating Eq. (3.27) at every sample time:

$$
\begin{bmatrix} \Delta u_y(t_0) \\ \vdots \\ \Delta u_y(t_f) \end{bmatrix} = \begin{bmatrix} t_0 & \int_{t_0}^{t_0} a_{y,ef}\,\mathrm{d}t^* & 1 \\ \vdots & \vdots & \vdots \\ t_f & \int_{t_0}^{t_f} a_{y,ef}\,\mathrm{d}t^* & 1 \end{bmatrix} \begin{bmatrix} a_{y,bias} \\ s_{ay} \\ \Delta u_{y,0} \end{bmatrix} + noise \tag{3.28}
$$

which is equivalently,

$$
z_y = H\hat{x_y} + noise \tag{3.29}
$$

where

$$
z_y = \begin{bmatrix} \Delta u_y(t_0) \\ \vdots \\ \Delta u_y(t_f) \end{bmatrix}, \quad H = \begin{bmatrix} t_0 & \int_{t_0}^{t_0} a_{y,ef}\,\mathrm{d}t^* & 1 \\ \vdots & \vdots & \vdots \\ t_f & \int_{t_0}^{t_f} a_{y,ef}\,\mathrm{d}t^* & 1 \end{bmatrix}, \quad \hat{x_x} = \begin{bmatrix} a_{y,bias} \\ s_{ay} \\ \Delta u_{y,0} \end{bmatrix}
$$

As before, a least square estimator is applied to estimate the a_y bias, sensitivity, and initial velocity:

$$
\hat{x_y} = \left(H^T H\right)^{-1} H^T z_y \tag{3.30}
$$

While the sensitivity may change with time, this variation was not found to be particularly large so continuous updating is unnecessary. The estimated cross-coupling coefficient, $c_{x,y}$, and lateral accelerometer sensitivity, s_{ay}, are shown in the Fig. 3.16.

Taking into account compensation for roll, grade, the cross-coupling coefficient, $c_{x,y}$, and lateral accelerometer sensitivity, s_{ay}, the model for the velocity Kalman

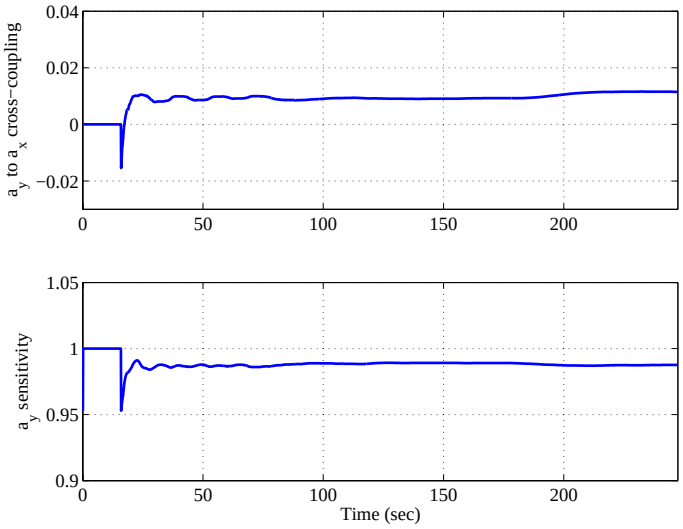

Figure 3.16: Estimated Cross-coupling Coefficient and Lateral Accelerometer Sensitivity

filter in Eq. (3.11) is replaced by the following linear dynamic system constructed from Eqs. (3.21) and (3.22):

$$\begin{bmatrix} \dot{u}_{x,sensor} \\ \dot{a}_{x,bias} \\ \dot{u}_{y,sensor} \\ \dot{a}_{y,bias} \end{bmatrix} = \begin{bmatrix} 0 & -1 & r & c_{x,y}/s_{ay} \\ 0 & 0 & 0 & 0 \\ -r & 0 & 0 & -1/s_{ay} \\ 0 & 0 & 0 & 0 \end{bmatrix} \begin{bmatrix} u_{x,sensor} \\ a_{x,bias} \\ u_{y,sensor} \\ a_{y,bias} \end{bmatrix} + \begin{bmatrix} 1 & c_{x,y}/s_{ay} & g & 0 \\ 0 & 0 & 0 & 0 \\ 0 & 1/s_{ay} & 0 & g \\ 0 & 0 & 0 & 0 \end{bmatrix} \begin{bmatrix} a_{x,m} \\ a_{y,m} \\ \sin\theta_r \\ \sin\phi \end{bmatrix} + \begin{bmatrix} w_{ax,m} \\ w_{ax,bias} \\ w_{ay,m} \\ w_{ay,bias} \end{bmatrix} \tag{3.31}$$

where

$$w_{ax,bias},\ w_{ay,bias} = \text{process noise}$$

Figure 3.17 shows the estimated accelerometer biases after the cross-coupling between the two accelerometers and lateral accelerometer sensitivity are taken into account.

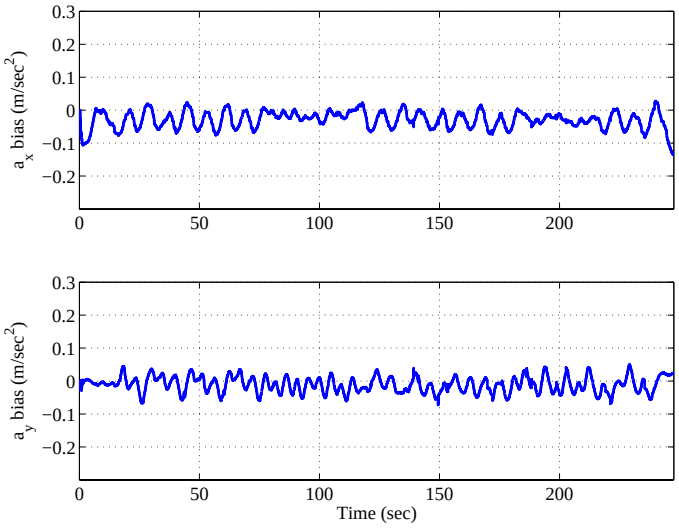

Figure 3.17: Estimated Accelerometer Biases after the Compensation

Note that the variations are reduced after the compensation. Since the lateral acceleration tends to dominate over longitudinal acceleration, only cross-coupling from the lateral acceleration to the longitudinal accelerometer and the lateral accelerometer sensitivity are considered. Estimation of other sensitivity or cross-coupling parameters could be included in an analogous manner but, since the signals are somewhat lower, more convergence time is necessary and the resulting improvement is less. Obviously, there are some remaining bias variations, but the absolute level of variation is quite small given the relatively simple vehicle model used for estimation purposes.

In fact, a large portion of the remaining bias in longitudinal acceleration can be traced to a single modeling assumption. Rapid grade fluctuations at certain spatial frequencies are not detectable through the velocity based grade estimate. As the vehicle moves along the road, the rear wheels see almost the same input as the front wheels, delayed in time by the interval equal to the wheelbase divided by speed. This time delay acts to filter the bounce and pitch motion of the vehicle, and has been

called wheelbase filtering [23]. The typical effects of wheelbase filtering are illustrated in Fig. 3.18.

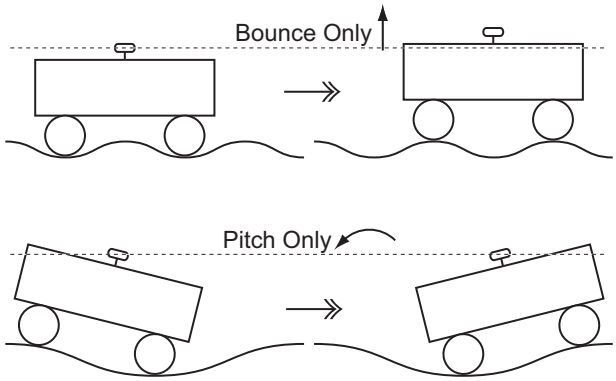

Figure 3.18: Wheelbase Filtering Mechanism

When the wavelength of the road is equal to the wheelbase of the vehicle, or integer multiples equal to the wheelbase, the vehicle only bounces up and down without a pitch change. Similarly, only pitch motion occurs when the wavelength is equal to twice the wheelbase or odd integer multiples equal to twice the wheelbase length. In either case, at these frequencies, the velocity based grade estimate does not reflect the true grade seen by the vehicle. While this effect is small for most roads, the parking lot structure used for testing has a pronounced periodic texture (comparable to the lower half of Fig. 3.18) to provide for drainage. Thus the unmodeled dynamics reflected in the bias variation in Fig. 3.17 have an easily understood physical interpretation in light of the assumptions made in grade measurement. The fact that such seemingly small effects appear provides some additional measure of confidence that the estimator is correctly capturing the larger vehicle motion.

Chapter 4

State Estimation Performance and Application

The previous chapter shows experimentally that the proposed estimation method gives vehicle state estimates at a level previously unavailable. However, the estimation process involves cascaded Kalman filters and overall convergence is not immediately clear from a theoretical standpoint. This chapter proves that the proposed estimation method is stable and gives accurate state estimates for vehicle control purposes. First, the convergence of the cascade filter structure is proven, and the performance of the estimation method is then verified by statistical analysis. Finally, the estimated vehicle states are used to modify a vehicle's handling characteristics through a full state feedback controller. This application shows the applicability of the proposed estimation scheme. This handling modification work is performed jointly with Yih [54]

4.1 Stability of Cascade Estimators

As shown in Fig. 4.1, the vehicle state estimator presented in the previous chapter forms a structure of cascade estimators. The velocity filter uses estimates from the roll and yaw filters in a cascade manner to estimate longitudinal and lateral velocities. However, the overall convergence of such cascade estimators is not shown in the

previous chapter. The convergence of generalized cascade estimators is investigated

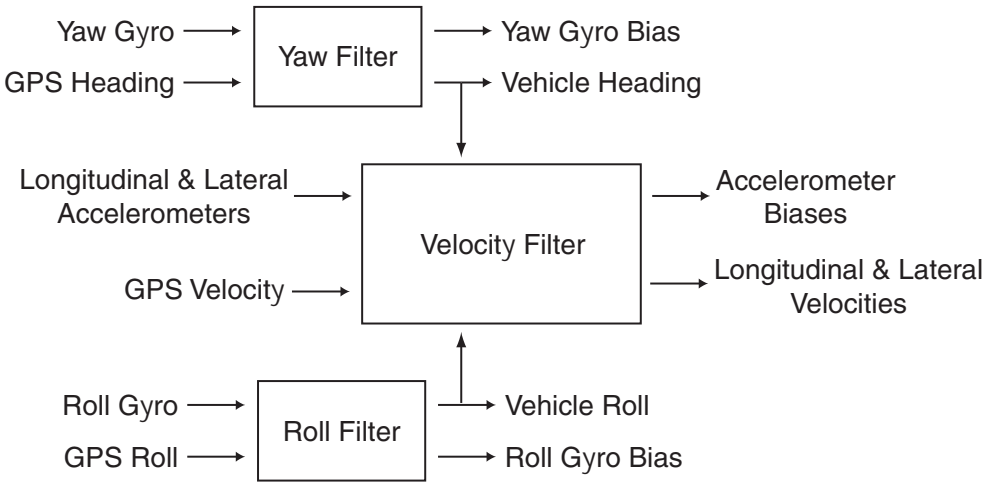

Figure 4.1: Cascade Estimators for Vehicle State Estimation

here in order to show that the proposed estimator structure is stable.

Figure 4.2 shows a generalized structure of the system structure to which the cascade estimator approach can be applied. If two estimators are constructed as shown

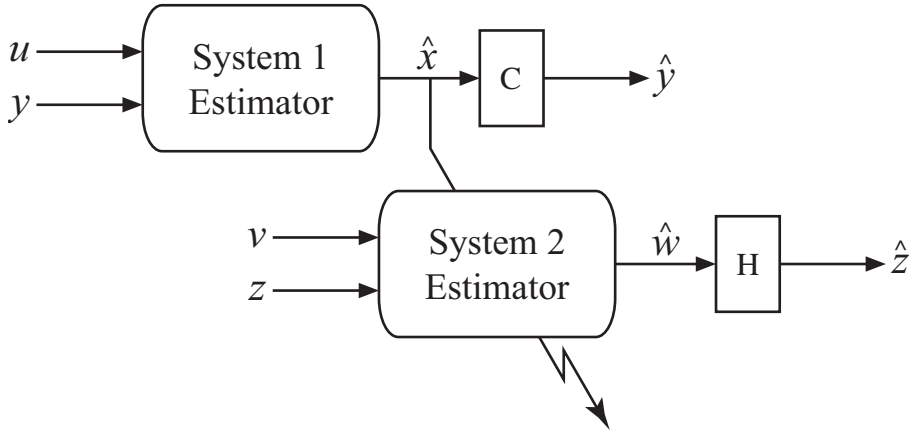

Figure 4.2: Generalized Cascade Estimators

in Fig. 4.2, estimates from the first estimator affect the system dynamics the second estimator. When each estimator is designed according to conventional estimator design techniques, such as a Kalman filter or linear observer, the convergence of the total system is studied here.

The first estimator is designed to estimate states of system 1, which is described by

$$\dot{x} = Ax + Bu \tag{4.1}$$
$$y = Cx \tag{4.2}$$

A linear estimator for system 1 is constructed as

$$\dot{\hat{x}} = A\hat{x} + Bu + L\left(y - C\hat{x}\right) \tag{4.3}$$

where $\hat{x}$ is a estimate of x and L is the estimator gain. If the gain, L, is chosen according to linear estimator design techniques, then the estimate error goes to zero:

$$\dot{e_1} = \left(A - LC\right)e_1$$
$$e_1 \to 0 \quad \text{as} \quad t \to \infty \tag{4.4}$$

where $e_1 = x - \hat{x}$.

The second estimator is constructed for system 2, which is described by

$$\dot{w} = Fw + Gv \tag{4.5}$$
$$z = Hw \tag{4.6}$$

where $F = F(x)$. An estimator for system 2 can be designed according to the estimator design theory similarly to the case of system 1. However, the F matrix estimate, $\hat{F}$, is available only instead of the true F matrix when the F matrix is calculated using estimates, $\hat{x}$, from the estimator of system 1. As a result, the estimator for system 2 is constructed using $\hat{F}$ as

$$\dot{\hat{w}} = \hat{F}\hat{w} + Gv + K\left(z - H\hat{w}\right) \tag{4.7}$$

where $\hat{F} = F(\hat{x})$ and K is chosen using the estimator design theory, so that the

following dynamics go to zero.

$$\dot{e} = \left(\hat{F} - KH\right) e$$
$$e \to 0 \quad \text{as} \quad t \to \infty \tag{4.8}$$

Two assumptions are made here, First, $\hat{F}$ can be divided into the true value, F and the error due to e_1, ΔF, where $\|\Delta F\|$ is known to converge to zero as e_1 goes to zero. Second, w is assumed to be bounded.

$$\hat{F} = F + \Delta F \tag{4.9}$$
$$\|\Delta F\| \to 0 \quad \text{as} \quad e_1 \to \infty \tag{4.10}$$
$$\|w\| \leq w_{max} \tag{4.11}$$

Then, the estimate error of Eq. (4.7) can be calculated by subtracting Eq. (4.7) from Eq. (4.5) and substituting Eq. (4.6).

$$\begin{aligned} \dot{w} - \dot{\hat{w}} &= Fw - \hat{F}\hat{w} - KH\left(w - \hat{w}\right) \\ &= \left(\hat{F} - KH\right)\left(w - \hat{w}\right) - \Delta F w \\ \dot{e_2} &= \left(\hat{F} - KH\right) e_2 - \Delta F w \end{aligned} \tag{4.12}$$

where $e_2 = w - \hat{w}$.

Using the triangle inequality and Eq. (4.11),

$$\|\Delta F w\| \leq \|\Delta F\| \, \|w\| \leq \|\Delta F\| \, w_{max} \tag{4.13}$$

Using Eqs. (4.10) and (4.13),

$$\|\Delta F w\| \to 0 \quad \text{as} \quad e_1 \to \infty \tag{4.14}$$

Therefore,

$$\Delta F w \to 0 \quad \text{as} \quad e_1 \to \infty \tag{4.15}$$

From Eqs. (4.4) and (4.15), Eq. (4.12) converges to the following equation as time goes to infinity.

$$\dot{e_2} = \left(\hat{F} - KH\right) e_2 \tag{4.16}$$

Since K is chosen so that the above error dynamics are stable as shown in Eq. (4.8),

$$e_2 \to 0 \quad \text{as} \quad t \to \infty \tag{4.17}$$

In the vehicle state estimation case, system 2 is equivalent to the velocity filter and F is then from Eq. (3.11):

$$F = \begin{bmatrix} 0 & -1 & r & 0 \\ 0 & 0 & 0 & 0 \\ -r & 0 & 0 & -1 \\ 0 & 0 & 0 & 0 \end{bmatrix} \tag{4.18}$$

$\hat{F}$ is given from the yaw filter as

$$\hat{F} = \begin{bmatrix} 0 & -1 & r_m - \hat{r}_{bias} & 0 \\ 0 & 0 & 0 & 0 \\ -r_m + \hat{r}_{bias} & 0 & 0 & -1 \\ 0 & 0 & 0 & 0 \end{bmatrix} \tag{4.19}$$

$$= \begin{bmatrix} 0 & -1 & r + e_r & 0 \\ 0 & 0 & 0 & 0 \\ -r - e_r & 0 & 0 & -1 \\ 0 & 0 & 0 & 0 \end{bmatrix} \tag{4.20}$$

$$= \begin{bmatrix} 0 & -1 & r & 0 \\ 0 & 0 & 0 & 0 \\ -r & 0 & 0 & -1 \\ 0 & 0 & 0 & 0 \end{bmatrix} + \begin{bmatrix} 0 & 0 & e_r & 0 \\ 0 & 0 & 0 & 0 \\ -e_r & 0 & 0 & 0 \\ 0 & 0 & 0 & 0 \end{bmatrix} \tag{4.21}$$

$$= F + \Delta F \tag{4.22}$$

where $e_r \to 0$ and $\|\Delta F\| \to 0$ as $t \to \infty$.

Therefore, Eqs. (4.9) and (4.10) hold and the estimate error goes to zero according to Eq. (4.17) assuming the vehicle velocity is bounded.

4.2 Statistical Analysis of State Estimation

In the previous chapter, the vehicle state estimates are compared to predictions from a calibrated model instead of actual truth values. This is a result of the difficulty involved with obtaining truth measurements for speed over ground. Optical systems do exist but are far more expensive than the even the research version of the system presented here and suffer from some inaccuracies of their own. It is possible, however, to offer additional support for the filter performance by comparing the innovation statistics to the predictions obtained by propagating the sensor and process noise covariances through the Kalman filters. As this section shows, simple prediction from a linear Kalman filter analysis describes the experimental behavior quite accurately.

The unique structure of the Kalman filters used in this work makes it possible to develop a statistical analysis easily given only the specifications of the INS sensors and GPS receivers. This follows from the fact that all the system models for the Kalman filters are purely based on the kinematic relationships between the INS sensor measurements and the vehicle states as shown in Eqs. (3.20) and (3.31). This means that the system model noise (process noise) is mainly from the INS sensor noise, assuming that the biases and sensitivities of the INS sensors can be modeled as random walks with relatively small variances. As a result, noise from the INS sensors, such as accelerometers and rate gyros, act as the process noise in the Kalman filters and the noise from the GPS system enters as traditional measurement noise in Eqs. (3.4) and (3.16).

Table 4.1 shows the actual values for the process noise variances of the Kalman filters used in this work. The noise variances of the accelerometers and the rate gyros are taken from the sensor specification and are used as the process noise variances for the corresponding vehicle states. The noise variances for the sensor sensitivities and biases are chosen from the experimental tests to give reasonable convergence rates of

the sensitivity and bias estimates. The numerical values for the measurement noise variances of the Kalman filters are also shown in Table 4.1. The noise covariances of the GPS angle and velocity measurements are taken from the GPS receiver specifications and are used as the measurement noise variances for each Kalman filter.

Process Noise			
State	$1\ \sigma$	State	$1\ \sigma$
$w_{r,m}$	0.2 (deg/s)	$w_{ax,m}$	0.05 (m/s^2)
w_{sr}	1.0e-3	$w_{ay,m}$	0.05 (m/s^2)
$w_{r,bias}$	1.0e-2 (deg/s)	$w_{ax,bias},\ w_{ay,bias}$	1.0e-3 (m/s^2)
Measurement Noise			
Measurement		$1\ \sigma$	
ψ_m^{GPS}		0.2 (deg)	
$u_{x,m}^{GPS}$		0.03 (m/s)	
$u_{y,m}^{GPS}$		0.03 (m/s)	

Table 4.1: Measurement and Process Noise Covariances

With these noise variances, the estimate error covariances can be calculated from the Kalman filters under the assumption that all calibration is correct and all compensation is performed exactly. These covariances describe the differences between the filter output and ground truth, however, and are not directly comparable to the measurement residual (or innovation) obtained by comparing the filter output to the measurement at each time step. For a proper comparison, the expected variances of the measurement residuals may be calculated as the sum of the error covariances from the Kalman filters and the variances of the measurement noise as shown in Eq. (4.23), assuming that the process noise and measurement noise are uncorrelated.

$$S = CPC^T + R \tag{4.23}$$

where

$S =$ measurement residual covariance

$C =$ observation matrix

P = error covariance matrix

R = measurement noise covariance matrix

Yaw Filter	Measurement Residuals				Expected Variances	
	Mean	-4.1e-3	1 σ	0.2572	1 σ	0.2544
Velocity Filter	Measurement Residuals				Expected Variances	
	Mean	-1.3e-4	1 σ	0.04037	1 σ	0.03852
Percentages within σ Bounds						
Yaw Filter	$\leq 1\ \sigma$	71.57%	$\leq 2\ \sigma$	94.90%	$\leq 3\ \sigma$	98.83%
Velocity Filter	$\leq 1\ \sigma$	69.88%	$\leq 2\ \sigma$	95.54%	$\leq 3\ \sigma$	99.08%
Gaussian (Normal)	$\leq 1\ \sigma$	68.27%	$\leq 2\ \sigma$	95.45%	$\leq 3\ \sigma$	99.73%

Table 4.2: Statistics of Measurement Residuals and Estimated Variances

The statistics of the actual measurement residuals from the experimental tests are shown in Table 4.2 together with the expected variances of the measurement residuals. It can be seen that the variances of measurement residuals are similar to the Kalman filter predictions. This suggests that the calibration and compensation methods function as desired. In reality, the sensor performance is slightly better than that guaranteed by the manufacturer but in these experiments this conservatism neatly balances degradation due to unmodeled effects such as wheelbase filtering. Table 4.2 also demonstrates that the mean values of the measurement residuals are virtually zero. This implies that the techniques for the sensor bias removal work and no serious biases exist during the estimation processes. The distributions of the measurement residuals are also compared with the Gaussian (normal) distribution in the last three columns of Table 4.2. The comparison shows that the measurement residuals follow the normal distribution roughly. This indicates that the basic assumption of this analysis (zero-mean Gaussian noise) is reasonable and that the Kalman filter error prediction is in fact meaningful.

Figure 4.3 shows the plot of measurement residuals for each Kalman filter and the bounding 3σ regions of confidence derived from the filter. Note that measurement residuals are centered at zero and most of them are within the bounding 3σ regions. The outliers, in fact, correspond to points where new GPS data was not available

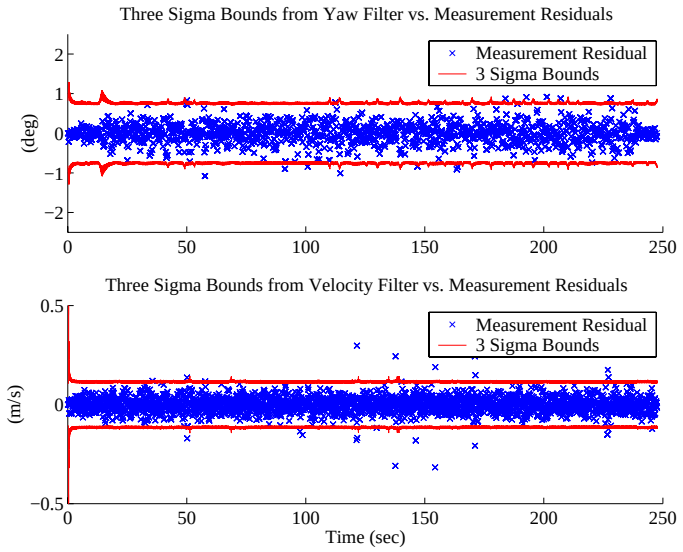

Figure 4.3: Measurement Residual vs. Estimated 3 σ Bounds

for a given time step, an effect that could be explicitly included in calculating the expected variances but was not considered here.

4.3 Handling Modification

4.3.1 Introduction

As a step toward fully integrated vehicle dynamic control systems, active steering capability is available on select production vehicles and will be popular in the near future [8, 54]. One of the potential benefits of active steering capability is to improve handling behavior by active steering control [2, 29]. Although feedback of sideslip angle for active steering control has been proposed theoretically [37], the difficulty in estimating vehicle sideslip presents an obstacle to accomplishing this in practice. However, estimated sideslip from the proposed method may be used for active steering control since the proposed state estimation method provides accurate estimates of vehicle sideslip. This section demonstrates that the estimates from the proposed method are accurate and clean enough to be used by a real-world vehicle controller.

A test vehicle converted to steer-by-wire is used to show that a vehicle's handling characteristics can be modified using a full state feed back controller with state estimates from the proposed GPS/INS method. This handling modification is really beneficial to the drivers since it can take care of driver preferences, changes in weight distribution, and tire wear.

4.3.2 Full State Feedback Controller

A full state feedback control law for an active steering vehicle is given by:

$$\delta = K_r r + K_\beta \beta + K_d \delta_d \tag{4.24}$$

where δ_d is the driver commanded steer angle and δ is the augmented angle (the total steer angle at the road wheels). In order to modify a vehicle's handling characteristics, a target front cornering stiffness is first defined as:

$$\hat{C}_{\alpha f} = C_{\alpha f}(1 + \eta) \tag{4.25}$$

where η is the desired fractional change in the original front cornering stiffness C_f. Then, the state feedback gains are set in terms of η as follows:

$$K_\beta = -\eta, \quad K_r = -\frac{a}{V}\eta, \quad K_d = -(1+\eta)\eta \tag{4.26}$$

Using the feedback law by Eq. (4.24) with Eq. (2.5), a new state space equation with the new cornering stiffness $\hat{C}_{\alpha f}$ is given in the same form as Eq. (2.5):

$$\begin{bmatrix} \dot{u}_{y,CG} \\ \dot{r} \end{bmatrix} = \begin{bmatrix} \frac{-\hat{C}_{\alpha f} - C_{\alpha r}}{m u_{x,CG}} & -u_{x,CG} + \frac{C_{\alpha r} b - \hat{C}_{\alpha f} a}{m u_{x,CG}} \\ \frac{C_{\alpha r} b - \hat{C}_{\alpha f} a}{I_z u_{x,CG}} & \frac{-\hat{C}_{\alpha f} a^2 - C_{\alpha r} b^2}{I_z u_{x,CG}} \end{bmatrix} \begin{bmatrix} u_{y,CG} \\ r \end{bmatrix} + \begin{bmatrix} \frac{\hat{C}_{\alpha f}}{m} \\ \frac{\hat{C}_{\alpha f} a}{I_z} \end{bmatrix} \delta \tag{4.27}$$

Since tire cornering stiffness affects a vehicle's handling characteristics directly, the effect of changing front tire cornering stiffness is to make the vehicle either more oversteering or understeering depending on the sign of η. There are obviously many other ways to apply full state feedback control, but the physical motivation behind

cornering stiffness adjustment makes clear through the bicycle model exactly how the handling characteristics have been modified. Note that in this formulation, it is not necessary to know the real cornering stiffness of the front tire – only vehicle speed and weight distribution, which are relatively easy to measure, are necessary – to achieve the desired handling modification.

4.3.3 Experimental Results

A production model 1997 Chevrolet Corvette is modified for full steer-by-wire capability by replacing the steering shaft with a brushless DC servomotor actuator [54]. The steer-by-wire test vehicle is also equipped with a two-antenna GPS receiver and INS sensors configured to estimate its states as shown in Fig. 4.4. The experimental setup for vehicle state estimation is the same as described in the previous chapter and the same estimation method is used.

Figure 4.4: Experimental Steer-by-wire Vehicle

Experimental tests of the handling modification are performed at Moffett airfield,

California. First, the test vehicle is driven without handling modification. Figure 4.5 shows that the measured yaw rate from a sinusoidal steering input while driving at 13.4 m/s (30 $mile/hr$) compares well to simulation results from the bicycle model. After that, handling modification is implemented on the test vehicle. Changes in

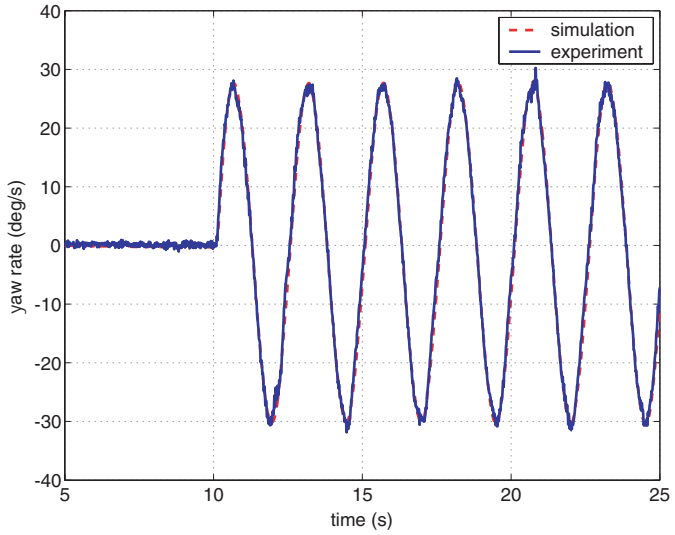

Figure 4.5: Comparison between Bicycle Model and Experiment with Normal Cornering Stiffness

handling characteristics with the proposed full state feedback control scheme are evaluated by comparing measured vehicle response to the nominal case shown in Fig. 4.5.

In Fig. 4.6, the effective front tire cornering stiffness is reduced 50% by setting η to -0.5. The experimental results exhibit lower peak yaw rate and sideslip values than the nominal case. This behavior is expected since reducing the front tire cornering stiffness makes the vehicle tend toward understeer. Figure 4.7 confirms that the experimental results for the reduced case match bicycle model simulation. Experimental results show a corresponding but opposite change in handling behavior when the effective front tire cornering stiffness is increased such that the vehicle tends toward oversteer.

For the final series of tests, 182 kg (400 lbs) of weight are added to the rear of

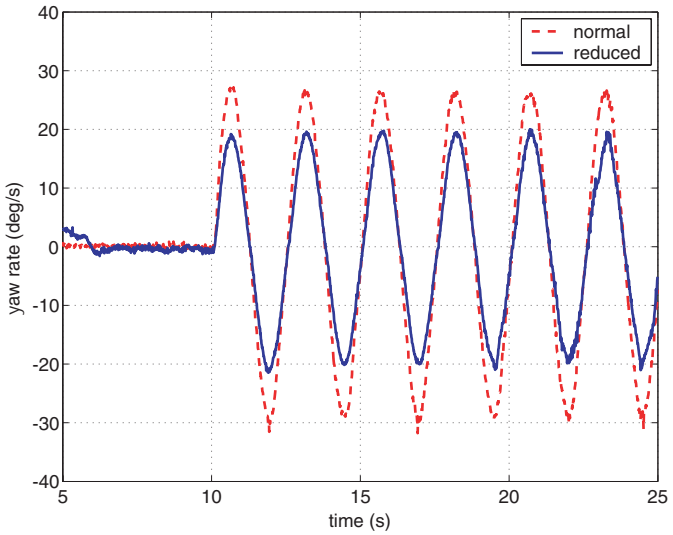

Figure 4.6: Comparison between Normal and Effectively Reduced Front Cornering Stiffness

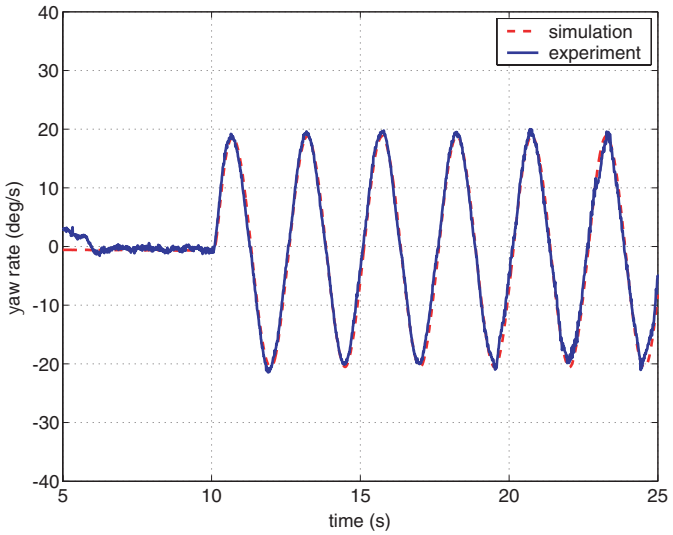

Figure 4.7: Comparison between Bicycle Model and Experiment with Reduced Cornering Stiffness

the vehicle so that 43% of the total vehicle weight lies over the front axle with 57% over the rear axle. The unloaded vehicle originally has a weight distribution balanced equally front to rear. The loaded vehicle exhibits slightly more oversteering behavior than the unloaded vehicle as seen in Fig. 4.8. However, a 20% reduction in front tire cornering stiffness with active handling modification returns the controlled vehicle to the near neutral handling behavior of the unloaded vehicle as shown in Fig. 4.9. While the difference in handling behavior may seem small when viewed on a graph, the improvement with handling modification is readily apparent to both driver and passenger.

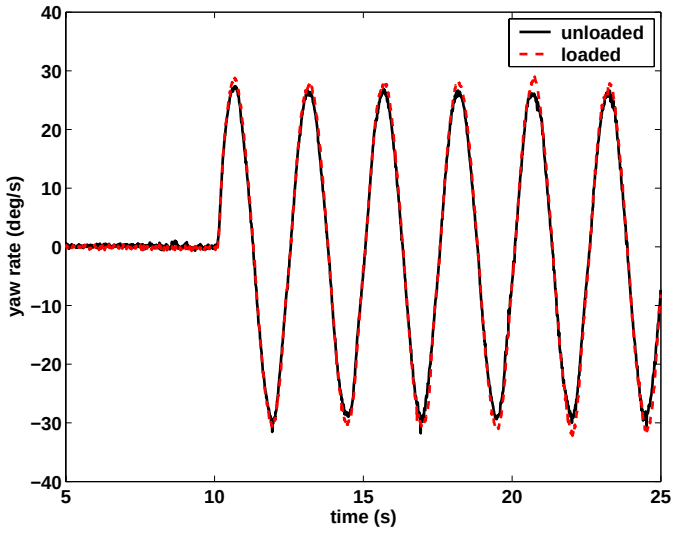

Figure 4.8: Comparison between Unloaded and Loaded Vehicle

This work represents one of the first applications of GPS-based state estimation to dynamic control of a vehicle with active steering. Experimental results demonstrate that the estimated vehicle states can be used to alter a vehicle's handling characteristics with a full state feedback controller.

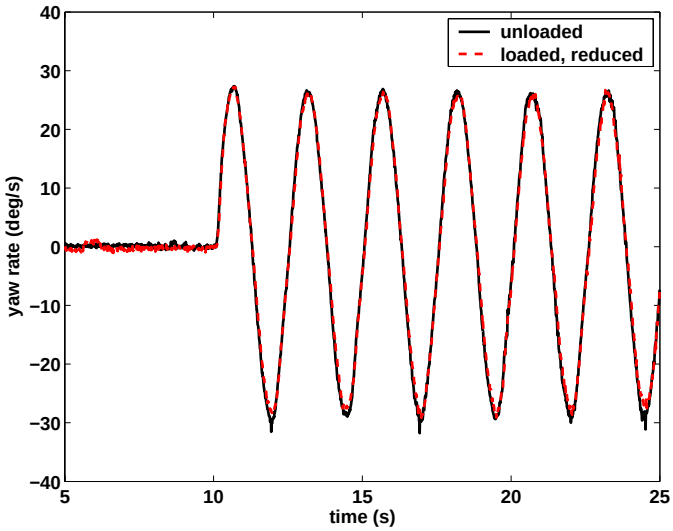

Figure 4.9: Comparison between Unloaded Vehicle and Loaded Vehicle with Handling Modification

Chapter 5

Vehicle Parameter Estimation

5.1 Introduction

The design of vehicle control systems requires sufficiently accurate system models in order to achieve a desired level of closed-loop performance. Parameters of the models are one of the important factors that determine the accuracy of system modeling and eventually overall performance of closed-loop system. Using accurate estimates of vehicle states at a level previously unavailable, key vehicle parameters – such as tire cornering stiffness, understeer gradient, yaw moment of inertia, roll stiffness, and roll damping coefficient – can be estimated easily. This chapter investigates various vehicle parameter estimation schemes and demonstrates experimental results of the estimation schemes. First, parameters of the bicycle model – such as tire cornering stiffness, weight distribution, and yaw moment of inertia – are estimated using the least squares method and total least squares method. Then, vehicle roll parameters – such as roll stiffness and roll damping ratio – are estimated using the least squares method. Once vehicle parameters are precisely estimated, then parameterized vehicle dynamics models with properly estimated parameters can be used for a wide variety of applications including highway automation, vehicle stability control, and rollover prevention systems [10, 17, 38, 47, 53].

5.2 Bicycle Model Parameter Estimation

5.2.1 Introduction

The lateral dynamics of a vehicle can be modeled using the bicycle model with several parameters of the vehicle as shown in Fig. 2.3 and Eq. (2.5). The bicycle model is written as:

$$\begin{bmatrix} \dot{u}_{y,CG} \\ \dot{r} \end{bmatrix} = \begin{bmatrix} \frac{-C_{\alpha f}-C_{\alpha r}}{mu_{x,CG}} & -u_{x,CG}+\frac{C_{\alpha r}b-C_{\alpha f}a}{mu_{x,CG}} \\ \frac{C_{\alpha r}b-C_{\alpha f}a}{I_z u_{x,CG}} & \frac{-C_{\alpha f}a^2-C_{\alpha r}b^2}{I_z u_{x,CG}} \end{bmatrix} \begin{bmatrix} u_{y,CG} \\ r \end{bmatrix} + \begin{bmatrix} \frac{C_{\alpha f}}{m} \\ \frac{C_{\alpha f}a}{I_z} \end{bmatrix} \delta \qquad (5.1)$$

The bicycle model includes mass, moment of inertia, cornering stiffness of tires, and weight distribution of the vehicle to explain lateral dynamics of the vehicle. While the mass of a vehicle can be estimated well as shown in previous work [3], identifying cornering stiffness, yaw moment of inertia, and weight distribution of a vehicle still remains a hard problem. In this section, the estimated vehicle states from a kinematic Kalman filter are used to identify the front and rear cornering stiffness of the tires and yaw moment of inertia and weight distribution of the vehicle. Because the vehicle parameters are not used in the estimation of the vehicle states, a separate algorithm can be used to identify the parameters of the vehicle.

5.2.2 Nonlinearity in Steering System

Since a steering wheel is connected to its road wheel through steering linkages, the angle measured at the steering wheel does not always represent the road wheel angle in a linear relationship when the steering system has nonlinearity. The nonlinearity in the steering system should be taken into account in order to accurately estimate cornering stiffness of tires because a small error in slip angle can result in a huge error in estimating cornering stiffness of the tire.

Figure 5.1 shows the nonlinearity in the steering system of the test vehicle. The dotted line represents road wheel angle calculated using a constant steering ratio, and the solid line is the best third-order polynomial fit through measured values of actual road angle. Note that measured actual road wheel angle does not have a linear

relationship with steering wheel angle.

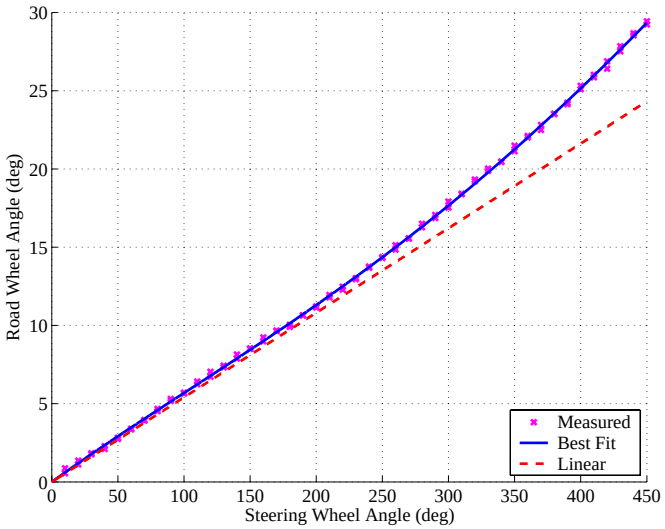

Figure 5.1: Nonlinearity in Steering System

5.2.3 Estimation of Cornering Stiffness Using Least Squares

The front and rear cornering stiffness of the tires, $C_{\alpha f}$ and $C_{\alpha r}$, are estimated first assuming the mass, moment of inertia, and weight distribution are known or estimated. The cornering stiffness can be estimated using the bicycle model and state estimates from the kinematic Kalman filters because the filters do not rely on the physical parameters. In order to estimate the front and rear cornering stiffness of the tires, $C_{\alpha f}$ and $C_{\alpha r}$, the bicycle model, Eq. (5.1), is rewritten in terms of those values as in the following equation.

$$\begin{aligned}\begin{bmatrix} \dot{u}_{y,CG} \\ \dot{r} \end{bmatrix} &= \begin{bmatrix} \frac{-C_{\alpha f}-C_{\alpha r}}{m u_{x,CG}} u_{y,CG} - u_{x,CG} r + \frac{C_{\alpha r} b - C_{\alpha f} a}{m u_{x,CG}} r + \frac{C_{\alpha f}}{m}\delta \\ \frac{C_{\alpha r} b - C_{\alpha f} a}{I_z u_{x,CG}} u_{y,CG} + \frac{-C_{\alpha f} a^2 - C_{\alpha r} b^2}{I_z u_{x,CG}} r + \frac{C_{\alpha f} a}{I_z}\delta \end{bmatrix} \\ &= \begin{bmatrix} f\left(C_{\alpha f}, C_{\alpha r}\right) \\ g\left(C_{\alpha f}, C_{\alpha r}\right) \end{bmatrix} \end{aligned} \tag{5.2}$$

Equation (5.2) can then be expressed in a discrete form using the Euler method as follows:

$$\begin{bmatrix} u_{y,CG}(k+1) \\ r(k+1) \end{bmatrix} = \begin{bmatrix} u_{y,CG}(k) + f\left(C_{\alpha f}, C_{\alpha r}\right)\Delta T \\ r(k) + g\left(C_{\alpha f}, C_{\alpha r}\right)\Delta T \end{bmatrix} \tag{5.3}$$

where ΔT represents the sampling time.

Since the states, $u_{y,CG}$ and r, are available from the kinematic Kalman filters, the least square method can be applied to estimate the cornering stiffness, $C_{\alpha f}$ and $C_{\alpha r}$. To apply the least square method, Eq. (5.3) can be rewritten as:

$$y = h(\theta) \tag{5.4}$$

where

$$\begin{aligned} y &= \begin{bmatrix} u_{y,CG}(k+1) & r(k+1) \end{bmatrix}^T \\ \theta &= \begin{bmatrix} C_{\alpha f} & C_{\alpha r} \end{bmatrix}^T \end{aligned}$$

Because y is measured, there exists measurement error, Δy, and the estimation problem can then be reformulated as follows:

$$\begin{aligned} \min_{\theta} \quad & \left\| \Delta y \right\| \\ \text{Subject to:} \quad & \hat{y} = h(\theta) + \Delta y \end{aligned} \tag{5.5}$$

where

$$\begin{aligned} \hat{y} &= y + \Delta y \\ \Delta y &= \text{measurement error} \end{aligned}$$

This minimization problem can be then solved by the conventional least squares method since it forms a linear structure in terms of $C_{\alpha f}$ and $C_{\alpha r}$ as shown in Eq. (5.4).

5.2.4 Estimation Results by Least Squares Method

Table 5.1 shows results of cornering stiffness estimation from experimental tests with normal maneuvering. A typical test run is shown in Fig. 5.2. The reference values of

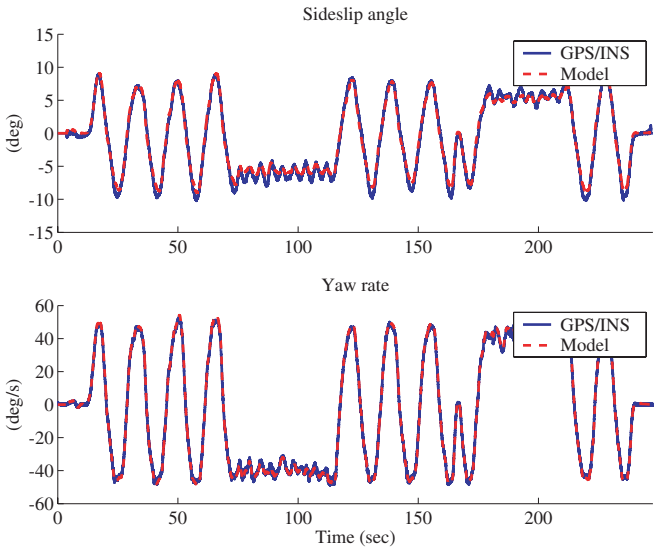

Figure 5.2: Sideslip Angle and Yaw Rate of Experimental Test

the cornering stiffness, which are used for the bicycle model, are 100,000 N/rad for the front tire and 160,000 N/rad for the rear tire.

	$C_{\alpha f}$ (N/rad)	$C_{\alpha r}$ (N/rad)	$C_{\alpha f}$ (N/rad)	$C_{\alpha r}$ (N/rad)
Experimental Results	115,014	165,240	111,673	164,780
	130,078	191,390	100,198	192,090
	104,282	168,170	131,885	183,420
	111,414	160,800	103,587	189,190
	102,151	185,900	101,963	193,160

	$C_{\alpha f}$ (N/rad)	$C_{\alpha r}$ (N/rad)
Mean of Experimental Results	111,225	179,414
1 σ of Experimental Results	11,514	13,058
Reference Value	100,000	160,000

Table 5.1: Estimation results of Cornering Stiffness

Even though the simple linear least squares method is used, the cornering stiffness

estimation yields a reasonable value for the bicycle model. In addition, the estimation process can be easily applied to a real-time system in a recursive way since the linear least squares method can be converted to a recursive method. The recursive method takes care of only new data at every time step, not all of the past data. This saves a lot of computational power and makes real-time implementation of the method relatively easy. However, the estimation results shows some errors compared to the reference value, and the variance is not insignificant. In order to resolve these problems and make the estimator more robust and consistent, the structure of the estimation problem should be examined more carefully.

5.2.5 Estimation Using Total Least Squares

When the least squares method is applied to Eq. (5.4), a basic assumption is that measurement errors exist only with y as shown in Eq. (5.5). However, measurement errors exist in both sides of the equation since the right side of the equation is also a function of measurements, $u_{y,CG}$ and r. This is similar to orthogonal regression and errors in the variables (EIV) problems, and the total least squares method can be used to get more robust and consistent estimates [28].

In order to apply the total least squares for cornering stiffness estimation, the bicycle model, Eq. (5.1), is rewritten in terms of measurements and unknown parameters as in the following equation.

$$\begin{aligned}\begin{bmatrix} \dot{u}_{y,CG} \\ \dot{r} \end{bmatrix} &= \begin{bmatrix} \frac{-C_{\alpha f}-C_{\alpha r}}{mu_{x,CG}}u_{y,CG} - u_{x,CG}r + \frac{C_{\alpha r}b-C_{\alpha f}a}{mu_{x,CG}}r + \frac{C_{\alpha f}}{m}\delta \\ \frac{C_{\alpha r}b-C_{\alpha f}a}{I_z u_{x,CG}}u_{y,CG} + \frac{-C_{\alpha f}a^2-C_{\alpha r}b^2}{I_z u_{x,CG}}r + \frac{C_{\alpha f}a}{I_z}\delta \end{bmatrix} \\ &= \begin{bmatrix} f\left(u_{y,CG}, r, C_{\alpha f}, C_{\alpha r}\right) \\ g\left(u_{y,CG}, r, C_{\alpha f}, C_{\alpha r}\right) \end{bmatrix} \end{aligned} \tag{5.6}$$

Similarly to Eq. (5.3), Eq. (5.6) can be expressed in a discrete form using the Euler method as follows:

$$\begin{bmatrix} u_{y,CG}(k+1) \\ r(k+1) \end{bmatrix} = \begin{bmatrix} u_{y,CG}(k) + f\left(u_{y,CG}(k), r(k), C_{\alpha f}, C_{\alpha r}\right)\Delta T \\ r(k) + g\left(u_{y,CG}(k), r(k), C_{\alpha f}, C_{\alpha r}\right)\Delta T \end{bmatrix} \tag{5.7}$$

where ΔT represents the sampling time.

To apply the total least squares method, Eq. (5.7) can be rewritten as:

$$y = h(x, \theta) \tag{5.8}$$

where

$$\begin{aligned} y &= [\ u_{y,CG}(k+1) \quad r(k+1)\ ]^T \\ x &= [\ u_{y,CG}(k) \quad r(k)\ ]^T \\ \theta &= [\ C_{\alpha f} \quad C_{\alpha r}\ ]^T \end{aligned}$$

Since x and y are measured, there exist measurement errors, Δx and Δy. The estimation problem can then be reformulated as follows:

$$\begin{aligned} \min_{x,\theta} \quad & \left\| \begin{array}{c} \Delta x \\ \Delta y \end{array} \right\| \\ \text{Subject to:} \quad & \hat{y} - \Delta y = h(\hat{x} - \Delta x, \theta) \end{aligned} \tag{5.9}$$

where

$$\begin{aligned} \hat{x} &= x + \Delta x \\ \hat{y} &= y + \Delta y \\ \Delta x,\ \Delta y &= \text{measurement errors} \end{aligned}$$

This minimization problem can be then solved by iteration. The details of the total least squares method are explained in Appendix A and other references [10].

5.2.6 Estimation Results by Total Least Squares Method

Figure 5.3 shows results of cornering stiffness estimation from an experimental test by the total least squares method. The estimates converge to the given values in less than ten iterations. Table 5.2 also shows results of cornering stiffness estimation by

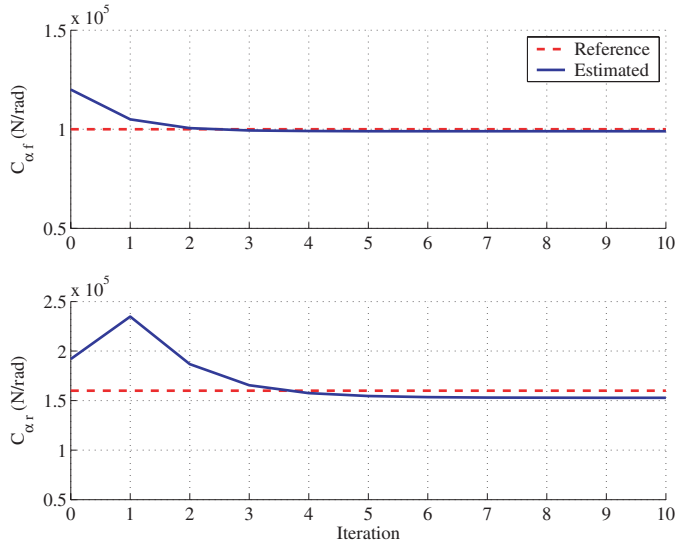

Figure 5.3: Estimation of Front and Rear Tire Cornering Stiffness

the total least squares method from the same experimental tests as used by the least squares method in Table 5.1

	$C_{\alpha f}$ (N/rad)	$C_{\alpha r}$ (N/rad)	$C_{\alpha f}$ (N/rad)	$C_{\alpha r}$ (N/rad)
Experimental Results	99,577	152,528	97,716	165,396
	85,071	138,612	100,500	159,384
	89,550	147,120	101,388	163,612
	96,097	154,764	87,335	148,436
	89,153	158,256	98,990	152,810

	$C_{\alpha f}$ (N/rad)	$C_{\alpha r}$ (N/rad)
Mean of Experimental Results	94,538	154,092
1 σ of Experimental Results	6,106	8,087
Reference Value	100,000	160,000

Table 5.2: Estimation results of Cornering Stiffness

As shown in Table 5.2, the estimates by the total least squares show less error than the estimates from the least squares and also have less variance. Since the noise structure of the estimation problem is taken care of more carefully with the total least squares method, it yields more robust and consistent estimates than the least squares method does as shown in Table 5.1.

5.2.7 Estimation of Cornering Stiffness and Weight Distribution

In the previous section, it is shown that the cornering stiffness can be estimated. A natural question is whether the weight distribution can be simultaneously estimated as well. In this section, the front and rear cornering stiffness of the tires, $C_{\alpha f}$ and $C_{\alpha r}$, and distances from front and rear axles to CG (weight distribution of the vehicle), a and b, are estimated simultaneously using the nonlinear total least squares method. Similarly to Eq. (5.6), the bicycle model is rewritten in terms of measurements and unknown parameters as in the following equation.

$$\begin{aligned}\begin{bmatrix} \dot{u}_{y,CG} \\ \dot{r} \end{bmatrix} &= \begin{bmatrix} \frac{-C_{\alpha f}-C_{\alpha r}}{mu_{x,CG}}u_{y,CG} - u_{x,CG}r + \frac{C_{\alpha r}b-C_{\alpha f}a}{mu_{x,CG}}r + \frac{C_{\alpha f}}{m}\delta \\ \frac{C_{\alpha r}b-C_{\alpha f}a}{I_z u_{x,CG}}u_{y,CG} + \frac{-C_{\alpha f}a^2-C_{\alpha r}b^2}{I_z u_{x,CG}}r + \frac{C_{\alpha f}a}{I_z}\delta \end{bmatrix} \\ &= \begin{bmatrix} f\left(u_{y,CG}, r, C_{\alpha f}, C_{\alpha r}, a\right) \\ g\left(u_{y,CG}, r, C_{\alpha f}, C_{\alpha r}, a\right) \end{bmatrix} \end{aligned} \tag{5.10}$$

where b can be replaced by $L - a$ assuming the wheelbase length, L, is known. Equation (5.10) can then be expressed in a discrete form using the Euler method as follows:

$$\begin{bmatrix} u_{y,CG}(k+1) \\ r(k+1) \end{bmatrix} = \begin{bmatrix} u_{y,CG}(k) + f\left(u_{y,CG}(k), r(k), C_{\alpha f}, C_{\alpha r}, a\right)\Delta T \\ r(k) + g\left(u_{y,CG}(k), r(k), C_{\alpha f}, C_{\alpha r}, a\right)\Delta T \end{bmatrix} \tag{5.11}$$

where ΔT represents the sampling time.

Based on Eq. (5.11), the nonlinear total least squares method can be applied to estimate cornering stiffness, $C_{\alpha f}$ and $C_{\alpha r}$, and distance from front axle to CG, a, in a manner similar to Eq. (5.9). Figure 5.4 shows results of cornering stiffness and distance from front axle to CG estimation from an experimental test with normal maneuvering. The test driving data is shown in Fig. 5.5. Interesting results are obtained when cornering stiffness and weight distribution are estimated simultaneously from tests with typical driving situations. Even though the estimation results converge in

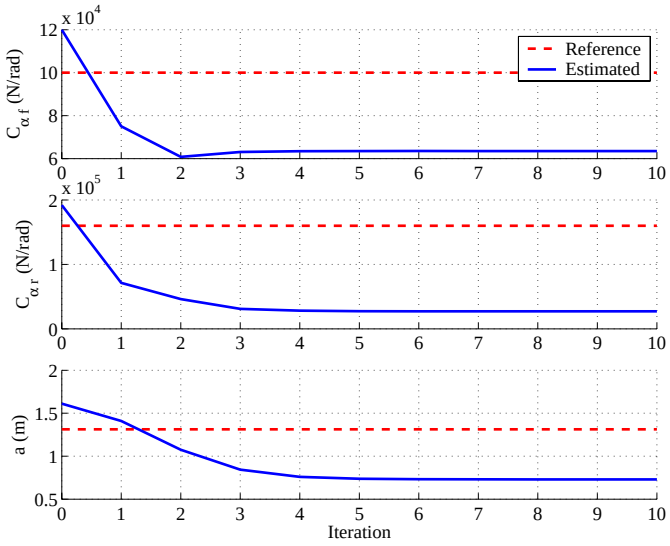

Figure 5.4: Estimation of Tire Cornering Stiffness and Weight Distribution

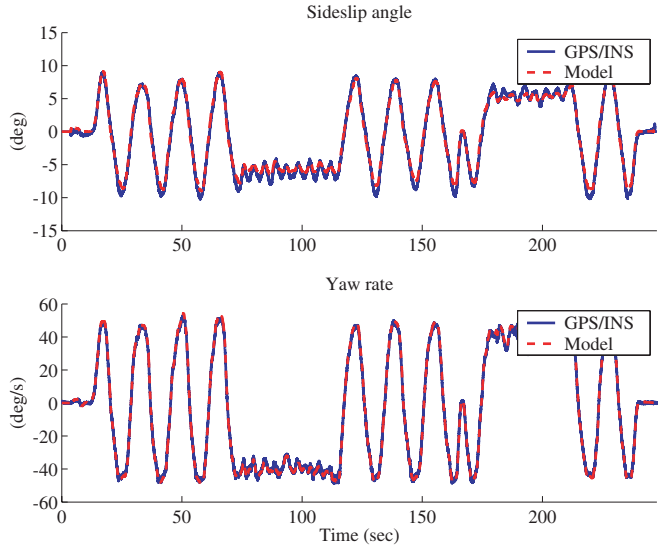

Figure 5.5: Sideslip Angle and Yaw Rate of Experimental Test

less than ten iterations, estimates do not converge to the correct values. The estimates should converge to 100,000 N/rad for front cornering stiffness, 160,000 N/rad for rear cornering stiffness, and 1.313 for the distance from front axle to CG, but apparently it is not the case in Fig. 5.4.

In fact, it turns out that the estimation of cornering stiffness and weight distribution is not always possible even when the vehicle is turning. This can be shown by simulations as well as experimental tests. A series of simulations using the bicycle model is performed with various inputs, and the cornering stiffness and weight distribution are estimated from the simulations. The simulation is performed with the measurement and process noise. Variance of the measurement noise is measured from the experimental tests, and variance of the process noise is guessed reasonably. The estimation results are listed in Table 5.3.

Simulation Input	$C_{\alpha f}$ (N/rad)	$C_{\alpha r}$ (N/rad)	a (m)	Understeer Gradient (deg/g)
0.1 Hz Sinusoid	88,092	66,840	0.9586	2.5463
0.4 Hz Sinusoid	96,200	126,180	1.2352	2.5032
2 Hz Sinusoid	98,800	152,400	1.3110	2.4965
Sinusoidal Sweep 0.1-0.5 Hz	94,930	112,660	1.1887	2.4847
Sinusoidal Sweep 0.1-1 Hz	97,510	135,560	1.2605	2.5063
Sinusoidal Sweep 0.1-2 Hz	98,130	149,290	1.3014	2.5293
Experiment	66,691	28,450	0.7301	2.3750
Reference Value	100,000	160,000	1.3130	2.5670

Table 5.3: Estimation results of Cornering Stiffness and Weight Distribution

As clearly seen in Table 5.3, the cornering stiffness and weight distribution cannot be simultaneously estimated without sufficient excitation, especially without high frequency input components. In other words, the estimated cornering stiffness and weight distribution is not correct when the maneuvering does not excite vehicle lateral dynamics enough. However, it is interesting that the understeer gradient resulting from the estimated cornering stiffness and weight distribution is always correct whether there exists sufficient excitation or not.

This phenomenon can be analytically proven by analysis of the bicycle model. Suppose there is not sufficient excitation or high frequency input components, the

vehicle is then quasi-steady-state, which means resulting $\dot{u}_{y,CG}$ and $\dot{r}$ are small and close to zero. As a result, the following equations are approximately satisfied from the bicycle model, Eq. (5.1).

$$\begin{bmatrix} \frac{-C_{\alpha f}-C_{\alpha r}}{mV} & -V+\frac{C_{\alpha r}b-C_{\alpha f}a}{mV} \\ \frac{C_{\alpha r}b-C_{\alpha f}a}{I_zV} & \frac{-C_{\alpha f}a^2-C_{\alpha r}b^2}{I_zV} \end{bmatrix} \begin{bmatrix} u_{y,CG} \\ r \end{bmatrix} + \begin{bmatrix} \frac{C_{\alpha f}}{m} \\ \frac{C_{\alpha f}a}{I_z} \end{bmatrix} \delta \approx 0 \tag{5.12}$$

where

$$\dot{u}_{y,CG} \approx 0, \quad \text{and} \quad \dot{r} \approx 0$$

Then, rewriting Eq. (5.12) gives:

$$\left(\frac{-C_{\alpha f}-C_{\alpha r}}{mV}\right) u_{y,CG} + \left(-V+\frac{C_{\alpha r}b-C_{\alpha f}a}{mV}\right) r + \left(\frac{C_{\alpha f}}{m}\right)\delta \approx 0 \tag{5.13}$$

$$\left(\frac{C_{\alpha r}b-C_{\alpha f}a}{I_zV}\right) u_{y,CG} + \left(\frac{-C_{\alpha f}a^2-C_{\alpha r}b^2}{I_zV}\right) r + \left(\frac{C_{\alpha f}a}{I_z}\right)\delta \approx 0 \tag{5.14}$$

In order to estimate three unknowns, $C_{\alpha f}$, $C_{\alpha r}$, and a, with the above two equations, multiple linearly independent data points are necessary because the number of equations should be equal to or greater than the number of unknowns. However, $u_{y,CG}$, r, and δ are not linearly independent when the vehicle is quasi-steady-state. This is because the steady-state $u_{y,CG}$ and r are linearly related to the steering angle, δ as shown in Eq. (5.15).

$$\begin{aligned} u_{y,CG,ss} &= \frac{C_{\alpha f}(bLC_{\alpha r}-amV^2)V}{L^2C_{\alpha f}C_{\alpha r}-(C_{\alpha f}+C_{\alpha r}mV^2)}\delta \\ r_{ss} &= \frac{V}{L+K_{US}V^2}\delta \end{aligned} \tag{5.15}$$

Because of the relationships in Eq. (5.15), the data points from Eqs. (5.13) and (5.14) are not linearly independent without sufficient excitation. In this case, Eqs. (5.13) and (5.14) become under-determined and therefore have multiple solutions. While all these solutions are mathematically valid, only one corresponds to the true physical values. In such a case, Eq.(5.9) gives the least norm estimates of cornering stiffness

and weight distribution, which are not necessarily the true values.

Linear dependency of $u_{y,CG}$, r, and δ due to lack of excitation in the experimental data can be graphically shown. Figure 5.6 shows plots of $u_{y,CG}$ vs. δ and r vs. δ from the experimental test. It is clearly seen that there exist strong linear relationships.

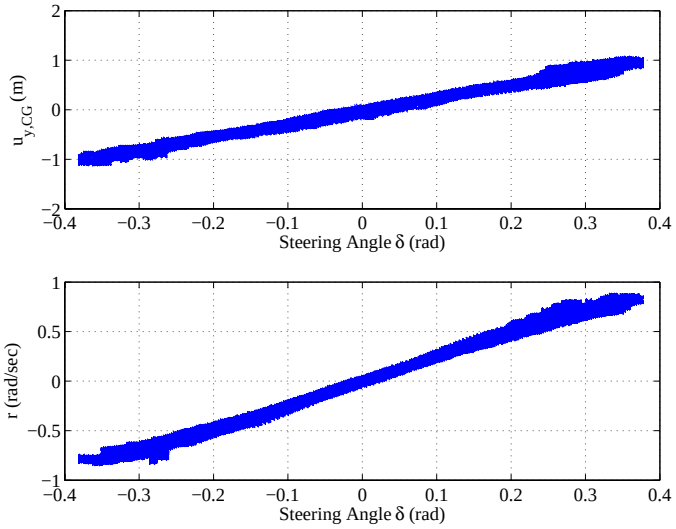

Figure 5.6: $u_{y,CG}$ vs. δ and r vs. δ from experimental test

Even though cornering stiffness and weight distribution can not be always estimated correctly, especially without sufficient excitation, the understeer gradient can be correctly identified. Suppose the vehicle lateral dynamics are not excited enough and the estimated cornering stiffness and weight distribution are not correct, Eqs. (5.13) and (5.13) still hold even in this case. The following equation is then derived Eq. (5.13):

$$u_{y,CG} \approx \frac{-aC_{\alpha f}r + bC_{\alpha r}r - mrV^2 + C_{\alpha f}V\delta}{C_{\alpha f} + C_{\alpha r}} \tag{5.16}$$

Substituting Eq. (5.16) in Eq. (5.14) gives:

$$\delta \approx \frac{(a+b)r}{V} - \frac{(aC_{\alpha f} - bC_{\alpha r})mrV}{(a+b)C_{\alpha f}C_{\alpha r}}$$

$$\begin{aligned} &= \frac{Lr}{V} + \frac{m}{L}(\frac{b}{C_{\alpha f}} - \frac{a}{C_{\alpha r}})rV \\ &= \frac{Lr}{V} + K_{US}\frac{rV}{g} \end{aligned} \tag{5.17}$$

Because Eq. (5.17) is from Eqs. (5.13) and (5.14), any combination of $C_{\alpha f}$, $C_{\alpha r}$, and a, which satisfies Eqs. (5.13) and (5.14) satisfies Eq. (5.17). It is then obvious that the understeer gradient, K_{US}, from the estimated $C_{\alpha f}$, $C_{\alpha r}$, and a using Eqs. (5.13) and (5.14), satisfies Eq. (5.17) and as a result, the estimated understeer gradient is correct even when the estimated $C_{\alpha f}$, $C_{\alpha r}$, and a are not correct individually.

While cornering stiffness and weight distribution cannot be estimated simultaneously without sufficient excitation, the cornering stiffness alone can be estimated correctly assuming the weight distribution is known. Table 5.4 shows estimated front and rear cornering stiffness from the same experimental and simulation data sets.

Simulation Input	$C_{\alpha f}$ (N/rad)	$C_{\alpha r}$ (N/rad)
0.1 Hz Sinusoid	98,770	152,840
0.4 Hz Sinusoid	98,470	154,740
2 Hz Sinusoid	98,840	153,060
Sinusoidal Sweep 0.1-0.5 Hz	98,260	154,310
Sinusoidal Sweep 0.1-1 Hz	98,790	155,860
Sinusoidal Sweep 0.1-2 Hz	98,840	152,980
Experiment	98,990	152,810
Reference Value	100,000	160,000

Table 5.4: Estimation Results of Front and Rear Cornering Stiffness

5.2.8 Estimation of Yaw Moment of Inertia with Cornering Stiffness

The previous section shows that cornering stiffness of a vehicle can be easily estimated using the proposed method. In addition, it shows that weight distribution of the vehicle can be estimated simultaneously when sufficient excitation exists. The remaining problem is to estimate yaw moment of inertia of the vehicle. In some cases, especially

for vehicle testing purposes, the mass and weight distribution of the vehicle can be measured using a scale, but the yaw moment of inertia is not easy to measure. Even though there exists a rule to approximate yaw moment of inertia of a vehicle [18], that is still just an approximation not an actual value, and the approximated value may not be accurate enough to analyze vehicle test results and control the vehicle. This section shows that yaw moment of inertia can be estimated together with cornering stiffness.

Similarly to Eq. (5.6), the bicycle model can be rewritten in terms of cornering stiffness, $C_{\alpha f}$ and $C_{\alpha r}$, and yaw moment of inertia, I_z, with known vehicle states as in the following equation.

$$\begin{bmatrix} \dot{u}_{y,CG} \\ \dot{r} \end{bmatrix} = \begin{bmatrix} f\left(u_{y,CG}, r, C_{\alpha f}, C_{\alpha r}, I_z\right) \\ g\left(u_{y,CG}, r, C_{\alpha f}, C_{\alpha r}, I_z\right) \end{bmatrix} \tag{5.18}$$

Then, the above equation can be expressed in a discrete form using the Euler method as follows:

$$\begin{bmatrix} u_{y,CG}(k+1) \\ r(k+1) \end{bmatrix} = \begin{bmatrix} u_{y,CG}(k) + f\left(u_{y,CG}(k), r(k), C_{\alpha f}, C_{\alpha r}, I_z\right)\Delta T \\ r(k) + g\left(u_{y,CG}(k), r(k), C_{\alpha f}, C_{\alpha r}, I_z\right)\Delta T \end{bmatrix} \tag{5.19}$$

where ΔT represents the sampling time.

Based on Eq. (5.19), the nonlinear total least squares method, similarly to Eq. (5.9), can be applied to estimate cornering stiffness, $C_{\alpha f}$ and $C_{\alpha r}$, and yaw moment of inertia, I_z. Figure 5.7 shows the estimation results from a experimental test. The estimates converge to the correct values in less than ten iterations.

In fact, it turns out that the estimation of yaw moment of inertia fails when there is not sufficient excitation similarly to the estimation of weight distribution. Unlike the case of simultaneous estimation of cornering stiffness and weight distribution, the estimation of yaw moment of inertia often diverges when the estimation fails. This is because the yaw moment of inertia, I_z, exists only in denominators of the bicycle model and drops out when there is not sufficient excitation as shown in Eq. (5.14).

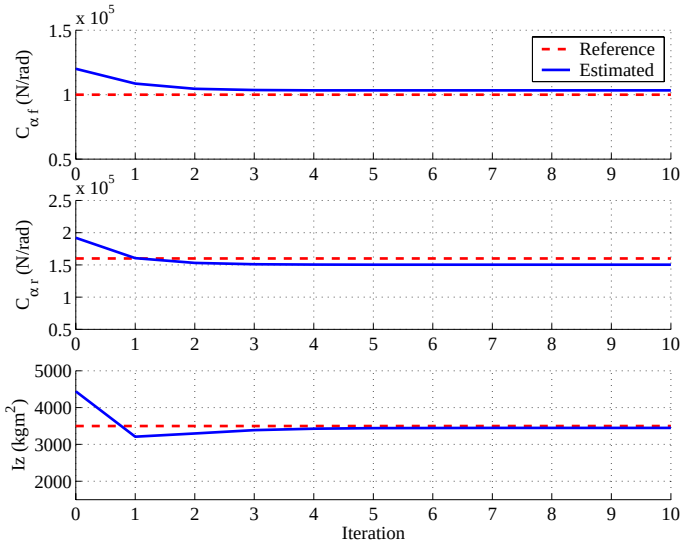

Figure 5.7: Estimation of Front and Rear Tire Cornering Stiffness and Yaw Moment Inertia

5.2.9 Discussion of Bicycle Model Parameter Estimation

The previous sections show that cornering stiffness, weight distribution, understeer gradient, and yaw moment of inertia can be estimated using the vehicle state estimates from the GPS/INS method. Table 5.5 is the summary of the estimation results with various methods and conditions.

These estimated parameters can be used to improve control and estimation schemes, such as stability control, steer-by-wire controller design and lateral control on an automated highway, or diagnostic systems that monitor tire condition and friction detection algorithms. However, note that the estimated cornering stiffnesses of tires may not be the true physical values of the tires even though the estimated values fit well with the bicycle model. The estimated tire cornering stiffnesses are the best fit for the bicycle model but not the true physical cornering stiffnesses of the tires. This follows from the fact that compliance and roll steer effects are lumped with cornering stiffness in the bicycle model. In order to study the true physical tire properties with cornering stiffness, more detailed models should be introduced including roll steer, camber change effect, etc.

Parameters to Estimate	Estimation Method	Note
Cornering stiffness	Least squares	Simple and fast Not very robust
Cornering stiffness	Total least squares	Robust and consistent Heavy computational power
Cornering stiffness and weight distribution	Total least squares	Converge to correct values with sufficient excitation Even when fail, give correct understeer gradient estimate
Cornering stiffness and yaw moment of inertia	Total least squares	Work well with sufficient excitation Diverge without sufficient excitation

Table 5.5: Summary of Estimation Results

5.3 Roll Parameter Estimation

5.3.1 Introduction

The previous section shows that the bicycle model parameters, such as cornering stiffness and yaw moment of inertia, can be estimated using the vehicle states from the two-antenna GPS setup with INS sensors. This section shows that parameters related to vehicle roll dynamics can also be estimated using the vehicle states from the GPS/INS setup. Since vehicle roll dynamics models are used in many rollover prevention or warning systems [10, 12, 24], properly estimated roll parameters are very critical for those systems.

5.3.2 Estimation Method

The following linear second order model (spring-damper-mass system) for roll dynamics is used for the estimation [52].

$$I_x\ddot{\phi}_k + b_r\dot{\phi}_k + k_r\phi_k = ma_yh + mgh\phi_k \tag{5.20}$$

where

I_x, b_r, k_r = roll moment of inertia, damping ration and stiffness

ϕ_k = suspension roll angle

m = vehicle mass

a_y = lateral acceleration of the vehicle

h = distance between roll center and center of mass

The roll angle, roll rate, and lateral acceleration can be measured from the GPS receiver and INS sensors. Because the roll acceleration is not directly available, numerical differentiation of the roll rate is used to get the roll acceleration. The roll moment of inertia, damping ratio, and stiffness can be estimated using a least squares estimator. Since the roll measurements include the road superelevation as well as the suspension roll, experimental runs should be performed with sufficient length of time and test path to average out the contribution from road superelevation changes.

5.3.3 Estimation Results

The roll stiffness and damping ratio are estimated by exciting the vehicle roll dynamics. An approximated value for the roll moment of inertia [18] is used because normal driving does not create sufficient excitation to accurately identify the moment of inertia. In order to minimize the interference from road superelevation changes, several experimental runs are performed on a fairly flat surface.

The estimated roll stiffness and damping ratio are shown in Fig. 5.8. The least squares fit is shown as a line going through the data points. To verify the result, the roll stiffness is also estimated by performing a series of constant radius turns at constant speed. The vehicle experiences different roll angles with various speeds since the lateral acceleration varies along with the speed. Figure 5.9 shows the plot of roll angle vs. lateral acceleration as well as the estimated roll stiffness. A line going through the data points represents the least squares best fit of the roll rate. The estimated roll stiffness from the constant speed turns is very similar to the roll

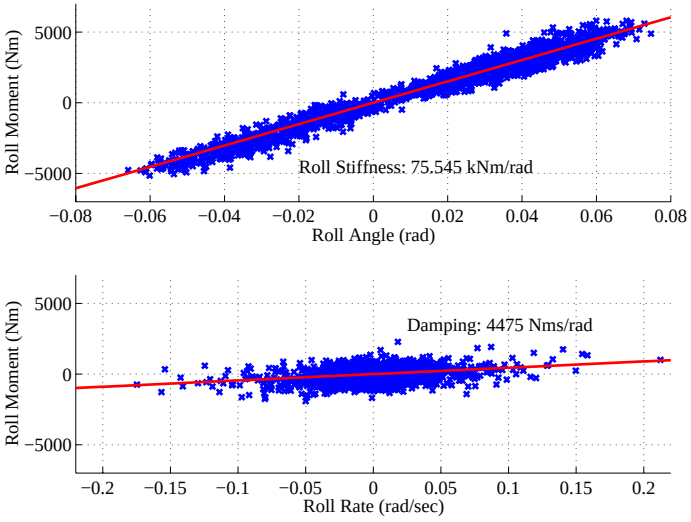

Figure 5.8: Roll Moment of Inertia and Damping Ratio Estimates

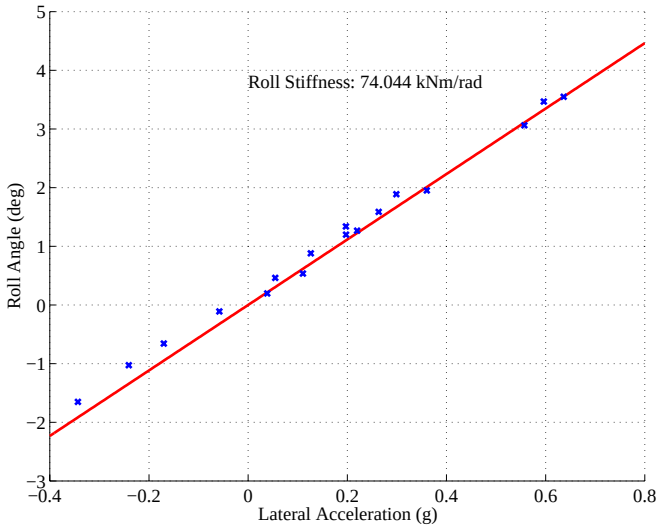

Figure 5.9: Roll Angle vs. Lateral Acceleration

stiffness estimated in Fig. 5.8. The difference between two roll stiffness estimates is less than 5%.

In addition, several step steer maneuvers are performed to validate the estimation result. Figure 5.10 and 5.11 show the measured roll angle and roll rate as well as the simulated values using estimated parameters. It is clearly seen that major response

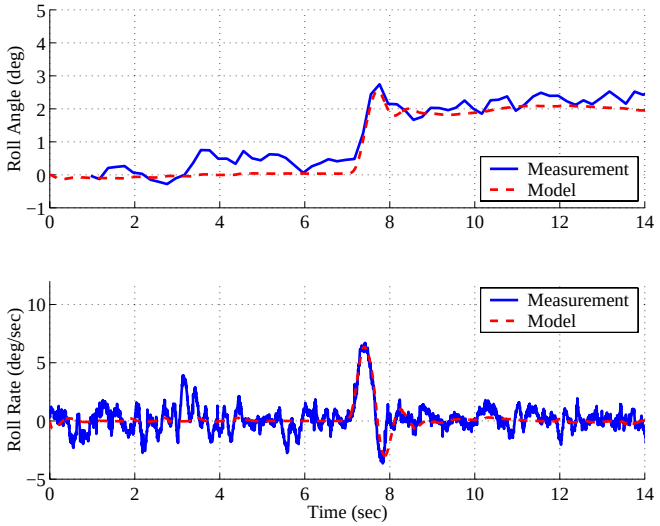

Figure 5.10: Comparison of Step Steer Response

characteristics such as rise time, overshoot, and steady state value are well matched between the measured and simulated roll angle and rate. Note that unevenness of the test path creates differences between the measured and simulated values because the unevenness is not included in the simulation. The slight discrepancies in the roll rate comparisons, especially after the peaks, can be explained by nonlinearity in the dampers because the simulation assumes a linear damper. When a vehicle has nonlinearity in the damping characteristics, simulation with a linear model creates some discrepancies against measured values. Nevertheless, the overall match is quite good.

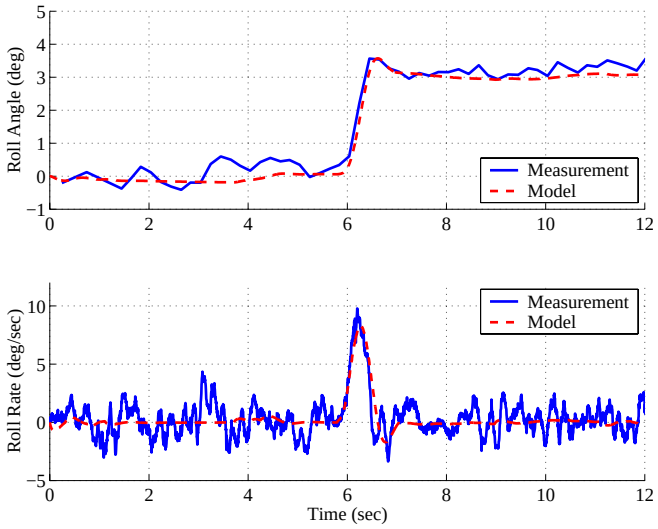

Figure 5.11: Comparison of Step Steer Response

5.4 Conclusion

This chapter shows that parameters of the bicycle model – such as tire cornering stiffness, weight distribution, and yaw moment of inertia – can be estimated using the vehicle state estimates from the GPS/INS method. The conventional least squares method can be used for the estimation, but the total least squares method yields more robust and consistent estimates of the parameters due to the noise structure of the estimation problem. In addition, it is shown that sufficient excitation is critical to estimate weight distribution and yaw moment of inertia. Estimates of weight distribution and yaw moment of inertia fails to converge correct values without sufficient excitation. However, it is shown that the understeer gradient can be estimated correctly even without high levels of excitation. This chapter also shows that the vehicle roll parameters – such as roll stiffness and roll damping ratio – can be estimated using the least squares method. Estimated parameters with parameterized vehicle dynamics models can be used for a wide variety of applications such as vehicle stability control and rollover prevention systems

Chapter 6

Estimation of Suspension Roll and Road Bank

6.1 Introduction

Vehicle stability control systems and state estimators commonly use lateral acceleration measurements from accelerometers to calculate lateral acceleration and sideslip angle of the vehicle [47, 48]. These acceleration measurements, however, are easily affected by disturbances such as road bank angle and suspension roll induced by suspension deflection. Since these unwanted effects in acceleration measurements can lead to false estimation of the vehicle states or misleading activation of the stability control systems, knowledge of the suspension roll and road bank angles is extremely important for such systems.

As a result, many researchers have pointed out that detection of the road bank angle and suspension roll is necessary for the satisfactory performance of such systems [38, 47, 48]. Over the last few years, several methods were proposed to estimate the road bank angle. Nishio et al. esimated the road bank angle by comparing model-generated acceleration and lateral accelerometer measurements [38]. Tseng used dynamic inverse transfer functions derived from the bicycle model to estimate road bank angle [46]. Hahn et al. designed a disturbance observer for road bank angle estimation using the bicycle model [26]. However, the suspension roll induced by

suspension deflection was neglected or was lumped with the road bank angle in these methods. While a lumped value can be used to compensate the acceleration measurements [41], the separation of these two angles could be especially beneficial to vehicle rollover warning and avoidance systems [10, 24]. Since a small lumped value does not necessarily mean a small road bank angle, a vehicle may experience a significant road bank angle even though the sum of the two angles is small. The vehicle rollover warning or avoidance systems may need to be aware of this because a significant road bank angle can create different behavior of the vehicle during transient maneuvering, when most rollover accidents actually happen.

The main challenge in separating road bank angle and suspension roll angle is that it is difficult to differentiate one from the other by using typical roll-related measurements (lateral acceleration and roll rate). Since the lateral accelerometers are usually attached to the vehicle body, the road bank angle and suspension roll have the exact same effect on the lateral acceleration measurements and are not differentiable. The roll rate gyros are also attached to the vehicle body and can only see changes of the road bank and suspension roll angles together, not individual changes separately. Therefore, suspension roll and road bank angles cannot be directly separated using the kinematic relationships of the roll-related measurements.

Even though the suspension roll and road bank angles have similar and indistinguishable influences on the measurements, they play very different roles in the vehicle dynamics. While the road bank angle can be treated as a disturbance or unknown input to the vehicle, the suspension roll angle is a state resulting from the road bank angle and other inputs, governed by vehicle dynamics. This implies that a parameterized vehicle dynamic model could conceivably be used to separate the suspension roll and road bank angles. The previous chapters show that parameters of such a model and vehicle states can be precisely estimated by combining GPS with inertial sensors.

Based on these results, this chapter presents a new method for identifying road bank and suspension roll separately using a disturbance observer and a vehicle dynamic model. First, a dynamic model, which includes suspension roll as a state and

road bank as a disturbance, is introduced. The disturbance observer is then implemented using the estimates of the sideslip angle and vehicle tilt angle (the sum of road bank and suspension roll angles). These estimates are accurately determined using GPS and INS as demonstrated in the previous chapters. From the disturbance observer, road bank angle and suspension roll can be separately estimated.

6.2 Road and Vehicle Kinematics

Figure 6.1 shows a conceptual schematic diagram for a vehicle roll model with road bank angle. It is assumed that the vehicle body rotates around the roll center of the vehicle. In Fig. 6.1, h is the height of the center of gravity (CG) from the roll center. ϕ_k and ϕ_r are the suspension roll angle and road bank angle respectively.

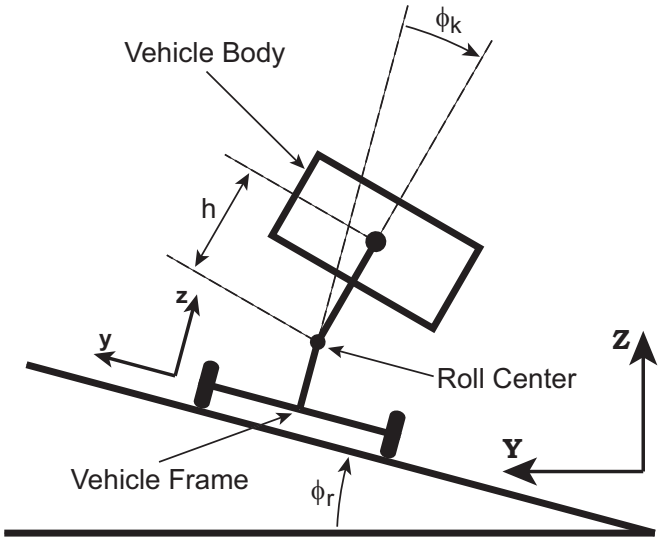

Figure 6.1: Vehicle Roll Model

If a roll rate gyro is attached to the vehicle body in Fig. 6.1, one might assume the roll rate gyro measures $\dot{\phi}_k + \dot{\phi}_r$, the sum of the rate of change of suspension roll angle and the rate of change of road bank angle. However, this is not what the roll rate gyro really measures. To illustrate this, assume a vehicle follows a circular path on a large flat plane with a slope of 10 degrees from the horizontal, and the vehicle

has no roll from suspension deflection ($\phi_k = 0$). The vehicle will then experience a road bank angle, ϕ_r, that changes from -10 to 10 degrees in one revolution of the circle. In this case, $\dot{\phi}_r$ is definitely not zero since the road bank angle experienced by the vehicle, ϕ_r, is continuously changing. However, the roll rate measurement is always zero because the angular velocity vector of the vehicle is orthogonal to the axis of the roll rate gyro and as a result the roll rate gyro cannot sense the change of the road bank angle. As this example shows, a careful treatment of the kinematics is necessary before a disturbance observer for estimating the vehicle and road bank angles can be implemented.

In this work, the vehicle frame is assumed to keep contact with the ground. Under this assumption, the roll and pitch motions of the vehicle frame are totally constrained by the road, and the road bank angle and road grade are the same as the roll and pitch angles of the vehicle frame in the inertial frame. Consequently, the attitude of the vehicle frame with respect to the inertial coordinates is first defined by the Euler angles in this work, and the rate of change of the road bank angle is expressed in terms of the angular velocities of the vehicle frame.

When the rotation of the vehicle frame is given by the Euler angles (ψ, θ, ϕ) about vehicle-frame-fixed axes according to the ISO standard (ISO 8855) [30], where the first rotation is by an angle ψ about the z axis, the second is by an angle θ about the y axis, and the third is by an angle ϕ about the x axis, the transformation matrix from the inertial coordinates to the vehicle-frame-fixed coordinates is given in Eq. (6.1).

$$
\begin{aligned}
Q_{30} &= Q_{32}Q_{21}Q_{10} \\
Q_{10} &= \begin{bmatrix} \cos\psi & \sin\psi & 0 \\ -\sin\psi & \cos\psi & 0 \\ 0 & 0 & 1 \end{bmatrix} \\
Q_{21} &= \begin{bmatrix} \cos\theta & 0 & -\sin\theta \\ 0 & 1 & 0 \\ \sin\theta & 0 & \cos\theta \end{bmatrix}
\end{aligned}
\tag{6.1}
$$

$$Q_{32} = \begin{bmatrix} 1 & 0 & 0 \\ 0 & \cos\phi & \sin\phi \\ 0 & -\sin\phi & \cos\phi \end{bmatrix}$$

The subscript 0 indicates the inertial coordinates and the subscript 3 represents the vehicle-frame-fixed coordinates. Similarly, the subscript 1 describes the intermediate coordinates given by the rotation about the z axis from the inertial coordinates 0, and the subscript 2 denotes the intermediate coordinates given by the rotation about the y axis from the intermediate coordinates 1.

The angular velocity vector of the vehicle frame with respect to the inertial coordinates, which is expressed in the vehicle-frame-fixed coordinates, is defined as:

$$\omega_{30,3} = [\ p_f \quad q_f \quad r_f\ ]^T \tag{6.2}$$

where p_f, q_f, and r_f represent the x, y, and z components of the angular velocity vector, $\omega_{30,3}$. The first two subscripts 30 mean that $\omega_{30,3}$ is the angular velocity of 3 (the vehicle frame) with respect to 0 (the inertial frame), and the last subscript 3 means the vector is expressed in 3 (the vehicle-frame-fixed coordinates).

Using Eq. (6.1), the relationship between the vehicle-frame-fixed angular velocity vector, $\omega_{30,3}$, and the rate of change of the Euler angles, $[\ \dot{\psi} \quad \dot{\theta} \quad \dot{\phi}\ ]^T$, can be determined by resolving the Euler rates into the vehicle-frame-fixed coordinates:

$$\begin{bmatrix} p_f \\ q_f \\ r_f \end{bmatrix} = Q_{32} \begin{bmatrix} \dot{\phi} \\ 0 \\ 0 \end{bmatrix} + Q_{32}Q_{21} \begin{bmatrix} 0 \\ \dot{\theta} \\ 0 \end{bmatrix} + Q_{32}Q_{21}Q_{10} \begin{bmatrix} 0 \\ 0 \\ \dot{\psi} \end{bmatrix} = J \begin{bmatrix} \dot{\phi} \\ \dot{\theta} \\ \dot{\psi} \end{bmatrix} \tag{6.3}$$

The Euler rates can be then determined from the vehicle-frame-fixed angular velocity vector by inverting J:

$$\begin{bmatrix} \dot{\phi} \\ \dot{\theta} \\ \dot{\psi} \end{bmatrix} = \begin{bmatrix} 1 & \sin\phi\tan\theta & \cos\phi\tan\theta \\ 0 & \cos\phi & -\sin\phi \\ 0 & \sin\phi/\cos\theta & \cos\phi/\cos\theta \end{bmatrix} \begin{bmatrix} p_f \\ q_f \\ r_f \end{bmatrix} \tag{6.4}$$

$$\therefore \dot{\phi} = p_f + \sin\phi \tan\theta\, q_f + \cos\phi \tan\theta\, r_f \tag{6.5}$$

When the Euler angle θ is not zero, the Euler angle ϕ is not the same as the road bank angle, ϕ_r, illustrated in Fig. (6.1), because the road bank angle is defined between the vehicle frame and the intermediate coordinates 1. Similarly, $\dot{\phi}_r$ is not the same as $\dot{\phi}$ unless θ is zero. However, $\dot{\phi}_r$ is the x component of the angular velocity, $\omega_{31,1}$, since $\omega_{31,1}$ represents the angular velocity of the vehicle frame with respect to the intermediate coordinates 1. Therefore, the rate of change of the road bank angle, $\dot{\phi}_r$, is given by the following equation:

$$\begin{aligned} \omega_{31,1} &= \begin{bmatrix} \dot{\phi}_r \\ \dot{\theta}_r \\ \dot{\psi}_r \end{bmatrix} = Q_{12} \begin{bmatrix} \dot{\phi} \\ 0 \\ 0 \end{bmatrix} + \begin{bmatrix} 0 \\ \dot{\theta} \\ 0 \end{bmatrix} \\ &= Q_{21}^{-1} \begin{bmatrix} \dot{\phi} \\ 0 \\ 0 \end{bmatrix} + \begin{bmatrix} 0 \\ \dot{\theta} \\ 0 \end{bmatrix} = \begin{bmatrix} \cos\theta\,\dot{\phi} \\ \dot{\theta} \\ -\sin\theta\,\dot{\phi} \end{bmatrix} \end{aligned} \tag{6.6}$$

$$\therefore \dot{\phi}_r = \cos\theta\,\dot{\phi} \tag{6.7}$$

where ϕ_r and θ_r represent the road bank angle and road grade respectively. Using Eq. (6.5), Eq. (6.7) can be rewritten as:

$$\dot{\phi}_r = \cos\theta\, p_f + \sin\phi \sin\theta\, q_f + \cos\phi \sin\theta\, r_f \tag{6.8}$$

Since the yaw rate gyro and the roll rate gyro are attached to the vehicle body, the yaw and roll rates of the vehicle frame, r_f and p_f respectively, cannot be exactly measured. The yaw and roll rate gyros measure the yaw and roll rates of the vehicle body and the measurements include the effects of roll motion of the vehicle body. Since the vehicle-body-fixed coordinates are defined from a rotation by the angle ϕ_k about the x axis of the vehicle-frame-fixed coordinates, the transformation matrix from the vehicle-frame-fixed coordinates to the vehicle-body-fixed coordinates is given

by:

$$Q_{43} = \begin{bmatrix} 1 & 0 & 0 \\ 0 & \cos\phi_k & \sin\phi_k \\ 0 & -\sin\phi_k & \cos\phi_k \end{bmatrix} \tag{6.9}$$

where the subscript 4 indicates the vehicle-body-fixed coordinates.

Using Eq. (6.9), The yaw rate of the vehicle body, r_b, and the roll rate of the vehicle body, p_b, can be written as:

$$\omega_{40,4} = \begin{bmatrix} p_b \\ q_b \\ r_b \end{bmatrix} = \begin{bmatrix} \dot{\phi}_k \\ 0 \\ 0 \end{bmatrix} + Q_{43} \begin{bmatrix} p_f \\ q_f \\ r_f \end{bmatrix} \tag{6.10}$$

$$\therefore p_b = p_f + \dot{\phi}_k \tag{6.11}$$

$$r_b = \cos\phi_k\, r_f - \sin\phi_k\, q_f \tag{6.12}$$

where p_b and r_b are are the roll rate and yaw rate of the vehicle body. Note that Eq. (6.11) says that the roll rate of the vehicle body, p_b, is not the same as $\dot{\phi}_k + \dot{\phi}_r$, the sum of the rate of the suspension roll angle change and the rate of the road bank angle change, as explained in the beginning of this section.

Eq. (6.8) can be rewritten by defining a new variable ε_r and assuming the vehicle pitch angle θ is small and so $\cos\theta$ is close to one:

$$\dot{\phi}_r \approx p_f + \varepsilon_r \tag{6.13}$$

where

$$\varepsilon_r = \sin\phi \sin\theta\, q_f + \cos\phi \sin\theta\, r_f$$

Eq. (6.12) can be also simplified as Eq. (6.14) assuming the suspension roll angle, ϕ_k, and the pitch rate, q_f, are small:

$$r_b \approx r_f \tag{6.14}$$

Therefore, the yaw rate and roll rate measurements can be described using Eqs. (6.11),

(6.13), and (6.14).

$$\begin{aligned} r_m &= r_b \approx r_f \\ p_m &= p_b = p_f + \dot{\phi}_k \\ &= \dot{\phi}_k + \dot{\phi}_r - \varepsilon_r = \dot{\phi} - \varepsilon_r \end{aligned} \tag{6.15}$$

where

$$\begin{aligned} r_m &= \text{yaw rate gyro measurement} \\ p_m &= \text{roll rate gyro measurement} \\ \dot{\phi} &= \dot{\phi}_k + \dot{\phi}_r \end{aligned}$$

6.3 Vehicle Model

The dynamics of a vehicle are represented here by the single track, or bicycle model with a roll mode [10]. It is assumed that the slip angles on the inside and outside wheels are approximately the same. The equations of motion can be linearized as in Eqs. (6.16), (6.17), and (6.18) assuming the road changes smoothly.

$$\begin{aligned} \dot{\beta} &= -\frac{I_{eq}C_0}{I_x m u_x}\beta - \left(1 + \frac{I_{eq}C_1}{I_x m u_x^2}\right) r_f + \frac{h(mgh - k_r)}{I_x u_x}\phi_k - \frac{hb}{I_x u_x}\dot{\phi}_k \\ &\quad + \frac{I_{eq}C_{\alpha f}}{I_x m u_x}\delta - \frac{g}{u_x}\phi_r \end{aligned} \tag{6.16}$$

$$\dot{r_f} = -\frac{C_1}{I_z}\beta - \frac{C_2}{I_z u_x} r_f + \frac{aC_{\alpha f}}{I_z}\delta \tag{6.17}$$

$$\ddot{\phi}_k = -\frac{C_0 h}{I_x}\beta - \frac{C_1 h}{I_x u_x} r_f + \frac{mgh - k_r}{I_x}\phi_k - \frac{b_r}{I_x}\dot{\phi}_r + \frac{C_{\alpha f} h}{I_x}\delta - \dot{p_f} \tag{6.18}$$

where

$$C_0 = C_{\alpha f} + C_{\alpha r}, \quad C_1 = aC_{\alpha f} - bC_{\alpha r}$$
$$C_2 = a^2 C_{\alpha f} + b^2 C_{\alpha r}, \quad I_e q = I_x + mh^2$$

β is the sideslip angle at the center of the vehicle frame, and r_f is the yaw rate of the vehicle frame. I_x is the moment of inertia about the roll axis, k_r is the roll stiffness, and b_r is the roll damping coefficient. h is the height of CG from the roll center. Note that the lateral force from gravity due to the road bank angle, ϕ_r, appears in Eq. (6.16), which describes the vehicle lateral dynamics, and the time derivative of p_f affects the vehicle roll dynamics in Eq. (6.18). The change of p_f, the roll rate of the vehicle frame, is related to the change of the road bank angle through Eq. (6.13) since the vehicle frame is assumed to keep contact on the ground.

From Eqs. (6.16), (6.17), and (6.18), the following four-state linear model can be written in the state space form:

$$\dot{x} = Ax + B\delta + B_{w1}\phi_r + B_{w2}\dot{p_f} \tag{6.19}$$

where

$$x = \begin{bmatrix} \beta & r_f & \phi_k & \dot{\phi_k} \end{bmatrix}^T$$

$$A = \begin{bmatrix} -\frac{I_{eq}C_0}{I_x m u_x} & -1 - \frac{I_{eq}C_1}{I_x m u_x^2} & \frac{h(mgh-k_r)}{I_x u_x} & -\frac{hb}{I_x u_x} \\ -\frac{C_1}{I_z} & -\frac{C_2}{I_z u_x} & 0 & 0 \\ 0 & 0 & 0 & 1 \\ -\frac{C_0 h}{I_x} & -\frac{C_1 h}{I_x u_x} & \frac{mgh-k_r}{I_x} & -\frac{b_r}{I_x} \end{bmatrix}$$

$$B = \begin{bmatrix} \frac{I_{eq}C_{\alpha f}}{I_x m u_x} & \frac{aC_{\alpha f}}{I_z} & 0 & \frac{C_{\alpha f}h}{I_x} \end{bmatrix}^T$$

$$B_{w1} = \begin{bmatrix} -\frac{g}{u_x} & 0 & 0 & 0 \end{bmatrix}^T$$

$$B_{w2} = \begin{bmatrix} 0 & 0 & 0 & -1 \end{bmatrix}^T$$

Note that the road bank angle, ϕ_r, and the time derivative of p_f are treated as disturbances or unknown inputs to the vehicle dynamics while the suspension roll angle, ϕ_k, is a state resulting from the road bank angle and other inputs.

6.4 Disturbance Observer

The road bank angle, ϕ_r, and the time derivative of p_f are the two disturbances to the vehicle dynamics described in Eq. (6.19). Since the road changes independently, the disturbances due to the road vary independently of the vehicle dynamics. However, the two disturbances are not independent of each other as shown in Eq. (6.13). Therefore, dynamics of the disturbances can be described as follows assuming that the disturbances due to the road changes are the result of white noise forcing $\ddot{p_f}$ and $\dot{\varepsilon_r}$ [26].

$$\dot{w} = A_w w \tag{6.20}$$

where

$$w = \begin{bmatrix} \phi_r \\ p_f \\ \dot{p_f} \\ \varepsilon_r \end{bmatrix}, \quad A_w = \begin{bmatrix} 0 & 1 & 0 & 1 \\ 0 & 0 & 1 & 0 \\ 0 & 0 & 0 & 0 \\ 0 & 0 & 0 & 0 \end{bmatrix}$$

From Eqs. (6.19) and (6.20), a disturbance observer can be implemented by augmenting the disturbances to the state vector. A new state vector z is defined by augmenting w to the vehicle state vector x.

$$\dot{z} = \begin{bmatrix} A & B_w \\ 0 & A_w \end{bmatrix} z + \begin{bmatrix} B \\ 0 \end{bmatrix} \delta = Fz + G\delta \tag{6.21}$$

where

$$z = \begin{bmatrix} x & w \end{bmatrix}^T, \quad B_w = \begin{bmatrix} B_{w1} & 0 & B_{w2} & 0 \end{bmatrix}$$

The available measurements are:

$$y = \begin{bmatrix} \beta \\ r_m \\ \phi \\ p_m \end{bmatrix} = \begin{bmatrix} \beta \\ r_f \\ \phi_k + \phi_r \\ \dot{\phi}_k + p_f \end{bmatrix} = \begin{bmatrix} 1 & 0 & 0 & 0 & 0 & 0 & 0 & 0 \\ 0 & 1 & 0 & 0 & 0 & 0 & 0 & 0 \\ 0 & 0 & 1 & 0 & 1 & 0 & 0 & 0 \\ 0 & 0 & 0 & 1 & 0 & 1 & 0 & 0 \end{bmatrix} z = Hz \tag{6.22}$$

The yaw rate, r_f, and the sum of the suspension roll rate and the rate of change of the roll angle of the vehicle frame, $\dot{\phi}_k + p_f$, are from the rate gyros according to Eq. (6.15). The sideslip angle, β, and the sum of the suspension roll and road bank angle, $\phi_k + \phi_r$, are from the integration of GPS and INS.

Since the new system from Eqs. (6.21) and (6.22) is observable, a disturbance observer is given by the following equation:

$$\dot{\hat{z}} = F\hat{z} + Gu + L(y - H\hat{z}) \tag{6.23}$$

The corresponding error dynamics are then described as follows:

$$\dot{\tilde{z}} = (F - LH)\tilde{z} \tag{6.24}$$

where

$$\tilde{z} = z - \hat{z}$$

When the observer gain, L, is selected so that $F - LH$ has stable eigenvalues and the error dynamics are significantly faster than the system dynamics, or by applying a Kalman filter, the error dynamics approach zero [22]. In this work, a Kalman filter is applied to determine the observer gain.

6.5 Experimental Results

A Mercedes E-class wagon is used for the experimental tests. The test vehicle is equipped with a 3-axis accelerometer/gyro triad and a two-antenna GPS system. The

parameters of the vehicle model are accurately estimated using GPS measurements from a two-antenna system combined with INS sensors as described in the earlier section.

Figure 6.2 shows experimental results for estimating suspension roll and road bank angles using the proposed disturbance observer. Experimental tests consisting of four laps around an uneven surface are performed.

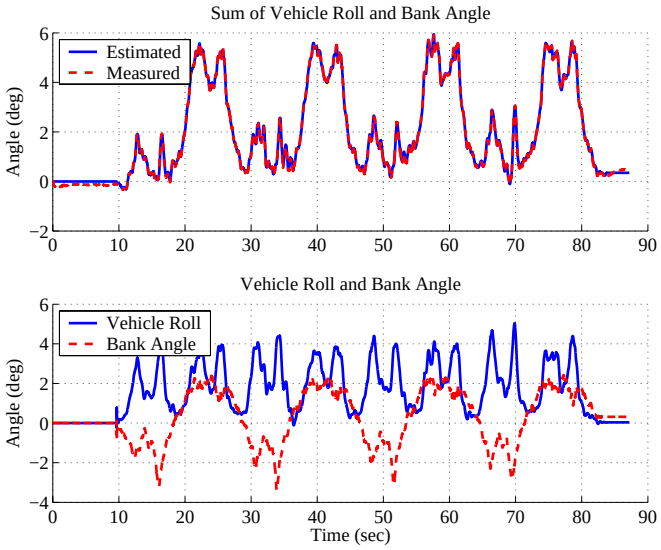

Figure 6.2: suspension roll and Bank Angle Estimates

The lower plot shows estimated suspension roll and road bank angles individually, and the upper plot shows the sum of those two estimated values compared with the measured value using the two-antenna GPS setup combined with INS. Note that the sum of suspension roll and road bank angles is mainly positive even though the road bank angle alone fluctuates almost evenly between positive and negative values. As easily seen in Fig. 6.2 at around 30, 50, and 70 seconds, a small value of the roll angle measurement – the sum of suspension roll and road bank angles – does not necessarily mean a small suspension roll angle and small road bank angle. A significant road bank angle can be a major factor in transient maneuvering, which is the cause of most rollover accidents.

To verify the estimates of the road bank angle, the true road bank angle is measured using a two-antenna GPS setup. The two GPS antennas are placed laterally on the top of the vehicle, and record the static roll angle as the vehicle moves along the marked path at a very low speed to avoid exciting vehicle roll dynamics. Since the measured roll angle from GPS contains both the road bank angle and the suspension roll angle, the suspension roll angle is then calculated from the estimated roll stiffness and subtracted from total roll angle [42]. The remaining angle is assumed to be the true road bank angle and is validated by repeating this test in the opposite direction of travel.

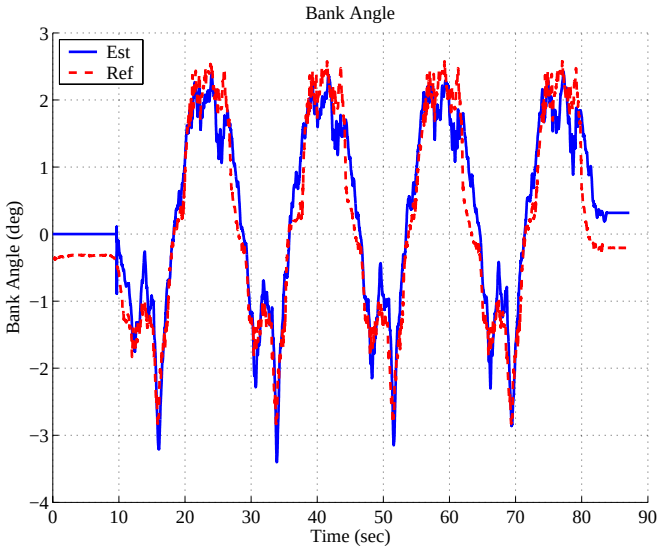

Figure 6.3: Verification of Road Bank Angle Estimates

The estimated road bank angle from the proposed method is verified with this measured road bank angle in Fig. 6.3. The estimates match to within the accuracy of the static road bank measurement technique, suggesting that dynamic separation works well. In addition, slalom maneuvers on a fairly flat surface are performed to validate the estimation method. Figure 6.4 shows estimated suspension roll and road bank angles from the slalom maneuvers as well as measurements of the vehicle lateral acceleration.

As expected, the estimated road bank angle is very small (mostly less than one

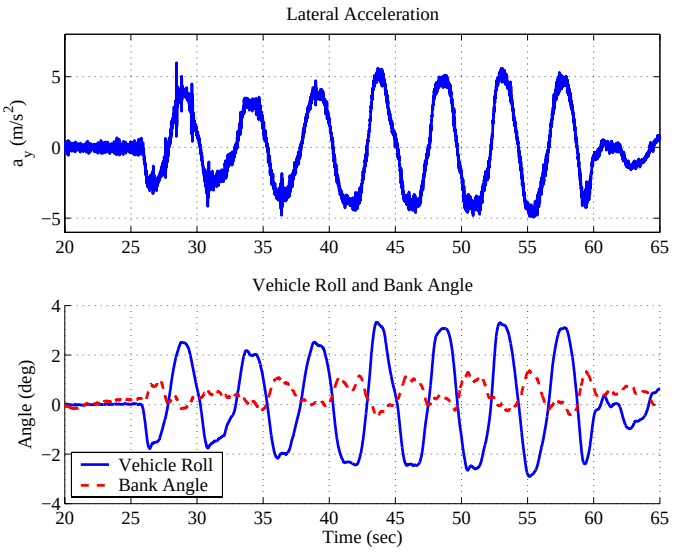

Figure 6.4: Measured Lateral Acceleration and Estimates of suspension roll and Bank Angles

degree), which reflects the fact that the test is performed on a fairly flat surface. The estimated suspension roll angle also shows strong correlation with the measured lateral acceleration, which can be predicted from the vehicle roll dynamics only when the effects from road bank are insignificant. In fact, small fluctuations in the estimated road bank angle can be explained by unevenness of the test surface. The slalom tests are performed on a runway at Moffett airfield, and the runway has road crown for water drainage. Therefore, the road crown is estimated as road bank angle. The estimated road bank angle is shown to have a strong correlation with vehicle heading and position, which can be easily explained by the fact that there exists almost identical road crown along the whole runway.

Chapter 7

Conclusion and Future Work

7.1 Conclusion

With the combination of a two-antenna GPS receiver and four automotive grade inertial sensors (two rate gyros and two accelerometers), it is possible to develop an estimate of vehicle sideslip corrected for roll and grade effects. The proposed method provides high update estimates of sideslip, longitudinal velocity, roll and grade and compares well to predictions from calibrated models and Kalman filter analysis. The complete system calibrates the inertial sensor sensitivities and biases at appropriate update rates and can handle loss of the GPS signal for periods of time by simply integrating the calibrated inertial sensors. The vehicle states obtained by this system represent a new level of fidelity for vehicle control and have been successfully implemented in steer-by-wire control. A full state feedback controller has been developed to alter a vehicle's handling characteristics by augmenting the driver's steering input. This work represents one of the first applications of GPS-based state estimation to dynamic control of a vehicle with active steering. Future work will investigate the possible extent of vehicle handling modification by active steering and any fundamental limitations imposed by the feedback or control structure.

Once the vehicle states are precisely estimated, key vehicle parameters – such as tire cornering stiffness, understeer gradient, yaw moment of inertia, roll stiffness, and roll damping coefficient – can be estimated easily with proper excitation using the

estimated states. With these properly estimated parameters, parameterized vehicle dynamics models can be used for a wide variety of applications including highway automation, vehicle stability control, and rollover prevention systems. Finally, a properly formulated disturbance observer and measurements from the GPS and INS sensors can separately estimate road bank angle and suspension roll. These results can be used for a wide variety of applications including vehicle stability control systems, state estimators, and vehicle rollover warning and avoidance systems.

7.2 Future Work

This thesis shows that accurate vehicle state and parameter estimation is possible using GPS/INS. A natural direction for this work is to use these estimates to improve stability control systems. This is especially true on steer-by-wire vehicles, in which the presence of active steering as well as differential braking allows more full utilization of the state estimates. Also, in a carefully designed steer-by-wire system, the aligning moment disturbance at the tires can be measured effectively by measuring the steering motor current. This is true regardless of whether the vehicle is being operated in the linear or nonlinear handling region [55]. The measured aligning moment can then be translated to the lateral force at the tires. The estimated lateral force along with the estimated states can be used by not only stability control systems but also tire parameter estimators particularly in the unpredictable nonlinear region.

In addition, the cornering stiffness estimation can be improved by considering more detailed vehicle models than the bicycle model. The bicycle model is a simplified model and does not include the complete dynamics of the vehicle and tires such as roll steer and chamber changes. In order to study the true physical cornering stiffness of the tire, not the best fit parameter for the bicycle mode, more detailed models must be considered.

Appendix A

Nonlinear Total Least Squares

This appendix covers the nonlinear total least squares method, which is used to estimate cornering stiffness and weight distribution. This appendix consists of two sections. The first section explains the nonlinear least squares method, which is a basis of nonlinear total least squares, and the second section covers the nonlinear total least squares method.

A.1 Nonlinear Least Squares

Suppose y is measured and the parameter, θ, needs to be estimated based on the following nonlinear equation:

$$y = f(\theta) \tag{A.1}$$

Since the measurement of y contains error, Δy, the parameter estimation problem can be reformulated as the following minimization problem in least-squares sense:

$$\begin{aligned} \min_{\theta} \|\hat{y} - f(\theta)\| \; &= \; \min \|\Delta y\| \\ \text{Subject to:} \quad \hat{y} &= f(\theta) + \Delta y \end{aligned} \tag{A.2}$$

where

$$\hat{y} = \text{measurement of } y$$

$$\Delta y = \text{measurement error}$$

The above nonlinear minimization problem can be solved by locally linearizing the constraint function and iteratively solving for the parameter, θ, which minimizes $\|\Delta y\|$.

Linearizing $f(\theta)$ gives:

$$f(\theta + \Delta\theta) = f(\theta) + Df|_{\theta}\,\Delta\theta \tag{A.3}$$

where

$$\begin{aligned} Df &= \frac{\partial f}{\partial \theta} \\ &= \text{gradient of } f \end{aligned}$$

Then, y can be written as follows to iteratively solve for θ:

$$y = f(\theta_k) + Df|_{\theta_k}\,\Delta\theta \tag{A.4}$$

where

$$\begin{aligned} \theta_k &= \text{current guess for } \theta \\ \Delta\theta &= \theta_{k+1} - \theta_k \end{aligned}$$

From the above equation:

$$\Delta\theta = Df|_{\theta_k}{}^{\dagger}\,(\hat{y} - f(\theta_k)) \tag{A.5}$$

where

$$Df|_{\theta_k}{}^{\dagger} = \text{linear least squares pseudo-inverse of } Df|_{\theta_k}$$

Each iteration step will be then:

$$\theta_{k+1} = \theta_k + Df|_{\theta_k}{}^{\dagger} (\hat{y} - f(\theta_k)) \tag{A.6}$$

Equation (A.6) is initialized with the initial value, θ_0, and is iterated until the solution converges. For most cases, this equation converges in less than ten steps if this algorithm converges.

However, Eq. (A.6) fails to converge sometimes if the function is locally not close to convex. Then, damping can be added to the equation to make sure that the solution converges.

$$\theta_{k+1} = \theta_k + \alpha\, Df|_{\theta_k}{}^{\dagger} (\hat{y} - f(\theta_k)) \tag{A.7}$$

where the damping coefficient, α, is between 0 and 1. For the cornering stiffness and yaw moment of inertia estimation problems, 0.8 works well.

A.2 Nonlinear Total Least Squares

Suppose x and y are measured and the parameter, θ, needs to be estimated based on the following nonlinear equation:

$$y = f(x, \theta) \tag{A.8}$$

Since the measurements, x and y, contain errors, Δx and Δy respectively, the parameter estimation problem can be reformulated as the following minimization problem:

$$\begin{aligned} \min_{x,\theta} \left\| \begin{array}{c} \hat{y} - f(x,\theta) \\ \hat{x} - x \end{array} \right\| &= \min \left\| \begin{array}{c} \Delta y \\ \Delta x \end{array} \right\| \\ \text{Subject to:} \quad \hat{y} - \Delta y &= f(\hat{x} - \Delta x, \theta) \end{aligned} \tag{A.9}$$

where

$$\hat{x},\ \hat{y} = \text{measurement of } x \text{ and } x$$

$$\Delta x,\ \Delta y = \text{measurement errors}$$

Equation (A.9) can be rewritten by introducing new variables, $\hat{Y}$ and z, and new function $g(z)$ as follows:

$$\begin{aligned} \min_z \left\| \hat{Y} - g(z) \right\| &= \min \|\Delta Y\| \\ \text{Subject to:} \quad \hat{Y} &= g(z) + \Delta Y \end{aligned} \tag{A.10}$$

where

$$\begin{aligned} \hat{Y} &= [\ \hat{y} \quad \hat{x}\ ]^T \\ \Delta Y &= [\ \Delta y \quad \Delta x\ ]^T \\ z &= [\ x \quad \theta\ ]^T \\ g(z) &= [\ f(x,\theta) \quad x\ ]^T \end{aligned}$$

Equation (A.10) is then equivalent to the nonlinear least squares problem as in Eq. (A.2). Using the nonlinear least squares method, the following equation is iterated until the solution converges:

$$z_{k+1} = z_k + \alpha\, Dg|_{z_k}{}^{\dagger} \left(\hat{Y} - g(z_k) \right) \tag{A.11}$$

where

$$Dg = \frac{\partial g}{\partial z} = \begin{bmatrix} \frac{\partial f}{\partial x} & \frac{\partial f}{\partial \theta} \\ I & 0 \end{bmatrix}$$

Similarly to Eq. (A.7), this equation converges in less than ten steps if this algorithm converges.

Bibliography

[1] E. Abbott and D. Powell. Land-vehicle navigation using GPS. *Proceedings of the IEEE*, 87(1):145–162, 1999.

[2] J. Ackermann and T. Buente. Yaw disturbance attenuation by robust decoupling of car steering. *Control Engineering Practice*, 5(8):1131–1136, 1997.

[3] H. S. Bae, J. Ryu, and J. C. Gerdes. Road grade and vehicle parameter estimation for longitudinal control using GPS. In *Proceedings of IEEE Conference on Intelligent Transportation Systems*, pages 166–171, Oakland, CA, 2001.

[4] I. Y. Bar-Itzhack and N. Berman. Control theoretic approach to inertial navigation systems. *Proceedings of the IEEE*, 11(3):237–245, 1988.

[5] Z. Berman and J. D. Powell. Role of dead reckoning and inertial sensors in future general aviation navigation. In *Proceedings of IEEE Position Location and Navigation Symposium*, Palm Springs, CA, 1998.

[6] D. M. Bevly et al. Use of GPS based velocity measurements for improved vehicle state estimation. In *Proceedings of the 2000 American Control Conference*, pages 2538–2542, Chicago, IL, 2000.

[7] D. M. Bevly, R. Sheridan, and J. C. Gerdes. Integrating ins sensors with GPS velocity measurements for continuous estimation of vehicle sideslip and tire cornering stiffness. In *Proceedings of the 2001 American Control Conference*, pages 25–30, Arlington, VA, 2001.

[8] BMW. *BMW Active Steering*, 2004. http://www.bmw.com/generic/com/en/fascination/technology/technologyguide/contentpages/active_steering.html?nl=1.

[9] M. E. Cannon et al. Low cost INS/GPS integration: Concepts and testing. *Journal of Navigation*, 54(1):119–134, 2001.

[10] C. R. Carlson and J. C. Gerdes. Optimal rollover prevention with steer by wire and differential braking. In *ASME Dynamic Systems and Control Division (Publication) DSC*, volume 72, pages 345–354, Washington, D.C., 2003.

[11] A. B. Chatfield. *Fundamentals of High Accuracy Inertial Navigation*. American Institute of Aeronautics and Astronautics, Inc., Reston, VA, 1997.

[12] B. Chen and H. Peng. Rollover warning of articulated vehicles based on a time-to-rollover metric. In *ASME Dynamic Systems and Control Division (Publication) DSC*, volume 67, pages 247–254, Nashville, TN, 1999.

[13] R. Da, G. Dedes, and K. Shubert. Design and analysis of a high-accuracy airborne GPS/INS system. In *Proceedings of ION GPS*, Kansas City, MO, 1996.

[14] J. C. Dixon. *Tires, Suspension and Handling*. Society of Automotive Engineers, Warrendale, PA, 1996.

[15] A. E. Duwel et al. Quality factors of mems gyros and the role. In *The Proceedings of the 15th IEEE International Conference on Microelectromechanical Systems (MEMS)*, pages 214–219, Las Vegas, NV, 2002.

[16] J. Farrelly and P. Wellstead. Estimation of vehicle lateral velocity. In *Proceedings of IEEE Conference on Control Applications*, pages 552–557, Dearborn, MI, 1996.

[17] Y. Fukada. Slip-angle estimation for vehicle stability control. *Vehicle System Dynamics*, 32(4):375–388, 1999.

[18] W. R. Garrott, M. W. Monk, and J. P. Chrstos. Vehicle inertial parameters measured values and approximations, 1988. SAE Paper No. 881767.

[19] J. D. Gautier. *GPS/INS Generalized Evaluation Tool (GIGET) for the Design and Testing of Integrated Navigation Systems*. PhD thesis, Stanford University, 2003.

[20] D. Gebre-Egziabher, R. C. Hayward, and J. D. Powell. Low-cost GPS/inertial attitude heading reference system (AHRS) for general aviation applications. In *Proceedings of IEEE Position Location and Navigation Symposium*, Palm Springs, CA, 1998.

[21] D. Gebre-Egziabher, R. C. Hayward, and J. D. Powell. Design and performance analysis of a low-cost aided dead reckoning navigation system. *Gyroscopy and Navigation*, 35(4):83–92, 2001.

[22] A. Gelb et al. *Applied Optimal Estimation*. The M.I.T. Press, Cambridge, Massachusetts, 1974.

[23] T. D. Gillespie. *Fundamentals of Vehicle Dynamics*. Society of Automotive Engineers, Warrendale, PA, 1996.

[24] R. W. Goldman, M. El Gindy, and B. T. Kulakowski. Rollover dynamics of road vehicles: Literature survey. *Heavy Vehicle Systems*, 8(2):103–141, 2001.

[25] M. S. Grewal, L. R. Weill, and A. P. Andrews. *Global Positioning Systems, Inertial Navigation, and Integration*. John Wiley and Sons, New York, NY, 2001.

[26] J. Hahn et al. Road bank angle estimation using disturbance observer. In *Proceedings of AVEC 2002 6th Int. Symposium on Advanced Vehicle Control*, pages 381–386, Hiroshima, Japan, 2002.

[27] M. Hiemer et al. Cornering stiffness adaptation for improved side slip angle observation. In *Proceedings Preprints of IFAC Symposium on Advances in Automotive Control*, pages 685–690, University of Salerno, Italy, 2004.

[28] S. Van Huffel and J. Vandewalle. *The Total Least Squares Problem: Computational Aspects and Analysis*. Society for Industrial and Applied Mathematics, Philadelphia, 1991.

[29] K. Huh and J. Kim. Active steering control based on the estimated tire forces. *Journal of Dynamic Systems, Measurement, and Control*, 123(3):505–511, 2001.

[30] ISO (International Organization for Standardization). *Road vehicles – Vehicle dynamics and road-holding ability – Vocabulary*, 1991. ISO 8855.

[31] S. Kimbrough. Coordinated braking and steering control for emergency stops and accelerations. In *ASME Design Engineering Division (Publication) DE-Vol. 40*, pages 229–244, Atlanta, GA, 1991.

[32] A. Lawrence. *Modern Inertial Technology: Navigation, Guidance, and Control*. Springer-Verlag, New York, NY, 1998.

[33] A. Masson, D. Burtin, and M. Sebe. Kinematic DGPS and INS hybridization for precise trajectory determination. In *Proceedings of ION GPS*, Kansas City, MO, 1996.

[34] C. McMillan et al. Dynamic GPS attitude performance using INS/GPS reference. In *Proceedings of ION GPS*, pages 675–682, Salt Lake City, UT, 1994.

[35] W. F. Milliken and D. L. Milliken. *Race Car Vehicle Dynamics*. Society of Automotive Engineers, Warrendale, PA, 1995.

[36] P. Misra and P. Enge. *Global Positioning System: Signals, Measurements, and Performance*. Ganga-Jamuna Press, Lincoln, MA, 2001.

[37] M. Nagai, S. Yamanaka, and Y. Hirano. Integrated control law of active rear wheel steering and direct yaw moment control. In *Proceedings of AVEC 1996 3rd Int. Symposium on Advanced Vehicle Control*, Aachen, Germany, 1996.

[38] A. Nishio et al. Development of vehicle stability control system based on vehicle sideslip angle estimation, 2001. SAE Paper No. 2001-01-0137.

[39] Novariant. *AutoFarm GPS Precision Farming*, 2004. http://www.novariant.com /agriculture/products/index.cfm.

[40] J. S. Randle and M. A. Horton. Low cost navigation using micro-machined technology. In *Proceedings of IEEE Conference on Intelligent Transportation Systems ITSC*, pages 1064–1067, Boston, MA, 1997.

[41] J. Ryu and J. C. Gerdes. Integrating inertial sensors with GPS for vehicle dynamics control. *ASME Journal of Dynamic Systems, Measurement, and Control*, 2004.

[42] J. Ryu, E. Rossetter, and J. C. Gerdes. Vehicle sideslip and roll parameter estimation using GPS. In *Proceedings of AVEC 2002 6th Int. Symposium on Advanced Vehicle Control*, Hiroshima, Japan, 2002.

[43] G. T. Schmidt. Strapdown inertial systems - theory and applications. In *AGARD (Advisory Group for Aerospace Research and Development) Lecture Series*, page 1, London, England, 1978.

[44] T. Schonberg et al. Positioning an autonomous off-road vehicle by using fused DGPS and inertial navigation. *International Journal of Systems Science*, 27(8):745–752, 1996.

[45] R. F. Stengel. *Optimal Control and Estimation*. Dover Publications, Mineola, NY, 1994.

[46] H. E. Tseng. Dynamic estimation of road bank angle. *Vehicle System Dynamics*, 36(4-5):307–328, 2001.

[47] H. E. Tseng et al. Development of vehicle stability control at Ford. *IEEE/ASME Transactions on Mechatronics*, 4(3):223–234, 1999.

[48] A. Y. Ungoren, H. Peng, and H. E. Tseng. Experimental verification of lateral speed estimation methods. In *Proceedings of AVEC 2002 6th Int. Symposium on Advanced Vehicle Control*, pages 361–366, Hiroshima, Japan, 2002.

[49] A. T. van Zanten. Evolution of electronic control systems for improving the vehicle dynamic behavior. In *Proceedings of AVEC 2002 6th Int. Symposium on Advanced Vehicle Control*, Hiroshima, Japan, 2002.

[50] A. T. van Zanten, R. Erhardt, and G. Pfaff. VDC, the vehicle dynamics control system of Bosch, 1995. SAE Paper No. 950759.

[51] S. Weisenburger and C. Wilson. An integrated vehicle positioning system for safety applications. In *Proceedings of the 1999 ION National Technical Meeting*, pages 361–368, San Diego, CA, 1999.

[52] M. Würtenberger, St. Germann, and R. Isermann. Modeling and parameter estimation of nonlinear vehicle dynamics. In *ASME Dynamic Systems and Control Division (Publication) DSC*, volume 44, pages 53–63, Anaheim, CA, 1992.

[53] D. Yanakiev and I. Kanellakopoulos. Speed tracking and vehicle follower control design for heavy-duty vehicles. *Vehicle System Dynamics*, 25(4):251–276, 1996.

[54] P. Yih, J. Ryu, and J. C. Gerdes. Modification of vehicle handling characteristics via steer-by-wire. In *Proceedings of the 2003 American Control Conference*, Denver, CO, 2003.

[55] P. Yih, J. Ryu, and J. C. Gerdes. Vehicle state estimation using steering torque. In *Proceedings of the 2004 American Control Conference*, Boston, CO, 2004.